Mathematical Modelling and Design for the Scale-up of an AACVD Process

A thesis submitted to the University College London for the degree of Doctor of Philosophy

2021

by

Pedro Ivo de Oliveira Filho

Supervisor:
Prof Eric S Fraga

The Sargent Centre for Process Systems Engineering
Department of Chemical Engineering
University College London
Torrington Place
London WC1E 7JE

I, Pedro Ivo de Oliveira Filho, confirm that the work presented in this thesis is my own. Where information has been derived from other sources, I confirm that this has been indicated in the thesis.

Pedro Ivo de Oliveira Filho

Abstract

The manufacturing process of photovoltaic devices, such as solar cells, relies on the production of Transparent and Conductive Oxide (TCO) films. One of the techniques for creating these films is based on Aerosol-Assisted Chemical Vapour Deposition (AACVD). The AACVD process comprises the atomisation of a precursor solution into aerosol droplets, which are transported to a heated chamber for the synthesis of films such as the TCOs, as well as coatings, powders, composites and nanotubes. At present, AACVD has not been used as an industrial deposition technique. However, it has the potential to be scaled-up due to its versatility and the ease through which effective functional coatings can be deposited at a laboratory-scale. Computational simulations are pivotal to study the feasibility of such a scale-up.

This thesis presents, therefore, an integrated model to support the AACVD process scale-up. The model is comprised of four stages: aerosol generation, transport, delivery and chemical deposition. The generation of aerosol is described by a distribution of droplet sizes, which is the input to a transport model that incorporates the impact of aerosol losses. The output distribution provides sufficient information to predict the amount and sizing of aerosol reaching the deposition site. Experimental validation has shown the model to be effective at predicting transport losses and droplet sizes. The delivery stage includes the solvent evaporation, accounting for uncertainties in the temperature profile of the deposition site. This is a key factor for the solvent evaporation, setting the precursors free to react and form the desired products. For the chemical deposition stage, reactions in the solid and gas phases were studied. The model presented is suitable for application on the scale of industrial processes and is also suitable for processes that rely on atomisation and transport of particles, for example, spray drying or cooling and fuel combustion.

Lessons learned in modelling uncertainties and their impact on process scale-up motivated the research into formulation, modelling and solution methods for such applications. Therefore, as an additional contribution, this thesis introduces Uncertainty.jl, a modelling framework focused on the treatment of uncertainty. The framework aims at a concise and natural syntax, allowing for a traditional mathematical notation without having to compromise between speed and code readability. Methods and operators were defined so that users can easily write down models with intrinsic parameter uncertainty and evaluate these models. Examples are presented to show the ease with which models can be developed using the framework. The contributions of this thesis are freely available on GitHub [1].

Impact Statement

Ever-growing energy demand coupled with increasing air pollution and depletion of fossil-fuel resources are key indicators of the need for sustainable energy alternatives. The demand for solar cells has been increasing steadily and the advancement of their manufacturing process is crucial. This thesis aims at contributing with such an advancement. Solar cells rely on the production of Transparent Conducting Oxide (TCO) films, which can be done via the Chemical Vapour Deposition (CVD) process. This technique involves the vaporisation of volatile precursors and their transport to the reaction site, where the deposition and film formation take place. A modification of the CVD technique results in the Aerosol-Assisted Chemical Vapour Deposition (AACVD), which generates aerosol droplets from the precursor solution instead of vaporising it. More options of precursors become available and the deposition rate at the substrate is higher.

Since AACVD is still being developed in the laboratory-scale, modelling the process is essential for scaling it up. This thesis provides models whose applications range from obtaining information about how sensitive variables are to the scale of the process through to assessing the viability and robustness of the industrial-scale process. Simulations also work as a proof-of-concept for the feasibility of keeping the current CVD equipment used in the industry to operate using the AACVD technique instead. Additionally, the collaboration in the Engineering and Chemistry interface is fostered: industrial requirements interact with *in silico* experiments, which interact with laboratory experiments.

The models and methodology of this thesis are also suitable for applications that rely on atomisation and transport of particles; for example, spray drying or cooling, ink-jet printing, agricultural sprays and fuel combustion. Additionally, in the context of the current COVID-19 pandemic, another possible application is the prediction of the extent of deposition of virus-contaminated aerosol in human airways.

Finally, as a free and open-source software, which fosters collaboration, free exchange of ideas and drives creative, scientific and technological advancements; this thesis introduces Uncertainty.jl, an intuitive modelling framework that allows the rapid development of complex models under uncertainty. The framework is user-friendly and straight forward to be employed, inviting users who are not experts in computer programming. The Uncertainty.jl framework and the AACVD models developed and presented in this thesis are freely available on GitHub [1].

Acknowledgements

I once came across the following quote: "*omnia autem probate: quod bonum est tenete*". It turned out to be a verse from the Bible, 1 Thessalonians 5:21, meaning "test everything; retain what is good". At that time, Process Systems Engineering was already one of my favourite fields. Jokingly, I thought: "testing everything is too expensive computationally... One can do better than that!". Having mentioned a Bible passage, I can naturally express my gratitude for the many gifts that I received from God throughout my life. *Servi Jesu et Mariae*!

I thank my colleagues, tutors, professors, and all those who contributed to my personal and professional development. I am grateful for the constant support and friendship provided by my principal supervisor, Prof Eric Fraga. I also thank Prof Angeli for her insights, Dr Dua, my subsidiary supervisor, and all the UCL Chemical Engineering staff for the support provided. I am very grateful for the discussions with NSG/Pilkington engineers and with Dr Potter, Dr Powell, Prof Parkin and Prof Carmalt, from UCL's Department of Chemistry, who also helped me with experimental validation for the mathematical models presented in this thesis.

I am extremely grateful to my family and friends, who have always been by my side. My parents, Pedro and Graciéli, and my siblings, Marina, Pedro Henrique and Mônica. My godchildren, Gustavo and Helena. My cousins, Fred, Ivanzinho, Mônica and Líllian, who are pretty much my siblings. My godparents, Dindinha, Márcia, Mércia (*in memoriam*) and Arturo. My lifelong friends, Dr Bruno, The Honourable Justice Guisinho, Dr Heyder and João Paulo. My favourite scientist, friend and mentor, Dr Annabel Cormack, whose insights and discussions have always been instigating. IMPA's pupil, Dr Pedro Borges. My Rio family, Stelinha, Ric, João, Zé and Juju, with whom I have countless memories, as well as my adoptive grandparents Francisco (*in memoriam*) and Eir, Péricles and Marlene. My friends from Coltec, UFMG and McMaster. At UCL, Imperial College, Newman House and Netherhall House, I will never forget all the adventures with Dr Kostas, Dr Harry, Dr Flavio, Dr Andres, Dr Alba, Dr Sergio, Dr Joanne, Dr Vincent, Dr Tomasz, Bea Espiritu, Syed, Julian, Jasmine, Antonia, Honora, Julia, Anne, Anthony, Bianca, Shaun, Barnaby, Benedykt, Clam, Irene, Jurgen, Jan, Jakov, Alex, John and Mariacarla. Most importantly, I thank my sweet Maysa for her unconditional love and support.

This work has been done with the support of the Brazilian National Council for Scientific and Technological Development (CNPq, Portuguese: Conselho Nacional de Desenvolvimento Científico e Tecnológico) and the British Engineering and Physical Sciences Research Council (EPSRC), towards which I am grateful.

Contents

List of Figures

List of Tables

1 Introduction and Background

This thesis finds itself under the scope of mathematical modelling and design for process scale-up under uncertainty. The main application is on the Aerosol-Assisted Chemical Vapour Deposition (AACVD) process scale-up.

1.1 Motivation

Competition in a global market and governmental regulations pose many challenges to the chemical industry and, therefore, to process systems engineers. The concerns for any successful process are mainly economic, environmental and social [2, 3]. A prosperous process must deliver products that satisfies the needs of the consumers while generating profit. The process should also be sustainable, given that society's perception is now greatly affected by environmental matters. As an example, products are now often designed with the "cradle to cradle" model [4]. The selection of raw materials and reactants already minimises possible by-products such as dangerous pollutants, while also considering product recycling and circularity.

One of the main challenges for sustainable development is in the energy field. In particular, low-cost and efficient solar cells have become more and more relevant for the generation of clean, affordable and reliable energy [5–7]. The manufacturing process of such photovoltaic devices relies on the production of Transparent and Conductive Oxide (TCO) films. One of the techniques showing growing potential for the production of these films relies on Aerosol-Assisted Chemical Vapour Deposition (AACVD), however it still needs further research before it can actually be used in the context of an industrial-scale production of thin films. In summary, AACVD comprises the atomisation of a precursor solution into aerosol droplets, which are transported to a heated chamber for the synthesis of films such as the TCOs, as well as coatings, powders, composites and nanotubes. At present, AACVD has not been used as an industrial deposition technique. However, it has the potential to be scaled-up due to its versatility and the ease through which effective functional coatings can be deposited at a laboratory-scale. Computational simulations are pivotal to study the feasibility of such a scale-up.

A key aspect of mathematical models is their capabilities to deal with uncertainty.

The design of an industrial process or the improvement of an existing one has different stages to be analysed. Uncertain parameters may be present throughout, from synthesis, design, planning, and scheduling through to the control of processes, where unexpected variations may occur in some parameters. Not taking into account uncertainties may lead to sub-optimal operation or even failure of the process. As an example, the production of functional thin films is subject to reaction rate constants and transfer coefficients that may not be known or cannot be specified with certainty, leading to uncertain deposition rates. Such a process is ideally built after comparing many proposed design options, which must account for the uncertainties. Therefore, simulating the process and considering uncertainties at the design stage is essential.

1.2 Research Contributions

The main focus of this work is to use mathematical models to simulate the AACVD process and to study the viability of bringing it from a laboratory-scale to an industrial-scale. The aim is at keeping the models simple and yet effective, using lumped parameters when possible to reduce the computational requirements and make them suitable for use in a future model-based design procedure. The models are also used to understand the sensitivity of the design variables to the scale of the process and, subsequently, to investigate the robustness of the design to the impact of uncertainties. In particular, the focus is on parameters, measurements and process uncertainties, which become the main sources of model uncertainties.

An integrated model to support the AACVD process scale-up is introduced. The model is comprised of four stages: aerosol generation, transport, delivery and chemical deposition. There is a range of droplet sizes obtained when generating aerosol, which are represented accordingly. The generation of aerosol by ultrasonic vibration is described by a distribution of droplet sizes. Such a distribution is the input to a transport model that incorporates the impact of aerosol losses, which depend on the properties of the droplets, the flow and the piping system. The output distribution provides sufficient information to predict the amount and sizing of aerosol reaching the deposition site. The transport model is tested through different scenarios, using horizontal, inclined and vertical pipes of different lengths connected by bends. Experimental validation will show that the model introduced is effective at predicting transport losses and droplet sizes. The delivery stage includes the droplet evaporation after leaving the transport system and accounts for uncertainties in the temperature profile of the deposition site. This is a key factor for the solvent evaporation, setting the precursors free to react and form the desired products. For the

chemical deposition stage, reactions in the solid and gas phases are studied, where obtaining a correct description of the mechanisms of reaction is a key challenge to predict the film growth rate. The model presented is suitable for application on the scale of industrial processes and is also suitable for processes that rely on atomisation and transport of particles, for example, spray drying or cooling and fuel combustion.

Lessons learned in modelling uncertainties and their impact on process scale-up motivated the research into formulation, modelling and solution methods for such applications. Therefore, as an additional contribution, this thesis introduces Uncertainty.jl, a modelling framework focusing on the treatment of uncertainty. Such a framework is based on Julia, given that it is an open-source modern computationally efficient language (scripted but with just-in-time compilation) providing support for the design of domain specific languages via abstract types, multi-dispatch, operator overloading and full Unicode support. The framework aims at a concise and natural syntax, allowing for a traditional mathematical notation. For instance, the user can write $t = 700 \pm (3\delta)$ (simple range of uncertainty), $X \sim \mathcal{N}(\mu, \sigma^2)$ (probability distribution function) or $F_0 = V^3 + [21.3, 21.7]$ (interval arithmetic) without having to compromise between speed and code readability. A number of methods and operators were defined, which allow users to easily write down models with intrinsic parameter uncertainty and evaluate these models. In addition to the AACVD scale-up model, several examples are presented to show the ease with which models can be developed using the framework, while the solutions obtained demonstrated its viability. The Uncertainty.jl framework and the AACVD models developed and presented in this thesis are open-source and freely available on GitHub [1].

1.3 Thesis Structure

Chapter 2 develops in detail the context and background of this thesis, including a review of the relevant literature on process design and scale-up. Chapter 3 introduces Uncertainty.jl, a modelling language designed to model uncertainties while writing computational models. Chapter 4 presents the mathematical models used to study the the AACVD process. Chapter 5 presents the results of the AACVD models and experimental validation, while Chapter 6 presents the results for an industrial-scale AACVD process. Finally, a summary and the conclusions of the work presented in this thesis is found in Chapter 7.

2 Process Design and Scale-up

In the context of the contributions previously introduced, the following sections will outline the relevant concepts, some of the work done so far by fellow scientists and engineers, as well as possible advancements yet to be achieved, towards which this thesis leaves a humble contribution. Firstly, Aerosol-Assisted Chemical Vapour Deposition process will be reviewed. Then, mathematical modelling under uncertainty is discussed with the process scale-up application, along with the related methods and tools.

2.1 Aerosol-Assisted Chemical Vapour Deposition (AACVD)

Aerosol-Assisted Chemical Vapour Deposition (AACVD) is a modification of the conventional atmospheric pressure Chemical Vapour Deposition (CVD) process for the production of functional thin films. In both processes, chemical precursors react and/or decompose on a substrate, forming the desired product. Both CVD and AACVD can be used in the synthesis of films, coatings, powders, composites and nanotubes [8–12]. Each one of these products has a particular application, for example, in electronics and optoelectronic applications [13–17], self-cleaning surfaces [18–21], and transparent conducting oxide (TCO) films; the latter are a special class of glass coating which can be used in solar cells and smart glasses [22–25].

Conventional CVD is based on the vaporisation of the precursors before delivering them to the reaction site, while AACVD generates an aerosol from a solution containing the precursors. For AACVD, although the precursors still need to be vaporised to undergo the chemical vapour deposition at the reaction site, they do not need to be transported in the vapour phase, which means that a wide range of safe and easy to handle precursors can be used. The aerosol-assisted method allows easy doping, since the stoichiometric ratio of dopant precursors to film precursors in the solution can be closely related to the stoichiometric ratio in the resultant film. On the other hand, conventional CVD would require precise control over gas flow rates, which can be unreliable. There are also cost benefits when using AACVD since it

is no longer necessary to heat and vaporise the precursors and to heat the piping system to prevent condensation during transport of the vaporised precursors as is done for the conventional CVD. The morphology of the films deposited via AACVD can also be controlled as a function of the solvent used for the precursor solution and different morphologies will lead to different properties, customised according to the final application. Lastly, AACVD does not need a sophisticated reactor, since it can operate in open atmosphere [8, 9, 26].

In the laboratory-scale, AACVD has been shown to produce low-cost, high-efficiency and high-quality products with optical and electrical properties comparable to industry standards [8, 27–39]. The challenge is to predict the behaviour of an AACVD process at industrial-scale. With that aim, this thesis will use mathematical models along with the experimental data from the successful laboratory-scale AACVD implementations. The success of the large-scale process can be specified in terms of the highest specific product formation rate obtained that meet the industry standard properties for the products. The scale-up procedure of the AACVD process involves assigning values for design variables that will impact the aerosol drop size distribution, the loss of aerosol during transport, the solvent evaporation, and the chemistry in the deposition site. Finally, as an alternative to designing a new plant, the AACVD process could potentially be suited to being incorporated into current CVD industrial plants for thin film deposition. The objective is, therefore, to look at the feasibility of generating aerosol and transporting it to the processing line using existing CVD facilities. Challenges are mainly due to the distributed nature of drop sizes in the aerosol, the prediction of losses over long distances, the need to model the evaporation of the solvent in the delivery, and the complex reactions potentially taking place in the deposition site. This thesis will introduce an integrated model of the AACVD process for use in industrial-scale design. The model is comprised of the following sub-processes: aerosol generation, aerosol transport, aerosol delivery, and the chemical deposition itself, as shown and described in Figure 2.1.

Finally, it is important to mention that the atomisation of particles is an important process, given that many industrial applications require the production of droplets with a particular size, for example, spray drying or cooling, film coating, incineration/combustion of liquid fuels/waste or fuel injection in internal combustion engines, production of fine emulsions, ink-jet printing, agricultural sprays, mass spectrometry, pulmonary drug delivery, DNA microarray printing and controlled release drug delivery, among others [40, 41]. Ideally, the atomisation process should control as tightly as possible the droplet median size, size distribution range, morphology, and possibly the droplet composition, according to the application. For

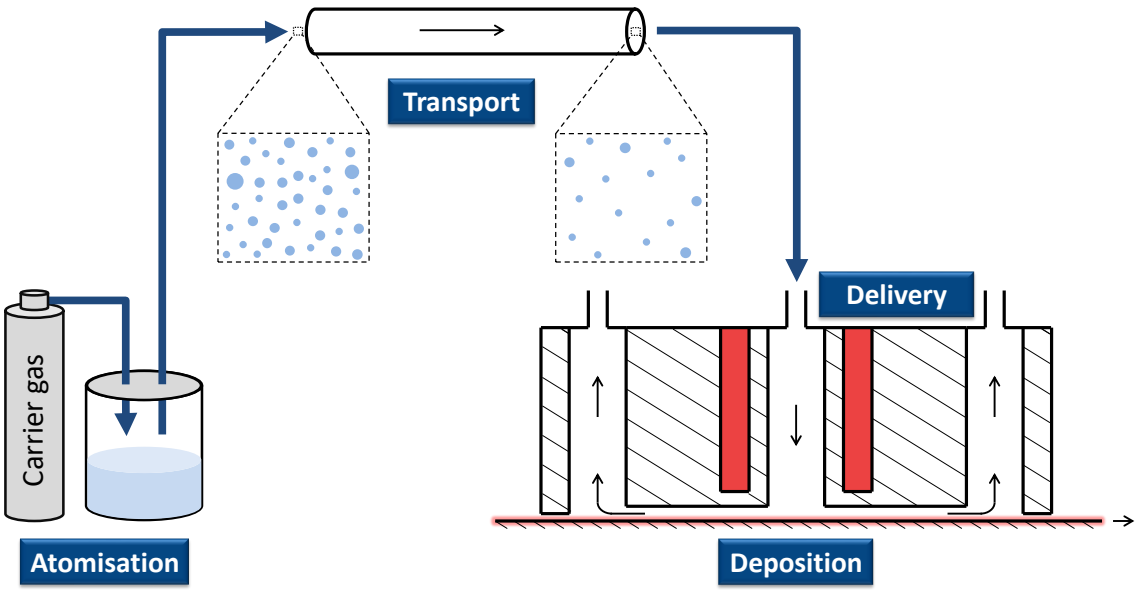

Figure 2.1: Schematic diagram of a large continuous industrial-scale Aerosol-Assisted Chemical Vapour Deposition (AACVD) process, divided into four units: firstly, a solution containing the precursors is atomised via ultrasonic vibration to generate aerosol. Carrier gas is then used to transport the aerosol over long distances (tens to hundreds of metres), which causes some aerosol loss and change of its size distribution. In the delivery unit, a cross-section of the equipment is shown, where the filled rectangles represent heat exchangers used to heat the carrier gas and evaporate the solvent, releasing the precursors. Finally, a functional thin film is continuously grown on top of a moving glass by the chemical deposition of the precursors.

AACVD, the solution containing the precursor (more often) or the precursor itself has to be atomised and become an aerosol before being sent to the reaction chamber. There are several methods for the atomisation, each one with a particular mechanism; the most popular ones were reviewed by Hou and Choy [9]. Depending on the method used, it is possible to achieve different generation rates and droplet size distributions. It is important to be able to control the size of the droplet and how narrow the distribution of sizes is, which will be a subject of study presented in this thesis.

2.2 Process Modelling for the Chemical Deposition

After the precursors are dissolved, the solution is atomised into aerosol, which is transported to the reaction site. There, the chemical vapour deposition itself will take place. The deposition is well-known to have complex gas-phase and surface processes. This includes transport phenomena (mass, momentum and energy), thermodynamics, kinetic competition between phases, species diffusion, classical nucleation theory, adsorption and desorption kinetics and equilibrium. The reaction mechanisms can also be very complex, including up to hundreds of reactions and chemical intermediates [42].

There have been a number of chemical vapour deposition models proposed for specific deposition processes, with different degrees of complexity. They aimed at the manufacture of specific products, for example, the deposition of diamond [42], boron [43], tungsten [44], silicon carbide [45], carbon nanotubes [46], fused silica glass [47, 48], graphene [49], silicon [50] and carbon fibre [51].

The governing equations for each of the above models are based on the mass, momentum and energy conservation equations. What changes is the particular mechanism suggested for the specific deposition modelled and the depth of the models in terms of how lumped the parameters are. There are also differences regarding how the parameters are calculated. For example, some models used the Arrhenius law to estimate the kinetic constants, other models fitted the parameters using experimental data. The more lumped the parameter are, the easier it may be to interpret the equations and fit the parameters. However, there may be loss of precision in the results. Instead of actually writing down the conservation equations, it is possible to use their already implemented version within the computational fluid dynamics framework, for example, using the Ansys Fluent Software [1]. The drawback is the expensive computational costs to evaluate the models.

There will always be a trade-off between model complexity and precision of results.

[1] https://www.ansys.com/products/fluids/ansys-fluent

Ideally, the models should be as complex as necessary to provide useful results, but not more complex. With that in mind, this thesis will write conservation equations for the production of a non-specified film. The equations can then be adapted for a particular film and the extent of simplifications can also be adapted. For example, if the mechanism for a particular deposition is limited by the diffusion of the precursor from the gas phase to the interface with the solid, the kinetics of the reaction could be neglected. The mechanisms are studied in laboratory-scale experiments, but scaling-up the deposition is necessary for large-scale applications. Therefore, the use of mathematical models for scale-up is discussed next.

2.3 Mathematical Modelling for Process Scale-up

Taking a process from laboratory to industrial-scale poses significant challenges when predicting the behaviour at the larger scale. Laboratory experiments can test different parameters, such as temperature, pressure, flow rates, solution concentration, etc. However, given successful operating conditions for the laboratory setting, adjustments will be necessary to achieve a large-scale operation [52–56]. Many variables are scale-dependent, for example, the transfer of heat is strongly dependent on the ratio of surface area to volume. Laboratory experiments are key for understanding the underlying process behaviour, including reaction mechanisms and transport phenomena. It is then necessary to determine the variables that will need to be adjusted and also how they will have to change in order to keep the feasibility of the process. The design of equipment at a larger scale and the criteria that may be used in taking decisions about such equipment are based on the modelling of the process features [57, 58]. Extrapolating from the experimental parameters to obtain the industrial-scale parameters will also introduce uncertainties in the prediction of the process behaviour, which will be discussed in the next section.

Some variables will need to have their values adjusted when moving from the laboratory to the industrial-scale. Therefore, models will be proposed aiming at simulating the AACVD process to study how those variables will have to change in order to keep the expected outcome and the feasibility of the industrial-scale process. Models will be used to guide the design of the industrial-scale process, also using data gathered from small-scale experiments. The models developed may also prove useful for the analysis of existing processes based on aerosol generation, transport, delivery and chemical deposition.

2.4 Uncertainty

There are different definitions for uncertainty. In general, it refers to the impossibility of having a parameter associated to a correct fixed value. One may assume a fixed value; however, there is a range of values that the quantity could assume. Therefore, such fixed value would actually be a nominal value. Uncertainty also refers to the existence of variations in a measured parameter. This means that one can expect the true value to lie within an interval, which can be called the uncertainty interval. It is important to study the effect on the final results of the uncertainties linked to each measurement made.

The overall uncertainty of a process has the contributions of many sources. For example, conceptual modelling errors (wrong or incomplete assumptions, simplifications, wrong equations, etc.), unknown consequences that depend on future events, imprecise decision-maker preferences, vague information, uncertainties related to the measuring devices, system disturbances, sensor-system interactions, etc. Therefore, treating uncertainty is a key element in process modelling.

2.4.1 Uncertainty in Computational Models

Uncertainty is ubiquitous in process design and scale-up, given that there is always imperfect or unknown information where it is impossible to exactly describe all the parameters [59]. Uncertainties in the model predictions are also introduced when some of the model parameters are fitted from experimental data, which is usually necessary when building models for process scale-up. Assumptions also generate a number of uncertainties in the process models. Consequently, it is important to consider the possible ranges of uncertain parameters and to understand how they impact the process, while ensuring that the process continues working regardless of the actual value that the parameters assume, anywhere in their uncertain ranges. This grants the robustness of the process to uncertainties. Sensitivity and uncertainty analysis [60] can be used to evaluate the robustness of the process models and to quantify the expected extent of variation in the process outcome, in addition to identifying the sources for variations in process performance.

Some parameters may have a single exact value, which cannot always be known with precision. Other parameters are themselves inherently distributed due to variability or heterogeneity, for example, the sizes of droplets generated by ultrasonic vibration. Both cases can be mathematically represented using the same approach, namely, probability theory [61]. The strengths of this approach are exemplified by how straight forward it becomes to quantify and understand how likely different

outcomes are and to visualise potential scenarios. Simulations of the AACVD models allow the study, for example, of the impacts of ranges of transfer coefficients and kinetic constants. Probability distributions can be used to describe such ranges. Quantities such as the mean, variance, skewness, upper and lower quantile values, and confidence intervals are used to understand the impacts on the results of the uncertain and distributed parameters. Such information may also be represented graphically, using probability density functions and likelihood plots, which can help understand the predicted behaviour of the scaled-up process.

The modelling of uncertainty is essential in process design and optimisation, evidenced by [59], who also shared some challenges in the field. In particular, they showed how important it is to develop tailored solution strategies, which can be facilitated when there is a framework that allows easy prototyping, especially with specific tools dedicated to representing uncertainty. Additionally, when dealing with uncertainty, running simulations helps to rationalise and explain the results from models. That can be done, for example, by incorporating Monte Carlo experiments and the associated statistical methods into the stochastic models [62]. A modelling language focused on the treatment of uncertainty would, therefore, be helpful to facilitate writing, running, maintaining and sharing computational models. This thesis will also leave a contribution regarding this necessity.

Another source of uncertainty stems from the change in scale of the process, given that some model parameters are not scale-invariant. When laboratory-scale experiments are used to find model parameters that adequately capture the physics of the system, uncertainties are introduced while scaling such parameters. Approximations must also be taken into account, since a simpler and yet effective model makes it easier to estimate its parameters, for example, kinetic and mass transfer coefficients.

2.4.2 Uncertainty Classification

Different classifications for uncertainties have been proposed [59, 63, 64]. The importance of classifying different types of uncertainties is mainly exemplified by facilitating the selection of different methods to treat particular groups of uncertainties. It is important to note that these classifications are not mutually exclusive and it is possible to have cases in which a combination of them is appropriate. The main classifications are now outlined.

Internal uncertainties are associated to the values and judgements of the decision-makers. Usually, two groups are used to distinguish the internal uncertainties. The first one is related to the lack of information about the process, such as the model parameters. The second group is related to the structure of the model, which de-

pends on the correctness or validity of the assumptions made. External uncertainties are the ones that affect the process, although they are not part of it, for example, product demand. Some authors also refer to external uncertainties when dealing with the lack of information about the consequences of the decision-maker's actions [64].

There are two possibilities for the realisation of the uncertainties. If the realisation is independent of the process decisions, the uncertainty is exogenous. Alternatively, if the decisions influence the realisation, the uncertainty is endogenous. This could happen, for example, if the probability distribution of an uncertain parameter changes or if the time when the realisation should occur changes. Exogenous uncertainties can be exemplified by fluctuations in the market, for example, the prices of raw materials. They can be represented using a scenario tree with defined shape. Whereas endogenous uncertainties can be represented using a scenario tree with conditional shape, given that the process decisions may change the time of realisation of uncertain parameters [59]. The endogenous uncertainties are usually related to technical choices, for example, the size of a solar module manufacturing plant can only be defined after the available locations are disclosed. Research on endogenous uncertainties is more recent and there are many opportunities of development; there is also a need for advancements on methods of optimisation to solve problems with the two types of uncertainties at the same time, which usually happens in real applications.

Finally, uncertainty can also be classified as epistemic or aleatory [65, 66]. The former refers to the incomplete knowledge, which creates difficulties to fix a meaningful value for a quantity; however, epistemic uncertainty can be reduced by increasing the effort to achieve more knowledge. On the other hand, the aleatory (also called random) uncertainty refers to the innate random behaviour of a process studied; therefore, it may be impossible to eliminate or even reduce aleatory uncertainty.

Most of the epistemic uncertainties are related to two sources [67, 68]. The first one regards errors in the process modelling, for example, the incapacity to know exactly how well the model represents reality and its range of validity. The second one is related to errors obtained by numerical methods to solve the modelling equation, for example, errors coming from approximations, convergence tolerances and discretisation of equations. On the other hand, random uncertainty is mostly associated to the physical nature of processes; examples ranging from quantum mechanic effects to the behaviour of the wind.

2.4.3 Uncertainty Sources

For experimental measurements of droplet size distributions using a laser diffraction system, as it will be done in this work, uncertainty has different possible sources. For instance, depending on the aerosol concentration, scattered light might be re-scattered by other droplets before reaching the detector. Also, the uncertainty in the density and optical properties of the atomised methanol, such as refractive index, might broaden the experimental results. Many other factors also generate uncertainty in the measurements, such as electronic noise, contamination on the optics, sunlight or artificial illumination, error in the alignment routine, ingress of moisture, dirt or contamination in the sensors. The distance of the spray from the measurement zone also impacts the results [69].

Beam steering and vignetting may lead to wider size distribution data: if measurements are made outside the working range of the lens, the system would measure incorrectly the light scattered at wide angles. This would cause the light scattered measured by the outer detectors to be partially lost, in which case the measured intensity would be less than expected. This effect is called vignetting. Beam steering, on the other hand, could occur if a significant volume of propellant gas or another gaseous phase apart from air is present in the measurement zone [70, 71].

All these factors explain the existence of uncertainties and suggest critical points to be careful about during the measurements. The minimisation of such factors can reduce uncertainties, increase the accuracy of the results and ensure experimental reproducibility. However, these factors also exemplify the importance of effective methods to compare uncertain experimental data with mathematical model results.

Modelling equations describing a physical process are usually obtained by the laws of conservation (mass, energy and momentum), as well as constitutive relations. Simplifications are usually used to obtain tractable models and can be separated into two groups, depending on what was assumed. The first one is related to assuming that some chemical or physical phenomena are negligible, whereas the second group is related to assuming steady or quasi-steady state in the processes to avoid dynamic equations.

Simplifications have the potential to create mismatches between the model and the real process. If these mismatches are acceptable, the model can be used, which solves the issue of infeasibility or high cost related to creating a model that better describes reality [57]. The mismatches can lead to model uncertainties, which also accounts for :

- Process disturbances: a process has several disturbances, acting in different time-spans.

  - Short-term (second, minute) disturbances: have impact on the process control level. For example, changes in temperature, pressure, composition, flow rate, etc.
  - Medium-term (day) disturbances: have impact on the optimisation level. For example, change in the raw material parameters.
  - Long-term (week, month) disturbances: have impact on the planning/scheduling level. For example, market fluctuations.

- Parametric errors: there may be inaccuracies in the model parameters (including the physical ones, whose values may not be accurately known).
- Mismatch between mathematical models and actual system behaviour: usually, models have simplifications regarding, for example, non-linearities and dynamics. This makes the model predictions differ from the actual measured values.

If the uncertainties are not negligible, the model might not be able to predict the behaviour of the process. Therefore, optimising such a model would not guarantee the real optimal process settings. If the model does describe the process accurately, it may still not be able to find its optimum settings, for example, if the model was only tested to predict the outputs, but not the gradients for the optimisation problem. Additionally, process performance may be sacrificed when the system is set very conservatively, ensuring that the constraints would never be violated, since it is particularly relevant for robust optimisation. On the other hand, sometimes it is acceptable to relax some constraints to improve the performance [72, 73].

Since model mismatches could lead to suboptimal or even to infeasible process operation, it is important to study if the model is well suited to the process. This is called model adequacy and it studies if a model is able to evaluate the actual process active constraints and gradients. Therefore, predicting the process outputs is not enough to find the optimal process settings. Additionally, a good model must minimise its conceptual and numerical mistakes which, if present, might result in worthless predictions. Finally, the preciseness of the output is a function of how accurate the input is [57].

Some model parameters may be obtained experimentally, which may be a source of uncertainty. Ideally, every experimental result should be followed by information regarding its associated uncertainty. Description of the basis data and methodology for the uncertainty analysis is essential for experimental results to be well presented. This allows an analysis of how scattered the dataset is, its significance and possible consequences. In addition, it allows a proper study of the system and suggests if it is necessary to search for tools to make the system more stable, decreasing the uncertainty. Some of these tools are exemplified by the use of better mathematical models, equipment and techniques to improve and make the system more reliable and predictable. Doing so successfully, means that new data will be less scattered than past results. Moffat [74] presented, in the context of engineering processes, a review on experimental uncertainties.

2.5 Mathematical Models Handling Uncertainty

Deterministic models may work well enough, if the uncertainties have only a small impact that can be ignored for the practical application in question. However, when the uncertainties are important, they should be taken into account to create a more robust model. There are several modelling approaches that can be used for uncertainty representation. The choice of which format will be used may have impacts on the decision making process. Durbach and Stewart [75] performed some experiments to exemplify how different formats can bias the final decision. Based on that, it is interesting to understand the methods available and how to select the best one for a particular application. The main representation formats, used individually or combined, are now addressed.

2.5.1 Probabilistic Models

The use of probability theory for building mathematical models is arguably the most common method to treat uncertainty, regardless of the field of study [67]. Basically, probability theory is applied to represent uncertain parameters as random variables characterised by probability distributions. Even when some of the variables have unknown distributions, alternative ones can be hypothesised and tested. Possible hypotheses may be discrete, having a finite or countable set; parametric, when the hypotheses are represented by a set of parameters; or non-parametric, when the set of hypotheses would need an infinite number of parameters [61].

Sometimes it is possible to split a problem into before and after the realisation of

uncertain parameters. Then, stochastic modelling with recourse becomes possible. For this, two sets are defined: in the first one, there are variables that must be decided before the uncertain parameters. Then, the random variables are realised and it is possible to choose a second set of variables (recourse), which improve the system or correct any infeasibilities that came from the realisation of the random variables. The second set is random, since it depends on the realisation of uncertain variables. Therefore, the aim is to choose the first set to optimise a given measure and the expected value of the same measure for the second set [63].

Probabilistic models are also used in multistage decision problems under uncertainty, also known as stochastic dynamic programming [76]. These problems usually have a discrete time system, which is assumed to evolve over N periods. Stochastic variables are used to describe the state of the system, the control action and random parameters (disturbance or noise, for instance). The objective is to minimise the additive cost function over all N periods.

2.5.2 Bounds and Intervals

Sometimes it is too expensive or not possible, for lack of information, to model probabilistic variables for the uncertain parameters. However, it is possible to bound the variables, for example, through the analysis of past data. Then, interval mathematics describes and treats the ranges that each uncertain variable could be realised. However, there is no information about probabilities of variables assuming particular values inside the interval, which has to be taken into consideration, since it could oversimplify the problem and lose important information. Finally, the ranges of the variables can be used to obtain worst-case scenarios [63].

2.5.3 Fuzzy Logic and Clouds

Strictly speaking, a fuzzy number represents a certain quantity, as it has a uniquely defined membership. However, it is possible to use and expand the concepts from fuzzy mathematics to be used as an alternative when there is not enough information to build probabilistic models [63, 77]. Instead of using probability functions to treat uncertainty, the uncertain parameters can be defined as fuzzy numbers and, when relevant, constraints as fuzzy sets. There is a 'membership function' that measures the degree of satisfaction when the model has constraints, which means that violation is allowed [78, 79]. While set theory and the use of bounds are able to limit the parameters to belong or not to a set, fuzzy theory allows parameters to be members of a set to some extent, based on possibility theory instead of using probability distributions.

Some authors use the term 'chance-constrained' programming [80] when referring to a methodology similar to fuzzy programming. For example, Nemirovski and Shapiro [81] used this terminology when they introduced an approximation method to solve computationally intractable optimisation problems with given probability of respecting the constraints. Additionally, Wendt et al. [82] explained the relationship between chance-constrained optimisation and probability distributions, as well as other applications. They also proposed an efficient method to solve non-linear chance-constrained problems accounting for uncertainty.

Another related methodology was introduced by Neumaier [83], who worked on the modelling of uncertainties using a mixture of fuzzy sets and probability distributions, which he defined as a 'cloud'. It has more information than a fuzzy set, but not as much as a probability distribution. The advantage is the flexibility obtained by the combination of the two well studied methods. He described the mathematical properties of the clouds, which can be used, for example, to simplify optimisation problems based on clouds.

2.5.4 Scenarios and Explicit Risk Measures

Uncertainty can also be represented in terms of its impacts, which can be captured in one or a small number of measures. For example, uncertainty can be decomposed into two components, value and risk. The first one is usually based on a measure of central tendency, such as the expected value. On the other hand, risk is commonly based on a measure of statistical dispersion, such as quantiles [64]. This method is widely used in the field of finance, where future returns are uncertain and risk measures are constructed and optimised to obtain the best portfolio [84].

Another option is the generation of possible alternatives, called scenarios, that the future might unfold. The analysis of such alternatives may provide insights related to the possible courses of action, given that a chain of causal effects has been built. The future can potentially unfold in several ways; therefore, it is possible to generate and analyse scenarios for all of them or the most important ones [59].

2.5.5 Propagating Uncertainty

A complex system has many variables linked to each other; therefore, the uncertainty of each variable also propagates to other variables. The final system output will have its uncertainty determined by the combinations of all uncertainties linked to all initial and intermediary variables. Consequently, the propagation of uncertainties and their effects are important steps before reaching reliable decisions. It also gives insights on how to make a system more robust, reducing its performance vari-

ations, by making it less sensitive to the main sources of variations. The propagation of uncertainty can be either based on complex models or on their approximations, as described next.

2.5.5.1 Complex Model Simulations

A simple and robust method to study uncertainty is based on simulations. Essentially, different input combinations are used to evaluate the model. The main deficiency of this approach is that the more complex a model is, the more computationally expensive it will be to perform model evaluations for each input combination.

The model evaluations can be done via a Monte Carlo method [85–87]. Given a function of many independent and uncertain variables, the Monte Carlo method randomly generates values for the variables and evaluates the model. This is repeated as many times as necessary to estimate the distribution of the output. First, it is necessary to define the distributions of the uncertainty in the input variables. Then, after the model evaluations, the uncertainty in the results and the sensitivity analysis are obtained [66]. The terminology Monte Carlo can be used to refer in general to any statistical technique of sampling; however, this thesis will refer to Monte Carlo as a specific method, the one that uses the greatest number of simulations.

Latin Hypercube [88] is a class of the sampling methods, usually used when an excessive computational time would be required if Monte Carlo simulations were to be used. To save model evaluations, Latin Hypercube divides the entire input domain into separate groups, called stratified samples; therefore, some information may be lost. However, the full range of each variable's domain is explored to increase accuracy of the results and to be closer to the results obtained by Monte Carlo simulations.

2.5.5.2 Surrogate Model Simulations

Large problems, such as the ones arising from chemical processes and industrial control [89], require expensive computer codes, generating time consuming simulations. Therefore, it may be infeasible to compare and contrast all possible options before decisions are made given a lack of resources such as time or computers powerful enough. Optimisation methods may rely on model evaluations, for example, sampling the design space and evaluating gradients through finite difference methods. To mitigate time consuming simulations, a complex model can be used to create an approximated and easier to evaluate model, here referred to as a surrogate model, although also known as meta-model or response surface [90, 91]. Additionally, there is the possibility of using data from possibly proprietary and computationally expensive simulation software to generate a surrogate model. The main objective of

a surrogate model is for it to replace the complex model. It must ensure two main features in the domain of interest: the first one is to be more efficient, which means that less computer power should be required. The second one is to be effective, that is, the approximation is good enough for practical purposes. The effectiveness of the surrogate model can be evaluated by a metric testing its ability to make predictions, which can be tested by physical experiments or simulations using the original model.

To simplify a model, the selection of a sampling space is the first step, followed by the construction of the surrogate, its validation and refinements. Then, the surrogate model can be used, for example, to perform sensitivity and uncertainty analysis, as well as process optimisation, with less computational cost. Kriging and polynomial chaos expansion methods are examples of how to generate surrogate models. Forrester and Keane [90] reviewed in depth the most applied methods, including those two, to build surrogate models and they also treated about optimisation based on surrogate models. The advantages and disadvantages of the methods were also studied. Finally, the authors presented some ideas related to the selection of a particular method for each particular application. Viana et al. [92] have recently written about the evolution of the techniques used to build surrogate models. Their review was based on what motivated the advancements in the field.

2.6 Modelling Tools

A computer language designed for a particular application is known as a domain-specific language (DSL). The main advantage of such approach is its focus: instead of including many applications, as the general languages do, the DSLs provide specifically what the user needs to solve a particular problem. Even though generality is lost, there is the possibility of defining specific tools and notations to address more effectively a particular type of problem. There is also an increase in productivity, since a DSL will be easier to use for its specific domain, as opposed to a general language.

General-purpose languages are very flexible, given the larger number of applications that can be treated. However, there is a higher implementation cost, since more time and effort must be dedicated for each particular application. When similar applications or similar problems are grouped, it may become interesting to use or develop a DSL, which could enable users to solve a problem without being limited by their programming skills. Ideally, the knowledge of the problem itself and its specificities should be the majority of the necessary effort to achieve the solution.

Rather than creating an entirely new language, a simpler approach is to create an embedded DSL. In other words, it is possible to create new components or to

automate existing tools. For example, Microsoft Excel has an embedded macro language, which grants programmability options to the user and has well-defined execution semantics. Another example is related to the presentation of high-level mathematics: OpenMath and Content MathML have well defined semantics to work with the representation of mathematical equations for the web. The importance of DSLs has been supported by different studies [93–97].

A subgroup of the DSLs focuses on allowing users to describe problems for large-scale mathematical computation. This subgroup, domain-specific modelling languages (DSML), usually uses a syntax similar to the actual mathematical notation of modelling and optimisation problems. This feature allows concise and readable definition of problems. Concepts, abstractions and their relationships regarding a modelling language can be tailored to the domain of interest. Therefore, the end-users are able to convey the core essence of their problem, from the domain they are experts, if the language they are using is tailored for them. The syntax of the language is related to its notation, which describes how users will learn from it (reading) and use it (writing and designing models). The language should be simple, but still expressive. This is granted through the writability, readability, learnability and effectiveness of the language. Then, the semantics of the language defines the meanings of each of the constructs forming an expression. According to that, the input will be changed while the program is executed and the output will be generated.

Well-known examples of DSMLs are AMPL, GAMS, Pyomo and YALMIP. Silva [98] reviewed and discussed modelling languages in the context of model-driven engineering. He gave a broad and integrated perspective on important concepts, such as system, model and modelling language. Even though his focus was mainly in languages to visualise and design systems in software engineering, most of the concepts studied are common to any type of programming language.

The programming language Julia is of particular interest for this thesis, since it is an open-source, high-level, high-performance, dynamic language. Additionally, Julia simultaneously has the advantages of the interactivity and syntax of scripting languages, such as MATLAB, Python, and R, with the speed of compiled languages such as Java, C and C++. In fact, Julia has been shown to at least approach the performance of C, which is known to provide some of the fastest numerical computations [99]. This thesis will, therefore, introduce a DSML focused on mathematical modelling under uncertainty within Julia. The main objective will be to create a user-friendly environment for the modelling of uncertainty.

2.7 The Research Gap

An integrated model to simulate the AACVD process cannot be found in the literature. The process itself is still being studied at a laboratory-scale and is yet to be adopted by the industry. There have been models proposed for aerosol generation and transport, but aimed at other applications. The chemical deposition itself has been modelled, but only for the production of specific films. With that in mind, this thesis aims at providing an integrated AACVD model, which can be parametrised to simulate both small and large-scale processes, batch or continuous, and with a general deposition methodology to allow the representation of different mechanisms for any specific film. There is also a lack of available free and open-source tools for handling uncertainties, which will be provided by this thesis, including tools and methodologies for a model-based scale-up under uncertainty. The gaps identified in the literature motivated the contributions of this thesis, as described in Section 1.2 and developed throughout the next chapters.

3 The Uncertainty.jl Framework

This chapter introduces Uncertainty.jl, an intuitive framework that allows the rapid development of complex models under uncertainty. Chapters 5 and 6 will then apply this framework for the modelling and scale-up under uncertainty of the AACVD process.

3.1 Purpose and Intended Functionalities

A number of tools to treat uncertainty are available in the fields of Probabilistic Programming [100–102] and Machine Learning [103–105]. Yet, in the field of process systems engineering, uncertainties are sometimes treated using deterministic approximations or modelled without the use of any dedicated computational tool. Even though process simulation systems (e.g. Aspen, Hysys, gPROMS) and/or modelling systems (e.g. GAMS, AIMMS, AMPL) have made it easier for practitioners to apply process systems engineering methodologies to industrial applications, the treatment of uncertainty is not always straightforward. There is, therefore, a necessity of further research on the development of tools aimed at the modelling of uncertainty. With that in mind, Uncertainty.jl aims to be an intuitive framework that allows the rapid development of complex engineering models under uncertainty. The framework is characterised by methods and operators which allow users to easily write down models with intrinsic parameter uncertainty or distributed quantities and evaluate these models.

Correctly formulating and solving a large model is already difficult. Therefore, having an easy and straightforward tool to represent uncertainty would be helpful. Such a tool should be connected to a fast language, allowing the user to write and solve very large computational problems when necessary. The framework proposed here will provide a concise and natural syntax, allowing for a traditional mathematical notation. For instance, users can write $t = 700 \pm (3\delta)$ (uncertainty range), $X \sim \mathcal{N}(\mu, \sigma^2)$ (probability distribution) or $F_0 = V^3 + [21.3, 21.7]$ (interval arithmetic) without having to compromise between speed and code readability.

Uncertainty.jl has the final goal of becoming a computational modelling language for incorporating uncertainty in mathematical modelling and also supporting communication with currently available modelling and simulation systems. The objective is to have a user-friendly syntax and to avoid the 'two-language problem', where modellers prototype algorithms in a user-friendly language such as Python but eventually have to rewrite them in a faster language like C++. This is both a time consuming and error-prone procedure.

3.2 Design and Implementation

Uncertainty.jl is a framework that provides a high-level interface to represent uncertainty in process modelling, built to address some of the challenges previously mentioned. The framework is user-friendly and straight forward to be employed, aiming therefore at users who are not experts in computer programming. It was written in Julia[1] for a number of reasons. Firstly, Julia is a high-level, high-performance, dynamic language, which allows both large-scale computation and flexible prototyping without having to simultaneously use two or more languages; for example, many engineers use MATLAB (high-level, but slow) and C (fast, but low-level) at the same time. On the other hand, Julia is a high-level language and yet has been shown to at least approach the performance of C [99, 106]. Finally, the users of Uncertainty.jl can also join the large and active community of Julia and have access to a vast and growing number of packages focused on scientific computing, which they can employ and, when necessary, extend.

Chen and Grossmann [107] outlined the current trend of allowing modellers direct access to model objects, which are easily created using Uncertainty.jl within Julia. This facilitates code sharing and the generation of models that are more readable and easier to validate. However, the main advantage is the use of Julia's multiple dispatch feature, allowing the overloading of generic functions using different type signatures [108]. This gives a greater expressive power, since additional code can be written in a concise and clear style.

[1] https://julialang.org/

3.3 Type Hierarchy

Another advantage of using multiple dispatch is how straight forward it becomes to extend any of the Julia packages already available. For example, Algorithm 3.1 shows how Uncertainty.jl extended the ODEProblem function, from the package DifferentialEquations.jl [109–111]. It now became possible to input uncertain parameters, which can be intervals or probability distributions, before solving the differential equations. Uncertainty.jl currently has the object hierarchy shown in Figure 3.1, which takes advantage of Julia's multiple dispatch. This allows, for example, that the appropriate ODEProblem method will be called according to the types of the input variables as follows: if the uncertain variables are all of the Interval type, Latin Hypercube Sampling will be used to generate samples. If there is a mix of intervals and probability distributions, a random sampling will be performed. The differential equations are then solved using the generated samples from the uncertain variables, according to their distributions. The output will itself be a distribution built from the solutions of the ODEs. The relevant statistics are also automatically provided. The framework also includes methods to perform sensitivity and uncertainty analysis for the whole model or its parts.

3.4 Operators

Uncertainty.jl allows users to take advantage of the full expressiveness of the Julia programming language while writing their models, supporting all of the basic Julia arithmetic operators, Boolean operators, and comparison operators, which are similar to C. However, Uncertainty.jl also defined and/or extended some operators to perform specific tasks. For example, the intuitive tilde-based operator ($\sim$) was defined for declaring a random variable following a specific probability distribution, as exemplified in Figure 3.2. Uncertainty.jl also supports interval arithmetic, allowing the user to perform operations such as the ones shown in Figure 3.3. Addi-

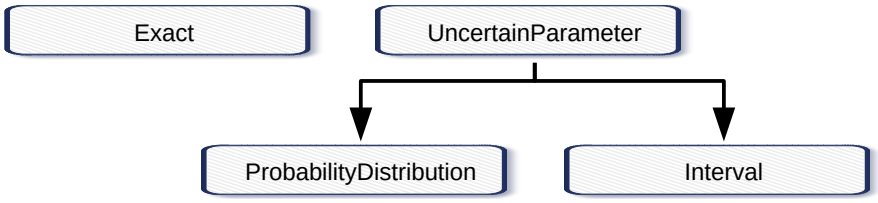

Figure 3.1: Current type hierarchy of the Uncertainty.jl framework.

```
1  Size = 500
2  Range = [0, 20]
3  X = ProbabilityDistribution(Size, Range)
4  k = 7
5  X ~ 𝒳²(k)
```

```
X ProbabilityDistribution
  x → Float64[500]
    minimum → 0.00
    maximum → 20.0
  P → Float64[500]
    mean → 7
    percentile25 → 4.25…
    median → 6.35…
    percentile75 → 9.04…
```

Figure 3.2: Definition of a random variable with 500 entries ranging from 0 to 20 and following a chi-squared distribution with 7 degrees of freedom. The output of line 5 is shown on the grey section, at the right-hand side. Screenshot from Atom editor.

```
1  δ = 20
2  x = 700 ± 3δ
3  y = x + [20, 50]
```

```
y Interval
    min → 660
    max → 810
```

Figure 3.3: Example of consecutive operations using interval arithmetic. The final output is in grey, at the bottom. Screenshot from Atom editor.

tionally, the plus or minus operator ($\pm$) was also defined, acting on real numbers to produce an interval, which can then be used in any further interval arithmetic operations. Finally, independent model evaluations, including the solution of differential equations, are intrinsically compatible with parallel computing, easily done in Julia. Methods are defined and readily available to be used with such operators to help decision makers to understand the impacts of uncertain variables. Examples are the mean, variance, skewness, upper and lower quantile values. Such information can also be represented graphically. Once the uncertain parameters are modelled, all the pertinent information can be automatically provided by the framework.

3.5 Sensitivity and Uncertainty Analysis and Model Exploration

As seen in the previous subsections, the Uncertainty.jl framework can be used to write models with uncertain parameters, which are either unknown exactly or may

vary inside a given range. The framework also provides straightforward methods for performing both local and global sensitivity analysis, as well as the necessary tools to explore the behaviour of a modelled process, propagating the uncertainties through the entire process modelled. To exemplify these capabilities, the following subsections will use a hypothetical model that predicts the energy consumption of a plant as a function of four parameters. However, the methods can be used for any model, from the simplest to the most complex.

3.5.1 Local Sensitivity Analysis

Local sensitivity analysis is only a first step to better understand the process modelled, since it uses the *ceteris paribus* condition, which means that, by definition, only one parameter is changed at a time and the impact of this change on the process model is evaluated. The first step of the analysis is to study the surroundings of a given model operating point. Uncertainty.jl provides the built-in function **localSensitivity**, which can be used for three different purposes through multiple-dispatch. The first one is the simplest form of local sensitivity analysis, it expects as input the model and the nominal value of the model parameters, returning the output of the model and the local gradient. The second purpose expects the model, the nominal value of the model parameters and a percentage change of these parameters, returning the output of the model and the percentage change of this output caused by the given percentage change of the parameters. This is obtained by simulating the model, not by assuming linearity and using the gradient at the initial point. Finally, the third purpose allows a vector of percentage change, in case the parameters do not change equally. Figure 3.4 summarises the three uses of the **localSensitivity** function through an example.

3.5.2 Global Sensitivity Analysis and Model Exploration

Uncertainty.jl provides two built-in functions to explore the model and perform a global analysis, which aims at finding which parameters have the greatest relative importance to the model output. Possible interactions between the variables are considered, since the *ceteris paribus* condition is no longer assumed and any number of parameters can change simultaneously. The global sensitivity analysis is defined as the study of the impacts of such a change in the parameters on the process model. The built-in functions will, through multiple-dispatch, act differently according to

how the parameters are provided: when the parameters are described as intervals, the Latin Hypercube Sampling method is used to create samples fully stratifying the initial range of all parameters. Alternatively, if the parameters are written as probability distributions, samples are drew according to the distributions themselves. Both functions expect the model, its parameters and the size of the sample to be generated and used to run simulations.

The first built-in function, **explore**, uses the generated samples to run Monte Carlo simulations and assemble data that will generate scatter plots, which allows eyeball estimation of the influence of each parameter. The data also include the probability distribution of the model output, leading to likelihood plots, which shows how likely specific scenarios are. Regardless of how many parameters the model has, the plots allow pairwise comparisons between them and the model output.

The second built-in function, **globalSensitivity**, uses the dataset generated by the simulations to grow regression trees fitting the output of the simulations to the sample parameters acting as predictors. Surrogate splits are used with the CART method [112]. The use of regression trees can be justified by their accuracy and computational speed. However, the main reason for their use in the framework is the interpretability of the tree structures, making it easy to rank parameters by importance. This is done by summing changes in the mean squared error due to splits on every predictor and dividing the sum by the number of branch nodes. This allows the generation of data on the global impact of each parameter, leading to the global sensitivity analysis.

Figure 3.5 exemplifies the use of the **explore** and **globalSensitivity** functions when the parameters are written as intervals. The output is used to generate the plots shown in Figures 3.6 and 3.7. Notice how Figure 3.7 confirms what can be visually seen from Figure 3.6 regarding the most impactful parameters on the energy consumption. Lastly, Figure 3.8 exemplifies the use of the built-in functions with parameters written as probability distributions. The results are shown in Figures 3.9, 3.10 and 3.11.

3.6 Summary

A new framework, Uncertainty.jl, was introduced. It was written using the Julia Language and allows the rapid development of complex engineering models under uncertainty. The framework contains methods and operators which allow users to easily write down and evaluate models dealing with distributed quantities or intrinsic

uncertainties. This encompasses, for example, the modelling and representation of model uncertainties, where there can be uncertainties on the parameters and structures; processes uncertainties, where there can be uncertainties in the inputs and behaviours (outputs); and measurement uncertainties, where noises will be modelled. Once the model is written, the framework also provides tools for sensitivity and uncertainty analysis and for model exploration. Examples were provided to showcase the capabilities of the Uncertainty.jl framework, which will be further used for the AACVD modelling. The next chapter will introduce the AACVD models.

Algorithm 3.1 Overloading the function ODEProblem from the DifferentialEquations.jl package. The function generateSamples identifies which parameters are exact and creates samples for the uncertain parameters.

Input: set of differential equations **f**; initial condition $\mathbf{u_0}$; time interval $\mathbf{t_{span}}$; set of exact and uncertain parameters **allParameters**.
Output: inferred probability distribution and its properties using the solutions of the ODEs system.

```
1  function ODEProblem(f, u_0, t_span, allParameters)
2      samples := generateSamples(allParameters);
3      sol := {};
4      for each exactParameters ∈ samples do
5          prob := ODEProblem(f, y_0, t_span, exactParameters);
6          sol := sol ∪ {solve(prob)};
7      end for
8      distribution := inferDistribution(sol);
9  return distribution;
```

```
1  parameters = [228.5, 533, 827, 312]
2
3  (E, ∇model) = localSensitivity(energyConsumption, parameters)
4  (E, percentageChange₁) = localSensitivity(energyConsumption,
   parameters, 10)
5  (E, percentageChange₂) = localSensitivity(energyConsumption,
   parameters, [5, -10, -8, 4])
```

```
                    E   1984.05…
               ∇model ⌄ Vector{Float64} with 4 elements
                        -4.03…
                        6.60…
                        3.09…
                        7.34…
  percentageChange₁ ⌄ Vector{Float64} with 4 elements
                        -4.58…
                        18.9…
                        13.5…
                        12.0…
  percentageChange₂ ⌄ Vector{Float64} with 4 elements
                        -2.30…
                        -16.6…
                        -9.93…
                        4.69…
```

Figure 3.4: Built-in function **localSensitivity** used to study the model **energyConsumption**. Line 3 returns the energy consumption $E = 1984.05$ and the gradient at the point of the given parameter values. Line 4 additionally returns the percentage change of the model output when each input parameter is increased by 10% at a time. For example, the expected energy consumption will be increased by 7.34% (from 1984.05 to 2129.68) if the fourth parameter were to be increased by 10% (from 312 to 343.2). Finally, line 5 also specifies the percent change of each parameter. For example, the third parameter decreased by 8% (from 827 to 760.84) causes a 9.93% decrease in the expected energy consumption (from 1984.05 to 1789.74). The output of lines 3, 4 and 5 are shown inside the grey box.

```
1  x₁ = Interval(80, 100)
2  x₂ = Interval(50, 70)
3  x₃ = Interval(20, 40)
4  x₄ = Interval(110, 140)
5  parameters = [x₁, x₂, x₃, x₄]
6  n = 500 #sample size
7
8  data = explore(energyConsumption, parameters, n)
9  λ = globalSensitivity(energyConsumption, parameters, n)
```

Figure 3.5: Built-in functions **globalSensitivity** and **explore** used to study the model **energyConsumption** with its parameters described as intervals. The Latin Hypercube Sampling method is employed to generate 500 sample vectors containing the four model parameters, each one inside the given interval. The output of lines 8 and 9 are presented graphically in Figures 3.6 and 3.7.

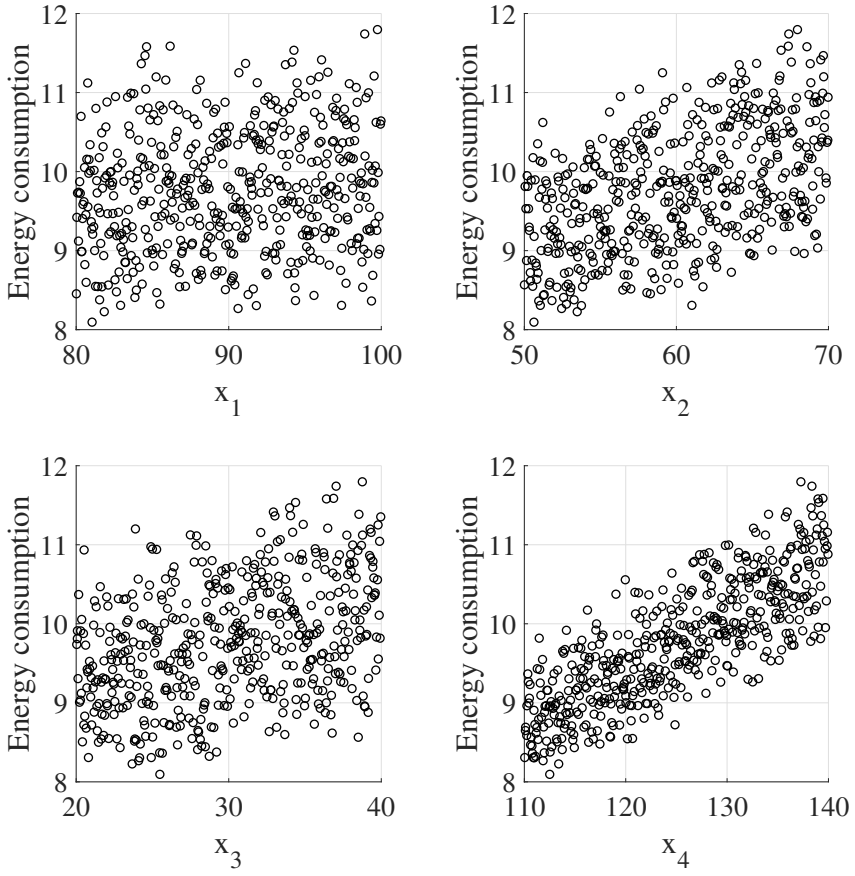

Figure 3.6: Scatter plots obtained for a pairwise analysis between the predictions of energy consumption and the parameters x_1 to x_4, whose intervals are described in Figure 3.5. It can be seen how the x_4 parameter has the greatest impact on the energy consumption. Some impact can also be observed for the the parameters x_2 and x_3, while x_1 has little impact.

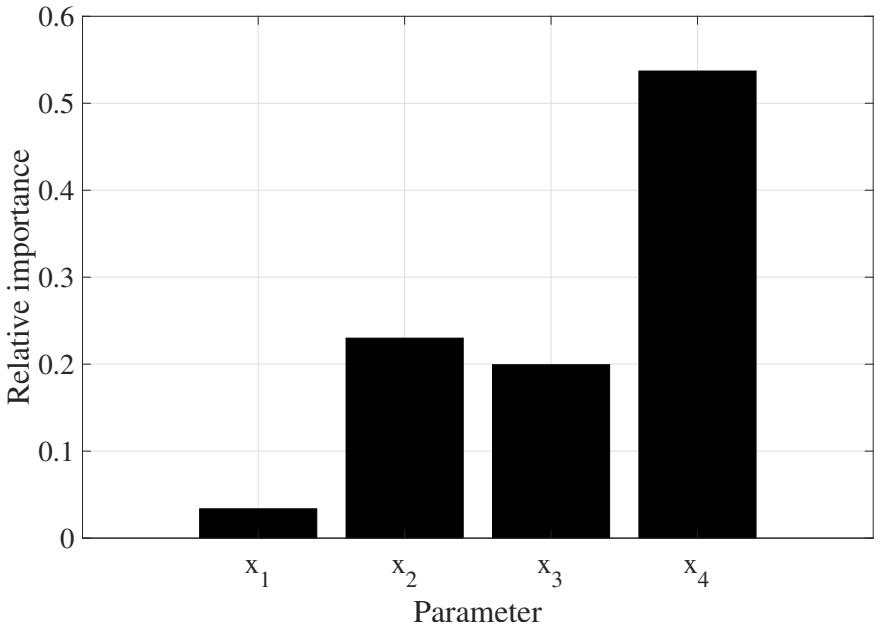

Figure 3.7: Relative importance of parameters x_1 to x_4, whose intervals are described in Figure 3.5, on the energy consumption. The results quantitatively describe what can be seen in the scatter plots of Figure 3.6, allowing global sensitivity analysis as described in Section 3.5.2.

```
1  (x₁, μ₁, σ₁²) = (ProbabilityDistribution(), 228.5, 100)
2  x₁ ~ 𝒩(μ₁,σ₁²)
3
4  (x₂, μ₂, σ₂²) = (ProbabilityDistribution(), 533, 900)
5  x₂ ~ 𝒩(μ₂,σ₂²)
6
7  (x₃, range) = (ProbabilityDistribution(), [800, 850])
8  x₃ ~ 𝒰(range)
9
10 (x₄, μ₄, σ₄²) = (ProbabilityDistribution(), 312, 400)
11 x₄ ~ 𝒩(μ₄,σ₄²)
12
13 parameters = [x₁, x₂, x₃, x₄]
14 n = 500 #sample size
15 data = explore(energyConsumption, parameters, 500)
16 λ = globalSensitivity(energyConsumption, parameters, n)
```

Figure 3.8: Built-in functions **globalSensitivity** and **explore** used to study the model **energyConsumption** with its parameters described as intervals. The given probability distributions are used to generate 500 sample vectors containing the four model parameters. The output of lines 15 and 16 are presented graphically in Figures 3.9, 3.10 and 3.11.

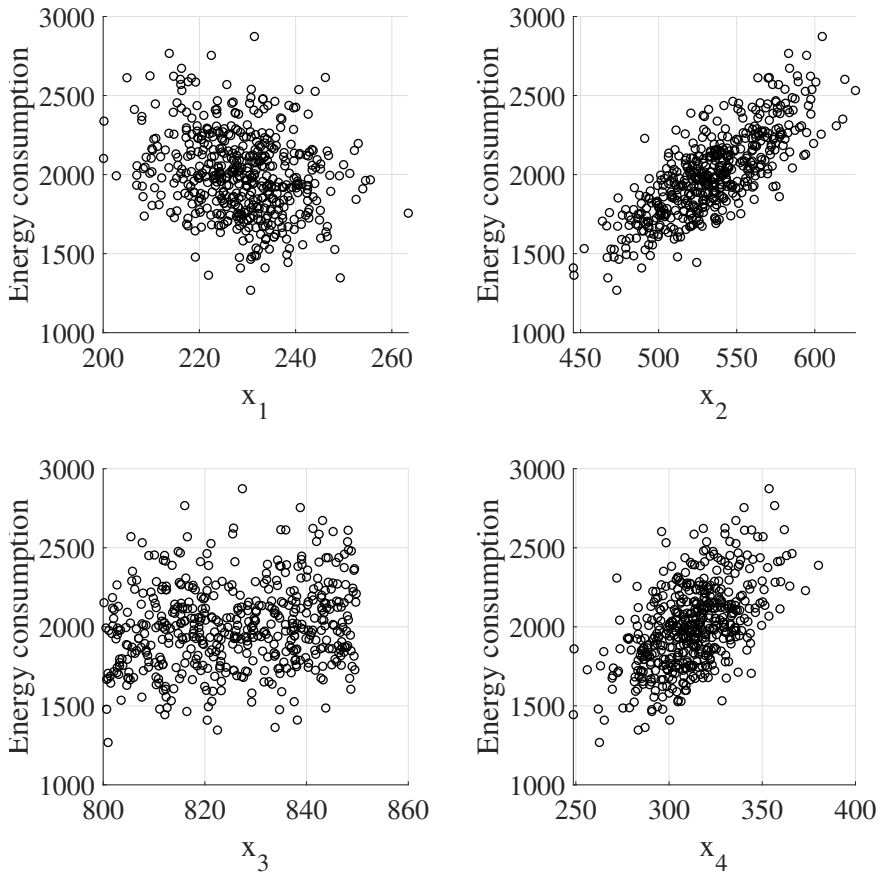

Figure 3.9: Scatter plots obtained for a pairwise analysis between the predictions of energy consumption and the parameters x_1 to x_4, whose probability distributions are described in Figure 3.8. It can be seen how parameters x_2 and x_4 have the greatest impact on the energy consumption, while parameters x_1 and x_3 have little impact.

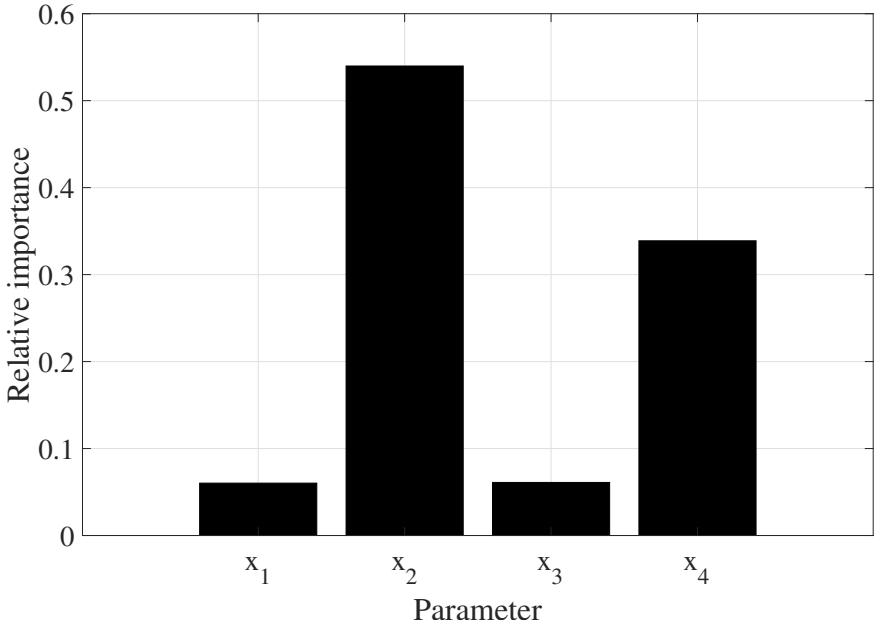

Figure 3.10: Relative importance of parameters x_1 to x_4, whose probability distributions are described in Figure 3.8, on the energy consumption. The results quantitatively describe what can be seen in the scatter plots of Figure 3.9.

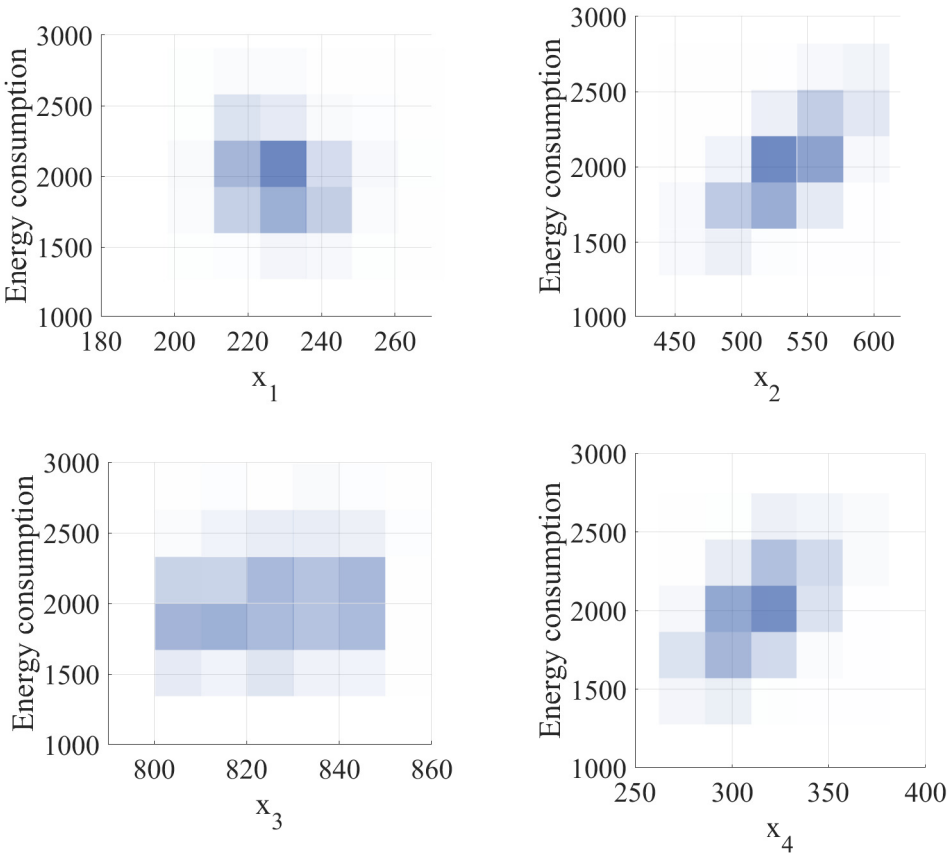

Figure 3.11: Plots showing the likelihood regions for a pairwise analysis between the predictions of energy consumption and the parameters x_1 to x_4, given the probability distributions of the model parameters as described in Figure 3.8. The darker the region, the more likely it is to represent reality.

4 AACVD Process Models

The following sections describe the models used to predict the droplet median diameter generated by ultrasonic vibration. Then, the distribution of the droplet sizes is modelled before and after a piping transport system as a function of distance travelled and of the transport system and fluid properties. Finally, models are presented to simulate the solvent evaporation and film formation.

4.1 AACVD Model-Based Scale-up and Design Procedure

In considering the design and scale-up of an AACVD process, the objective is to achieve a specific deposition rate. This objective is a function of many design variables: the choice of the precursor and the properties of the precursor solution (density, viscosity, concentration, etc.); the properties of the aerosol generator (vibration frequency, rate of aerosol generation, etc.); the properties of the transport system (diameter of the transport pipes, properties of the carrier gas and its flow rate, etc.); and, the properties of the deposition site (volume of reaction, speed of flowing glass, etc.). For the simulations, a goal seeking iterative method is used to identify the values of the design variables that achieve the desired deposition rate objective.

In a typical laboratory-scale AACVD [31, 33, 36], a precursor solution is prepared by dissolving 1-3 mmol of a precursor in 10-30 mL of a solvent. Sometimes a small quantity of a dopant is also dissolved (1-10 mol%). The precursor solution is then atomised using, for example, an ultrasonic atomiser, which produces aerosol with median droplet diameter ranging from 0.1 to 30 μm. The aerosol is transported over a small distance (5-50 cm) into the reactor, kept at a specific temperature, using a carrier gas at a constant flow-rate of 0.5-2 $\mathrm{L} \cdot \mathrm{min}^{-1}$. The substrate can be a small float glass plate of 50-100 cm^2, which is laid inside the reactor, where the chemical deposition takes place. The deposition process takes 10-30 min, from the

time aerosol starts being generated until the end of the chemical deposition.

The objective for an industrial-scale process might be, instead, to continuously deposit material on top of a glass of 3-4 m width, moving at 10-15 $m \cdot min^{-1}$, at atmospheric pressure, and at a fixed glass production temperature. As a comparative example, the process scale-up will take the laboratory-scale glass coating from the order of 1 $cm^2 \cdot min^{-1}$ to the industrial-scale order of 10 $m^2 \cdot min^{-1}$. This will substantially change the features of the process. First of all, the rates of aerosol generation and transport will change. Large-scale aerosol generation is already done, especially in the context of spray drying [113]. Additionally, the aerosol transport in the industrial process has to be in the order of tens to hundreds of metres for safety reasons, since the solvents used are often flammable and have to be kept far from the deposition site. The aerosol transport over large distances causes the loss of precursors in the piping system. Uncertainties in the transport model must be accounted for when estimating the rate of accumulation in the piping system, which could lead to clogging. Maintenance schedules can therefore be planned according to the range of possible accumulation rates and analysis of different scenarios.

Once the carrier gas reaches the deposition site, the heat and mass transfer rates will be different from the laboratory-scale. Therefore, the models will need to predict the temperature profile in the reactor using estimates for the heat transfer coefficients, which form a source of uncertainties given that they are obtained through empirical correlations. There are also uncertainties in the chemistry, specifically regarding the mechanisms of the reaction as well as the rates of gas and solid phase reactions, adsorption and desorption. Finally, choosing the solvent and reactants and quantifying the residence time for reaction will depend on the model predictions and their accuracy [54].

4.2 AACVD Process Model

The AACVD process consists of four steps, as shown in Figure 2.1, namely, aerosol generation, transport, and delivery, as well as the chemical deposition. Each of these steps is described separately but the models are integrated into a single model for use in simulating the complete process. For the sake of generality, the computation models used to simulate the process are written to independently accommodate different process specifications, which will then lead to different values for the design variables. For example, different plants will have different specifications for the distance where aerosol is generated and where the chemical deposition happens. The

process can be simulated for any process specifications. Additionally, some parameters can be fixed; for example, the industrial setting will have moving glass being continuously coated at fixed atmospheric pressure and at constant temperature.

While first principles are used to estimate some parameters, others have to be determined from experimental data. The models are easily adaptable, which facilitates, for example, the proposition of different reaction mechanisms and the procedure for parameter fitting. Consideration must be taken regarding which variables are independent of the process scale and which ones must be adjusted. Care was taken to use numbers that are representative of what could be expected in the real industrial-scale process, although the methodology presented is independent of the values adopted. Correlations for heat and mass transfer coefficients and thermophysical properties for possible precursor solutions and carrier gases were found in the literature [114–117].

The implementation of the models and description of the uncertain and distributed parameters uses Uncertainty.jl, the modelling framework introduced in the previous chapter. The models were then implemented in a concise and natural syntax, compatible with a traditional mathematical notation. For instance, kinetic constants were defined following a normal distribution with mean μ and variance σ^2 simply writing $k_1 \sim \mathcal{N}(\mu, \sigma^2)$, and then k_1 could be used in the mass balances evaluations without having to compromise between speed and code readability. The models with uncertain parameters or distributed quantities can then be simulated and the framework automatically provides their impacts on the results through the pertinent statistics.

4.3 Aerosol Generation

The first step in the process is the formation of the aerosol. There will not be a single size of drop in the aerosol generated due to the non-homogeneous ejection of droplets from the liquid surface and also the collisions and agglomerations of droplets [118]. The aerosol generated by ultrasonic vibration must therefore be described by a droplet size distribution. The *log*-normal distribution can describe variables obtained by the product of a sequence. When generating aerosol, there is a continuous process of fluid breakup, forming smaller droplets. The final droplet size is given by the product of a sequence of shrinking constants and each previous particle size, which is therefore well approximated by the log-normal distribution. The distribution only takes non-negative values, as it is the case for the droplet diameters [119].

Yasuda et al. [120] provided further evidence that the droplet diameters follow a *log*-normal distribution. The median droplet diameter $\overline{d_d}\,[\mathrm{m}]$ and the standard deviation s are enough to describe the theoretical distribution. These parameters are a function of the technique and equipment chosen for aerosol generation, as well as the properties of the fluid being atomised. For a target droplet diameter $\overline{d_d}\,[\mathrm{m}]$, the probability density function described by a *log*-normal distribution is equated as:

$$f(d_d|\overline{d_d}, s) = \frac{1}{d_d \cdot s \cdot \sqrt{2 \cdot \pi}} e^{\frac{-\left(\log d_d - \log \overline{d_d}\right)^2}{2 \cdot s^2}} \tag{4.1}$$

A common method [9] to generate aerosol droplets is by ultrasonic vibration, using a piezoelectric transducer. The breakup and formation of droplets depend on the atomiser and also on the forces that act on the sheet of solvent, such as buoyancy, drag, gravity, viscous and interfacial forces. Assuming a *log*-normal distribution for the diameter of the aerosol droplets generated, the median diameter $\overline{d_d}\,[\mathrm{m}]$ can be described by the following equation [40, 121]:

$$\overline{d_d} = 0.34 \cdot \left(\frac{8 \cdot \pi \cdot \sigma_d}{\rho_d \cdot f^2}\right)^{\frac{1}{3}} \tag{4.2}$$

where $\sigma_d\,[\mathrm{N \cdot m}]$ is the surface tension of the precursor solution, $\rho_d\,[\mathrm{kg \cdot m^{-3}}]$ is its density, and $f\,[\mathrm{Hz}]$ is the ultrasonic atomiser frequency. Note that the fluid may be a liquid precursor or a solution containing a dissolved precursor, with a concentration $C_A^{prec}\,[\mathrm{mol \cdot m^{-3}}]$ of a precursor A. Given the properties of the fluid, surface tension and density, the median droplet diameter is an inverse function of the frequency, studied from 10 kHz to 5.4 MHz [121]. Therefore, increasing the frequency will produce smaller droplets, which aids the evaporation of the solvent and the release of the precursor. Commercial ultrasonic atomisers are available for the production of droplets with sizes ranging from a fraction of a micrometre to hundreds of micrometres [122]. The non-uniformity of the droplet sizes is mainly due to the non-homogeneous ejection of droplets from the liquid surface and also the collisions and agglomerations of droplets [40, 118, 123].

While Equation 4.2 was first introduced by Lang [121], the current section expanded its applicability to represent polydisperse droplets using the *log*-normal distribution. The prediction of Equation 4.2 is now the median input for the distribution, while the standard deviation is determined from experimental results for a particular atomiser. This aerosol size distribution is a key parameter for the aerosol transport, given that the amount of aerosol that successfully crosses the transport system and its final size distribution will be different depending on the inlet size distribution.

Therefore, the output of the aerosol generation model can be used in the input of the transport model, which will be presented next.

4.4 Aerosol Transport

Frequently, the precursor chemicals are dissolved into flammable solvents. Since the deposition site is kept at a high temperature, the aerosol has to be generated at a safe distance. Suitable transport distances for industrial-scale processes range from tens to hundreds of metres. Therefore, a key element for the AACVD process scale-up is the transport of the aerosol from where it is generated to the deposition site. The aerosol transport system is usually made of straight tubes, possibly inclined, with a few bends. Losses during transport occur due to drop gravitational settling, turbulent diffusion, Brownian diffusion, and impaction in elbows [124]. Brownian diffusion has a major impact in the loss of smaller particles, for instance, the diffusivity of 0.01 μm particles is 20,000 times higher than that of 10 μm particles [125]. On the other hand, the larger droplets are affected mainly by turbulent deposition and gravitational settling, which makes them more likely to be lost during transport when compared with smaller droplets. This exemplifies the importance of modelling the full range of droplet sizes being transported, given the different amounts of aerosol loss depending on the size of the droplets. Therefore, the transport model can be used to identify the optimum range of droplet sizes for different precursor solutions, which is then used to choose the atomiser settings. Since it is impossible to completely prevent aerosol loss during transport, it becomes necessary to perform regular maintenance in the transport system.

The amount of aerosol loss grows exponentially with the pipe length [126]. Let $P_T \equiv {}^{C_{out}}/_{C_{in}}$ be defined as the total penetration, a dimensionless variable describing the fraction of aerosol particles that successfully crossed a given piping system; the aerosol content in the pipe input and output are C_{in} and C_{out}, respectively. The aerosol content can be measured, for example, by the number of aerosol droplets per unit volume. The total penetration is obtained by the product of all the individual penetration fractions, $P_T = \prod_i P_{S,i} \prod_j P_{B,j}$ where $P_{S,i}$ is the penetration for each straight pipe section i and $P_{B,j}$ is the penetration for each bend j.

4.4.1 Straight Pipes

Given a straight pipe section i of length L_i [m], the penetration $P_{S,i}$ is modelled as it was first proposed by Anand et al. [124, 126, 127]:

$$P_{S,i} = e^{-\frac{\pi \cdot d \cdot V_{e,i}}{Q} L_i} \tag{4.3}$$

where d [m] is the pipe diameter and Q [$\mathrm{m}^3 \cdot \mathrm{s}^{-1}$] is the fluid flow rate. $V_{e,i}$ [$\mathrm{m} \cdot \mathrm{s}^{-1}$] is defined as the effective velocity of aerosol loss, as a function of the three main mechanisms: Brownian diffusion, turbulent diffusion, and gravitational settling.

Using a cylindrical coordinate system with the polar axis in the radial direction and the longitudinal axis in the pipe direction; for a cross-section of the pipe, the effective velocity is a function of the radial distance r [m] and the angular coordinate θ [rad], which leads to the differential:

$$\delta V_{e,i} = \frac{\partial V_{e,i}}{\partial r} \delta r + \frac{\partial V_{e,i}}{\partial \theta} \delta \theta \tag{4.4}$$

This equation can be simplified considering that the aerosol is homogeneously distributed in any pipe cross-section. Experimental data [124, 128, 129] confirms that such an assumption is acceptable for the transport system that will be applied to the AACVD process. Therefore, the first term on the right-hand side of Equation 4.4 vanishes and an ordinary differential equation is obtained, $\delta V_{e,i} = \frac{\partial V_{e,i}}{\partial \theta} \delta \theta$, which can be analytically solved, leading to the following algebraic equation:

$$V_{e,i} = \begin{cases} \frac{\theta_c V_{tB}}{\pi} + \frac{V_{tB}}{2} + \frac{V_g \cdot \cos \theta_c}{\pi} & V_g \geq V_{tB} \\ V_{tB} & \text{otherwise} \end{cases} \tag{4.5}$$

where different parameters are used, as subsequently described. Anand et al. [124] gave some insights on the derivation of the above equation, based on writing $\frac{\partial V_{e,i}}{\partial \theta}$ as a function of different mechanisms that will be described below and integrating over the full cross-sectional circumference interval, $0 \leq \theta \leq 2\pi$. To calculate the effective velocity using Equation 4.5, several parameters must be first calculated. The parameter V_{tB} [$\mathrm{m} \cdot \mathrm{s}^{-1}$] is defined as a function of the turbulent diffusion velocity, V_t [$\mathrm{m} \cdot \mathrm{s}^{-1}$], and the Brownian diffusion velocity, V_B [$\mathrm{m} \cdot \mathrm{s}^{-1}$]:

$$V_{tB} = V_t + 10^{k_b} \cdot V_B \tag{4.6}$$

where k_b is a constant, which Anand et al. [124] suggested the use of $k_b = 0$. However, as a novel contribution, the value for the constant was set as $k_b = -4.3$. This is because when $k_b = 0$ is used, the deposition due to Brownian diffusion has a

major and growing impact in the droplet deposition as the droplet diameters get smaller than a certain threshold, which depends on the fluid and transport system characteristics. Notice that, according to Equation 4.7, bigger droplets (greater d_d) will have greater mass (m_d) and, therefore, the Brownian diffusion velocity will be smaller, meaning that Brownian motion would have less impact on the particle deposition. Since Anand et al. used experimental data for droplet sizes considerably greater than the threshold, their results are consistent. However, the aerosol generated for the AACVD process has droplet size distributions which also accounts for droplets smaller than the threshold. Therefore, further experimental results were used to test the model. Using data from Brockmann et al. [130] and also by Lee and Gieseke [131], the constant was fitted to $k_b = -4.3$, which shifted the impact of Brownian diffusion to smaller droplets, in a way that minimised the mismatch between the model and the reported experimental results. After the correction, the model also better agreed with experiments performed in the context of this thesis, as it will be described in Section 5.3.2 and already published [132].

The Brownian diffusion velocity, $V_B\,[\mathrm{m}\cdot\mathrm{s}^{-1}]$, is given by:

$$V_B = \sqrt{\frac{k_B \cdot T}{2 \cdot \pi \cdot m_d}} \tag{4.7}$$

where $k_B = 1.38 \cdot 10^{-23}\,\mathrm{m}^2 \cdot \mathrm{kg} \cdot \mathrm{s}^{-2} \cdot \mathrm{K}^{-1}$ is the Boltzmann constant, $T\,[\mathrm{K}]$ is the carrier fluid temperature, and $m_d\,[\mathrm{kg}]$ is the droplet mass. Given the droplet diameter $d_d\,[\mathrm{m}]$ and the droplet density $\rho_d\,[\mathrm{kg}\cdot\mathrm{m}^{-3}]$, assuming spherical droplets, it is possible to calculate their mass $m_d\,[\mathrm{kg}]$ by:

$$m_d = \rho_d \cdot \left(\frac{\pi \cdot d_d^3}{6}\right) \tag{4.8}$$

The turbulent diffusion velocity $V_t\,[\mathrm{m}\cdot\mathrm{s}^{-1}]$ is given by:

$$V_t = \frac{V_f \cdot (V_s + V_r)}{4} \tag{4.9}$$

where $V_f\,[\mathrm{m}\cdot\mathrm{s}^{-1}]$ is the friction velocity. Two dimensionless depositional velocities are used: V_s and V_r. The friction velocity is calculated by:

$$V_f = U \cdot \left(\frac{f}{2}\right)^{\frac{1}{2}} \tag{4.10}$$

where $U\,[\mathrm{m}\cdot\mathrm{s}^{-1}]$ is the mean fluid velocity and f is the dimensionless Fanning friction factor. The mean velocity of the carrier fluid can be calculated by:

$$U = \frac{4 \cdot Q}{\pi \cdot d^2} \tag{4.11}$$

where $Q\,[\mathrm{m}^3 \cdot \mathrm{s}^{-1}]$ is the carrier fluid flow rate and $d\,[\mathrm{m}]$ is the pipe diameter. The Fanning friction factor can be approximated by the Blasius correlation:

$$f = \frac{0.316}{4 \cdot Re^{\frac{1}{4}}} \tag{4.12}$$

where Re is the dimensionless Reynolds number based on the tube diameter $d\,[\mathrm{m}]$. Equation 4.12 was experimentally tested for $3,000 < Re < 100,000$. The Reynolds number is calculated by:

$$Re = \frac{U \cdot d \cdot \rho}{\mu} \tag{4.13}$$

where $U\,[\mathrm{m} \cdot \mathrm{s}^{-1}]$ is the mean fluid velocity, calculated by Equation 4.11, $d\,[\mathrm{m}]$ is the tube diameter, $\rho\,[\mathrm{kg} \cdot \mathrm{m}^{-3}]$ is the carrier fluid density and $\mu\,[\mathrm{N} \cdot \mathrm{s} \cdot \mathrm{m}^{-2}]$ is its dynamic viscosity.

To evaluate the parameters V_s and V_r, it is necessary to calculate the dimensionless modified stopping distances S and R. The first one is given by:

$$S = \frac{\rho \cdot V_f}{\mu} \cdot \left(0.9 \cdot \tau \cdot V_f + \frac{d_d}{2}\right) \tag{4.14}$$

where $\rho\,[\mathrm{kg} \cdot \mathrm{m}^{-3}]$ is the carrier fluid density, $V_f\,[\mathrm{m} \cdot \mathrm{s}^{-1}]$ is the friction velocity, calculated by Equation 4.10, $\mu\,[\mathrm{N} \cdot \mathrm{s} \cdot \mathrm{m}^{-2}]$ is the carrier fluid dynamic viscosity, $d_d\,[\mathrm{m}]$ is the droplet diameter and $\tau_r\,[\mathrm{s}]$ is the relaxation time, given by:

$$\tau_r = \frac{C \cdot \rho_d \cdot d_d^2}{18 \cdot \mu} \tag{4.15}$$

where $\rho_d\,[\mathrm{kg} \cdot \mathrm{m}^{-3}]$ is the droplet density, $d_d\,[\mathrm{m}]$ is the droplet diameter, $\mu\,[\mathrm{N} \cdot \mathrm{s} \cdot \mathrm{m}^{-2}]$ is the carrier fluid dynamic viscosity and C is the Cunningham slip correction, given by:

$$C = 1 + \frac{\lambda}{d_d} \cdot \left(2.34 + 1.05 \cdot e^{-0.39\frac{d_d}{\lambda}}\right) \tag{4.16}$$

where $\lambda\,[\mathrm{m}]$ is the mean free path of the carrier fluid and $d_d\,[\mathrm{m}]$ is the droplet diameter.

The dimensionless distance R is given by:

$$R = \frac{d_d \cdot V_f \cdot \rho}{2 \cdot \mu} \tag{4.17}$$

where $d_d\,[\mathrm{m}]$ is the droplet diameter, $V_f\,[\mathrm{m}\cdot\mathrm{s}^{-1}]$ is the friction velocity, calculated by Equation 4.10, $\rho\,[\mathrm{kg}\cdot\mathrm{m}^{-3}]$ is the carrier fluid density and $\mu\,[\mathrm{N}\cdot\mathrm{s}\cdot\mathrm{m}^{-2}]$ is the carrier fluid dynamic viscosity.

Using the dimensionless distances S and R, it is possible to calculate the two dimensionless depositional velocities, V_s and V_r, using the following equations, depending on the value obtained for S and R:

$$V_s = \begin{cases} 0.05 \cdot S & 0 \leq S < 10 \\ 0.5 + 0.0125 \cdot (S - 10) & 10 \leq S < 30 \end{cases} \tag{4.18}$$

$$V_r = \begin{cases} 0.05 \cdot R & 0 \leq R < 10 \\ 0.5 + 0.0125 \cdot (R - 10) & 10 \leq R < 30 \end{cases} \tag{4.19}$$

After calculating V_s and V_r, it is possible to go back to Equation 4.9 and calculate the turbulent diffusion velocity, $V_t\,[\mathrm{m}\cdot\mathrm{s}^{-1}]$, also using the friction velocity $V_f\,[\mathrm{m}\cdot\mathrm{s}^{-1}]$, calculated by Equation 4.10.

The component of the gravitational settling velocity $V_g\,[\mathrm{m}\cdot\mathrm{s}^{-1}]$ perpendicular to the flow direction is calculated by:

$$V_g = \tau_r \cdot g \cdot \cos(\varphi) \tag{4.20}$$

where $g = 9.81\,\mathrm{m}\cdot\mathrm{s}^{-2}$ is the standard gravity, $\varphi\,[\mathrm{rad}]$ is the inclination angle of the pipe relative to the horizontal direction, as shown in Figure 4.1, and $\tau_r\,[\mathrm{s}]$ is the relaxation time, given by Equation 4.15.

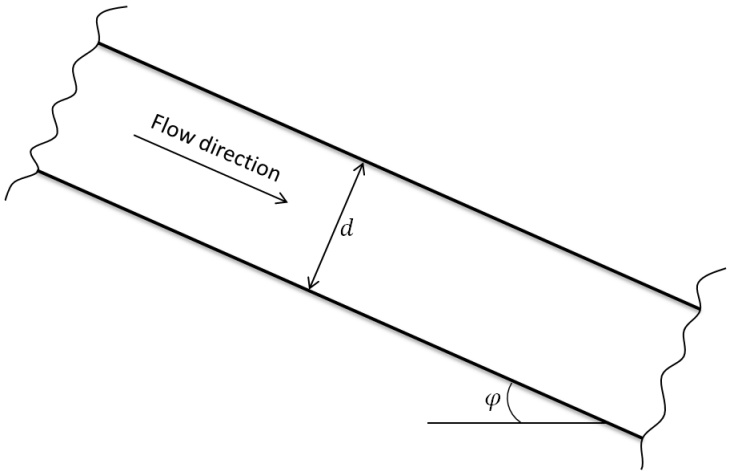

Figure 4.1: Schematics of inclined pipe.

Finally, the critical angle $\theta_c\,[\mathrm{rad}]$ is given by:

$$\theta_c = \arcsin\left(\frac{V_{tB}}{V_g}\right) \tag{4.21}$$

where $V_{tB}\,[\mathrm{m}\cdot\mathrm{s}^{-1}]$ is the combination, given by Equation 4.6, of the turbulent diffusion velocity and the Brownian diffusion velocity; $V_g\,[\mathrm{m}\cdot\mathrm{s}^{-1}]$ is the gravitational settling velocity component perpendicular to the flow direction, calculated by Equation 4.20.

Now it is possible to calculate the effective velocity $V_{e,i}\,[\mathrm{m}\cdot\mathrm{s}^{-1}]$ using Equation 4.5 and the penetration $P_{S,i}$ using Equation 4.3. For more information about the equations used to calculate the effective velocity $V_{e,i}\,[\mathrm{m}\cdot\mathrm{s}^{-1}]$, including the reasoning for the definition of the critical angle $\theta_c\,[\mathrm{rad}]$, refer to McFarland et al. [124, 127].

4.4.2 Bends

For each bend j, the penetration $P_{B,j}$ is modelled as it was first proposed by Cheng et al. [133–135]:

$$\begin{aligned} P_{B,j} = 1 - \frac{1}{\pi\cdot r_0}\Bigg[&\left(\frac{(\sin\alpha)^2\cdot e^{2\cdot\mathit{\Gamma}_\alpha}}{(\eta(\mathit{\Gamma}_\alpha))^2} - 1\right)\cdot\left(z_\alpha\cdot\left(r_0^2+1\right) - \frac{z_\alpha^3}{3}\right) \\ &+ r_0\cdot\left(\frac{(\sin\alpha)^2\cdot e^{2\cdot\mathit{\Gamma}_\alpha}}{(\eta(\mathit{\Gamma}_\alpha))^2} + 1\right)\cdot\left(z_\alpha\cdot\sqrt{1-z_\alpha^2} + \arcsin(z_\alpha)\right)\Bigg] \end{aligned} \tag{4.22}$$

where r_0 is the dimensionless curvature ratio, defined as the bend radius $r_b\,[\mathrm{m}]$ divided by the tube radius $r\,[\mathrm{m}]$; $\alpha\,[\mathrm{rad}]$ is the bend angle, Γ_α is the dimensionless time at impact, which is obtained by solving Equation 4.29; η is a dimensionless coordinate given by Equation 4.23, function of the dimensionless time Γ; z_α is the z-axis coordinate at impact and it is given by Equation 4.28. The bend angle $\alpha\,[\mathrm{rad}]$, bend radius $r_b\,[\mathrm{m}]$ and tube radius $r\,[\mathrm{m}]$ are represented in Figure 4.2.

The dimensionless coordinates η and ξ are functions of the dimensionless time Γ and are equated as:

$$\begin{aligned} \eta(\Gamma) = \sin(B\cdot\Gamma)\cdot&\left(\sinh(A\cdot\Gamma) + \cosh(A\cdot\Gamma)\cdot\left(\frac{A^3}{A^2+B^2}\right)\right) \\ &+ (\cos(B\cdot\Gamma)\cdot\sinh(A\cdot\Gamma))\cdot\left(\frac{B^3}{A^2+B^2}\right) \end{aligned} \tag{4.23}$$

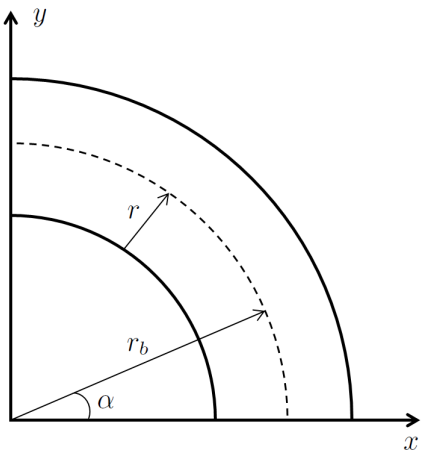

Figure 4.2: Schematics of a pipe bend.

$$\xi(\Gamma) = \cos(B \cdot \Gamma) \cdot \left(\cosh(A \cdot \Gamma) + \sinh(A \cdot \Gamma) \cdot \left(\frac{A^3}{A^2 + B^2} \right) \right) - (\sin(B \cdot \Gamma) \cdot \cosh(A \cdot \Gamma)) \cdot \left(\frac{B^3}{A^2 + B^2} \right) \tag{4.24}$$

where the two auxiliary variables, A and B, are given by:

$$A = \sqrt{\frac{1 + \sqrt{1 + \left(\frac{4 \cdot Stk}{r_0}\right)^2}}{2}} \tag{4.25}$$

$$B = \frac{4 \cdot Stk}{2 \cdot A \cdot r_0} \tag{4.26}$$

where r_0 is the dimensionless curvature ratio and Stk is the dimensionless Stokes number, given by:

$$Stk = \frac{2 \cdot \tau \cdot U}{d} \tag{4.27}$$

where τ [s] is the relaxation time, calculated by Equation 4.15, U [m · s^{-1}] is the mean fluid velocity, calculated by Equation 4.11 and d [m] is the tube diameter.

The z-axis coordinate at impact, z_α, is given by:

$$z_\alpha = \sqrt{1 - \frac{r_0^2 \cdot (\eta(\Gamma_\alpha) - e^{\Gamma_\alpha} \cdot \sin\alpha)^2}{(\eta(\Gamma_\alpha) + e^{\Gamma_\alpha} \cdot \sin\alpha)^2}} \tag{4.28}$$

where r_0 is the dimensionless curvature ratio, α [rad] is the bend angle and η is the dimensionless coordinate given by Equation 4.23, evaluated for the dimensionless

time at impact, Γ_α, which is obtained using the dimensionless coordinates η and ξ, from Equations 4.23 and 4.24, and solving the following equation:

$$\tan \alpha = \frac{\eta \left(\Gamma_\alpha \right)}{\xi \left(\Gamma_\alpha \right)} \tag{4.29}$$

The correlations above are based on experimental data [124, 126, 127, 133–135] and were tested for wide ranges of Stokes and Reynolds numbers.

4.4.3 Coiled Pipes

For the model validation, as it will be presented in Section 5.3, the transport piping system was customised in a coiled fashion. This allowed the use of up to 50 m of transport piping length and also to stress test the model. However, the aerosol transport model previously presented in Section 4.4 cannot be used straight away, given the coiled setting for the transport system. Some calculations are therefore necessary before using the transport model. Firstly, the schematics shown in Figure 5.19 is the approximation used to model the experimental transport system. The coil radius, defined as r_c [m], coincides with the bend radius shown in Figure 4.2. If the coiled pipe length is l [m], the number of turns, defined as N, is given by:

$$N = \frac{l}{2 \cdot \pi \cdot r_c} \tag{4.30}$$

The inclination of the pipe, φ [rad], can be modelled as:

$$\varphi = \arctan \frac{r}{r_c} \tag{4.31}$$

where the coil radius, r_c [m], and the tubing radius, r [m], are used.

The aerosol penetration fraction for the coiled section, P_c, is then calculated as:

$$P_c = P_l \cdot P_b^{4 \cdot N} \tag{4.32}$$

where P_l is calculated by the model presented in Section 4.4.1, using the pipe inclination φ [rad] given by Equation 4.31 and coiled pipe length l [m]; P_b is calculated by the model presented in Section 5.2.2, using $\alpha = \frac{\pi}{2}$ rad.

The model proposed above for the coiled pipe setting is novel. It was built upon the models for straight pipes and bends, which were first introduced by Anand et al. [124, 127, 133]. Such models were presented above in Sections 4.4.1 and 4.4.2. However, the original models were built for a different application and could not be used as they were in the context of an AACVD transport system, since the

models did not originally cope with the smallest droplets of the distribution. The model modifications that were proposed to solve such an issue also form a novel contribution of this thesis. Given that for the AACVD process the transport system will be at room temperature and with low aerosol concentration, the effects of aerosol evaporation and coalescence during transport were neglected.

4.5 Aerosol Delivery

Once the aerosol droplets leave the transport system, which is likely to be at room temperature, they enter a region that is heated. This happens when the carrier gas travels through the middle of the distributor beam, as can be seen in Figure 2.1 (bottom right-hand side), where the filled rectangles represent heat exchangers. The solvent will dry out and the precursors will be released. As the carrier gas travels through the heated delivery section, its temperature will increase with time. Conservation of energy leads to the steady-flow thermal energy equation, which describes how the temperature of the carrier gas will increase with time:

$$\frac{\mathrm{d}T}{\mathrm{d}t} = \frac{v_g \cdot h_1 \cdot P \cdot (T_w - T)}{\dot{m} \cdot c_p} \tag{4.33}$$

where $T\,[\mathrm{K}]$ is the carrier gas mean temperature; $t\,[\mathrm{s}]$ is time; $v_g\,[\mathrm{m \cdot s^{-1}}]$ is the carrier gas velocity; $h_1\,[\mathrm{W \cdot m^{-2} \cdot K^{-1}}]$ is the heat transfer coefficient; $P\,[\mathrm{m}]$ is the surface perimeter; $T_w\,[\mathrm{K}]$ is the wall temperature; $\dot{m}\,[\mathrm{kg \cdot s^{-1}}]$ and $c_p\,[\mathrm{J \cdot kg^{-1} \cdot K^{-1}}]$ are, respectively, the carrier gas mass flow rate and specific heat at constant pressure. The droplet evaporation is modelled by mass and energy balances. The process can be divided into two stages: the first one is the reduction of the droplet diameter, given the evaporation of the aerosol. For the second stage, the moisture content reaches a critical value and the solid precursors start to appear. As the precursor is further heated, it will transition to the vapour phase, allowing the chemical vapour deposition to take place. In addition to Equation 4.33, another two differential equations are numerically solved simultaneously [114, 116]:

$$\begin{aligned} \frac{\mathrm{d}}{\mathrm{d}t}T_d &= \frac{1}{c_{p,d} \cdot m_d}\left(h_2 \cdot \pi \cdot d_d^2 \cdot (T - T_d) - h_{vap,d} \cdot \dot{m}_v\right) \\ \frac{\mathrm{d}}{\mathrm{d}t}d_d &= -\frac{2 \cdot \dot{m}_v}{\rho_d \cdot \pi \cdot d_d^2} \end{aligned} \tag{4.34}$$

where $h_{vap,d}\,[\mathrm{J \cdot kg^{-1}}]$ is the droplet specific heat of evaporation; $c_{p,d}\,[\mathrm{J \cdot kg^{-1} \cdot K^{-1}}]$, $m_d\,[\mathrm{kg}]$, $\rho_d\,[\mathrm{kg \cdot m^{-3}}]$, $T_d\,[\mathrm{K}]$ and $d_d\,[\mathrm{m}]$ are, respectively, the droplet specific heat

at constant pressure, mass, density, temperature, and diameter; $t\,[\mathrm{s}]$ is time; $h_2\,[\mathrm{W}\cdot\mathrm{m}^{-2}\cdot\mathrm{K}^{-1}]$ is the heat transfer coefficient; $T\,[\mathrm{K}]$ is the carrier gas mean temperature; $\dot{m}_v\,[\mathrm{kg}\cdot\mathrm{s}^{-1}]$ is the mass transfer rate, given by:

$$\dot{m}_v = h_{m,s}\cdot(\rho_{v,s}-\rho_{v,\infty})\cdot\pi\cdot d_d^2 \tag{4.35}$$

where $h_{m,s}\,[\mathrm{m}\cdot\mathrm{s}^{-1}]$ is the solvent mass transfer coefficient; $\rho_{v,s}\,[\mathrm{kg}\cdot\mathrm{m}^{-3}]$ and $\rho_{v,\infty}\,[\mathrm{kg}\cdot\mathrm{m}^{-3}]$ are, respectively, the partial vapour densities over the droplet surface and far from it. Mass and heat transfer coefficients are calculated using different empirical correlations. These correlations will change according to the flow pattern, turbulent or laminar, and will be valid for different ranges of the appropriate Reynolds number. The correlations are written in terms of two dimensionless numbers, Nusselt number (Nu) and Sherwood number (Sh), which are then used to calculate, respectively, the heat and mass transfer coefficients. The first heat transfer coefficient, $h_1\,[\mathrm{W}\cdot\mathrm{m}^{-2}\cdot\mathrm{K}^{-1}]$, is calculated as:

$$h_1 = \frac{Nu_g\cdot k_g}{D_h} \tag{4.36}$$

where Nu_g is the Nusselt number relative to the carrier gas; $k_g\,[\mathrm{W}\cdot\mathrm{m}^{-1}\cdot\mathrm{K}^{-1}]$ is the carrier gas thermal conductivity; and $D_h\,[\mathrm{m}]$ is the flow hydraulic diameter, defined as:

$$D_h = \frac{4\cdot A_c}{P} \tag{4.37}$$

where $A_c\,[\mathrm{m}^2]$ is the cross-sectional area and $P\,[\mathrm{m}]$ is the perimeter of the flow.

The second heat transfer coefficient is calculated as:

$$h_2 = \frac{Nu_d\cdot k_g}{d_d} \tag{4.38}$$

where $k_g\,[\mathrm{W}\cdot\mathrm{m}^{-1}\cdot\mathrm{K}^{-1}]$ is the carrier gas thermal conductivity; $d_d\,[\mathrm{m}]$ is the droplet diameter; and Nu_d is the Nusselt number relative to the droplet, given by:

$$Nu_d = \left(2 + 0.6\cdot Re_d^{1/2}\cdot Pr^{1/3}\right)\cdot(1+C)^{-0.7} \tag{4.39}$$

where Pr is the dimensionless Prandtl number, Re_d is the Reynolds number relative to the droplet given by Equation 4.40 and C is the Spalding number, given by Equation 4.41:

$$Re_d = \frac{U\cdot d_d\cdot\rho}{\mu} \tag{4.40}$$

$$C = \frac{c_{p,v} \cdot (T - T_d)}{h_{fg}} \tag{4.41}$$

where $U\,[\mathrm{m \cdot s^{-1}}]$ is the mean velocity of the carrier gas, calculated by Equation 4.11; $d_d\,[\mathrm{m}]$ is the droplet diameter; $\rho\,[\mathrm{kg \cdot m^{-3}}]$ is the carrier gas density; and $\mu\,[\mathrm{N \cdot s \cdot m^{-2}}]$ is the carrier gas dynamic viscosity; $c_{p,v}\,[\mathrm{J \cdot kg^{-1} \cdot K^{-1}}]$ is the solvent vapour specific heat; $T\,[\mathrm{K}]$ is the carrier gas mean temperature; $T_d\,[\mathrm{K}]$ is the droplet temperature; and $h_{fg}\,[\mathrm{J \cdot kg^{-1}}]$ is the solvent specific heat of evaporation.

The mass transfer coefficient is calculated as:

$$h_{m,s} = \frac{Sh_d \cdot D_v}{d_d} \tag{4.42}$$

where Sh_d is the dimensionless Sherwood number, calculated by Equation 4.43; $D_v\,[\mathrm{m^2 \cdot s^{-1}}]$ is the solvent vapour diffusion coefficient.

$$Sh_d = \left(2 + 0.6 \cdot Re_d^{1/2} \cdot Sc^{1/3}\right) \cdot (1 + C)^{-0.7} \tag{4.43}$$

where Re_d is the Reynolds number relative to the droplet given by Equation 4.40, Sc is the dimensionless Schmidt number; C is the Spalding number, given by Equation 4.41; $T_d\,[\mathrm{K}]$ is the droplet temperature; and $T\,[\mathrm{K}]$ is the carrier gas mean temperature.

The delivery models can account for uncertainties in parameters that are calculated from empirical equations. For example, the partial vapour densities, the Prandtl and Schmidt numbers and the solvent vapour diffusion coefficient are calculated using specific correlations [117], as a function of the temperature and the choice of precursors and solvents.

The temperature profile of the carrier gas shown in Equation 4.33 was obtained via energy balance. On the other hand, the solvent evaporation model shown in Equation 4.34 was first introduced by Mezhericher et al. [114]. In the context of the AACVD process, this thesis connected the two models to be able to describe how the solvent evaporates once the carrier gas is heated and the precursors are released. The film formation can then take place and the modelling for that is presented next.

4.6 Chemical Deposition and Film Formation

The delivery model predicts the temperature profile in the deposition site and the rate of solvent evaporation. Now, the deposition reactions occur in gas and solid

phases and consist of multiple steps happening both in series and in parallel. Before obtaining the final product, there may be both detectable and undetectable intermediates and undesired reaction impurities [52]. Building a robust chemical process, with reproducible reaction performance, would require the understanding of the mechanisms and the competing rates of reactions, as well as the interplay between kinetic effects, mass transfer and energy-related effects. Sophisticated methodologies can be used to study the mechanism and kinetics of specific reactions as, for example, Wang et al. [136] did using an in-situ environmental scanning electron microscopy for the production of single-layer graphene growth on platinum foils. This is a first step to build specific mathematical models to describe that reaction in particular. Many other studies have been conducted to study synthetic methodologies, mechanisms and kinetics of deposition for different materials, as well as the correlation between properties [39, 137–149].

As an alternative, a general modelling methodology is proposed that requires simpler measurements, such as the film growth rate and some idea of the mechanisms involved. The objective is to have models that are independent from the full understanding of the mechanisms for each reaction, avoiding the cost of a thorough investigation towards the phase, composition and morphology of the deposition products. It is important to recognise that the accuracy and generality of predictions given by the simplified models are dictated by the amount of experimental data and the level of mechanistic understanding when building them. The parameters can, however, have their values improved with more experiments, which can be guided by the models using principles from model-based design of experiments. Alternatively, when there is a set of well studied and understood specific reactions and their mechanisms, more sophisticated models can be used [150–154].

Modelling the film formation can bring insights about the chemical mechanisms and the competition between mass transfer and reaction kinetics, which will affect the final products. The objective is, therefore, to model specifically the laboratory-scale CVD batch reactor and to generalise the results to the industrial-scale process. This means that a migration is necessary from sequential batch depositions in the laboratory to continuous deposition on top of a flowing glass in the industrial setting. In both cases, when the aerosol reaches the reaction chamber, the solvent evaporates and chemical reactions take place, resulting in the film formation.

Equation 4.44 represents a set of steps to describe a hypothetical chemical vapour deposition mechanism, namely, the mass transfer (diffusion) of each chemical species from the bulk gas (subscript g) to the interface with the solid (subscript int) and vice versa, adsorption onto the surface (subscript ad), desorption from the surface,

and the chemical reactions:

$$
\begin{aligned}
A_{(g)} &\underset{K_{eq_1}}{\rightleftharpoons} A_{(int)} \\
B_{(g)} &\underset{K_{eq_2}}{\rightleftharpoons} B_{(int)} \\
C_{(g)} &\underset{K_{eq_3}}{\rightleftharpoons} C_{(int)} \\
D_{(g)} &\underset{K_{eq_4}}{\rightleftharpoons} D_{(int)} \\
A_{(int)} + S_1 &\underset{K_{eq_5}}{\rightleftharpoons} A_{(ad)} \\
B_{(int)} + S_2 &\underset{K_{eq_6}}{\rightleftharpoons} B_{(ad)} \\
C_{(int)} + S_3 &\underset{K_{eq_7}}{\rightleftharpoons} C_{(ad)} \\
D_{(int)} + S_4 &\underset{K_{eq_8}}{\rightleftharpoons} D_{(ad)} \\
A_{(g)} &\underset{K_{eq_9}}{\rightleftharpoons} B_{(g)} + C_{(g)} \\
A_{(s)} &\underset{K_{eq_{10}}}{\rightleftharpoons} B_{(s)} + C_{(s)} \\
B_{(s)} &\underset{K_{eq_{11}}}{\rightleftharpoons} C_{(s)} + D_{(s)}
\end{aligned}
\tag{4.44}
$$

where A is a precursor, whose properties affects the aerosol generation, transport and delivery; B is an intermediate; C is a by-product; D is the main product forming the film; S_i is an empty sorption site i; K_{eq_i} is an equilibrium constant of reaction i. Considering only the chemical reactions and assuming that they are close to irreversible, Equation 4.45 is obtained:

$$
\begin{aligned}
A_{(g)} &\overset{\text{gas}}{\underset{k_1}{\longrightarrow}} B_{(g)} + C_{(g)} \\
B_{(s)} &\overset{\text{surface}}{\underset{k_2}{\longrightarrow}} C_{(s)} + D_{(s)} \\
A_{(s)} &\overset{\text{surface}}{\underset{k_3}{\longrightarrow}} 2C_{(s)} + D_{(s)}
\end{aligned}
\tag{4.45}
$$

where k_i [units vary] is the kinetic constant of reaction i, in the gas phase or on the surface. Notice that $A_{(s)} \overset{\text{surface}}{\underset{k_3}{\longrightarrow}} 2C_{(s)} + D_{(s)}$ is obtaining from combining $A_{(s)} \overset{\text{surface}}{\longrightarrow} B_{(s)} + C_{(s)}$ with $B_{(s)} \overset{\text{surface}}{\longrightarrow} C_{(s)} + D_{(s)}$. An example of reaction following the above mechanism is the conversion of monosilane for the production of high-grade polysilicon [155]. The deposition rate is affected by thermodynamic, kinetic and mass diffusion factors, any of which may be dominant depending on the operating conditions of the reactor [156]. Those factors are described in the dynamic model for the laboratory batch reactor, which can be obtained by performing material balances:

$$
\begin{aligned}
\frac{\mathrm{d}}{\mathrm{d}t}n_A^g &= \dot{F}_{in}\cdot C_A^{in} - \dot{F}_{out}\cdot\frac{n_A^g}{V} - h_{m,A}\cdot A\cdot\left(\frac{n_A^g}{V}-\frac{n_A^s}{V_{int}}\right) - k_1\cdot n_A^g\\
\frac{\mathrm{d}}{\mathrm{d}t}n_A^s &= A\cdot h_{m,A}\cdot\left(\frac{n_A^g}{V}-\frac{n_A^s}{V_{int}}\right) - A\cdot k_3\cdot\frac{n_A^s}{V_{int}}\\
\frac{\mathrm{d}}{\mathrm{d}t}n_B^g &= \dot{F}_{in}\cdot C_B^{in} - \dot{F}_{out}\cdot\frac{n_B^g}{V} - h_{m,B}\cdot A\cdot\left(\frac{n_B^g}{V}-\frac{n_B^s}{V_{int}}\right) + k_1\cdot n_A^g\\
\frac{\mathrm{d}}{\mathrm{d}t}n_B^s &= A\cdot h_{m,B}\cdot\left(\frac{n_B^g}{V}-\frac{n_B^s}{V_{int}}\right) - A\cdot k_2\cdot\frac{n_B^s}{V_{int}}\\
\frac{\mathrm{d}}{\mathrm{d}t}n_C^g &= \dot{F}_{in}\cdot C_C^{in} - \dot{F}_{out}\cdot\frac{n_C^g}{V} - h_{m,C}\cdot A\cdot\left(\frac{n_C^g}{V}-\frac{n_C^s}{V_{int}}\right) + k_1\cdot n_A^g\\
\frac{\mathrm{d}}{\mathrm{d}t}n_C^s &= A\cdot h_{m,C}\cdot\left(\frac{n_C^g}{V}-\frac{n_C^s}{V_{int}}\right) + A\cdot k_2\cdot\frac{n_B^s}{V_{int}} + 2\cdot A\cdot k_3\cdot\frac{n_A^s}{V_{int}}\\
\frac{\mathrm{d}}{\mathrm{d}t}n_D^g &= \dot{F}_{in}\cdot C_D^{in} - \dot{F}_{out}\cdot\frac{n_D^g}{V} - h_{m,D}\cdot A\cdot\left(\frac{n_D^g}{V}-\frac{n_D^s}{V_{int}}\right)\\
\frac{\mathrm{d}}{\mathrm{d}t}n_D^s &= A\cdot h_{m,D}\cdot\left(\frac{n_D^g}{V}-\frac{n_D^s}{V_{int}}\right) + A\cdot k_2\cdot\frac{n_B^s}{V_{int}} + A\cdot k_3\cdot\frac{n_A^s}{V_{int}}
\end{aligned}
\tag{4.46}
$$

where component j is described by its inlet feed concentration, $C_j^{in}\,[\mathrm{mol}\cdot\mathrm{m}^{-3}]$, its amount of substance in the gas phase, $n_j^g\,[\mathrm{mol}]$, and its amount of substance in the solid phase on top of the substrate, $n_j^s\,[\mathrm{mol}]$; $t\,[\mathrm{s}]$ is the reaction time; $\dot{F}_{in}\,[\mathrm{m}^3\cdot\mathrm{s}^{-1}]$ and $\dot{F}_{out}\,[\mathrm{m}^3\cdot\mathrm{s}^{-1}]$ are, respectively, the inlet and outlet volumetric flow rates of the carrier gas; $h_{m,j}\,[\mathrm{m}\cdot\mathrm{s}^{-1}]$ is the gas to solid phase mass transfer coefficient of component j; $V\,[\mathrm{m}^3]$ is the gas phase reaction volume; $V_{int}\,[\mathrm{m}^3]$ is the solid-gas interface volume; and $A\,[m^2]$ is the glass surface area in contact with the gas. Note that $\dot{F}_{in} = \dot{F}_{out} = Q$ when there is no accumulation, where $Q\,[\mathrm{m}^3\cdot\mathrm{s}^{-1}]$ is the carrier gas flow rate from Equation 4.3. The reaction rate constants and the mass transfer coefficients are not known exactly and are then represented using probability distributions. Therefore, the solution of the ODE system will then return a distribution, which is used to predict the most likely values of the final amounts of each material.

The driving force for the diffusion of particles from the bulk gas to the solid interface is the difference in concentration of the particles in the two regions. The model presented in Equation 4.46 used the solid-gas interface volume $V_{int}\,[\mathrm{m}^3]$, which can be physically interpreted as the volume of the static boundary layer from fluid dynamics. This way of modelling explicitly shows the use of the boundary layer. However, it is more common to find in the literature models that will leave the boundary layer implicit [46, 157–159], by writing the driving force $\left(\frac{n_i^g}{V}-\frac{n_i^s}{V_{int}}\right)$ as $(C_i^g - C_i^s)$. Nevertheless, the results are equivalent.

For the industrial-scale deposition on a continuously flowing glass, the process

operates at steady state. When comparing the batch with the continuous process, the time derivatives in Equation 4.46 become dependent on space and time, given that the carrier gas flows inside the distributor beam and on top of the moving glass, where the film grows, as shown in the bottom right-hand side of Figure 2.1. Since the interest lies in the profile of film growth as the glass moves, the reaction space was discretised into small parallelograms and solved Equation 4.46 for each one of them. The flow rate of carrier gas and the speed of the flowing glass dictate the residence time of the precursors in each discretised parallelogram. The result is the film growth profile as the glass flows through the deposition zone. The final amount of deposited D, $n_D^s\,[\mathrm{mol}]$, and the film thickness, $\tau\,[\mathrm{m}]$, will be given by:

$$\begin{aligned} n_D^s &= \rho_d \cdot \int_{d_d} \int_t f\left(\mathbf{x}\right) \cdot \mathrm{d}t \cdot \mathrm{d}d_d \\ \tau &= \frac{n_D^s}{\overline{\rho} \cdot w \cdot v \cdot t_r} \end{aligned} \tag{4.47}$$

where $f\left(\mathbf{x}\right)$ represents the integrated models for aerosol generation, transport and delivery and chemical deposition described above; $\rho_d\,[\mathrm{kg \cdot m^{-3}}]$ is the density of the precursor solution; $d_d\,[\mathrm{m}]$ is the droplet diameter; $t\,[\mathrm{s}]$ is time; $\overline{\rho}\,[\mathrm{mol \cdot m^{-3}}]$ is the mean molar density of the film; $w\,[\mathrm{m}]$ is the glass width; $v\,[\mathrm{m \cdot s^{-1}}]$ is the speed of the flowing glass; and $t_r\,[\mathrm{s}]$ is the chemical deposition residence time, defined as the time taken by the glass to cross the distributor beam. Note that the glass surface area in contact with the gas, $A\,[\mathrm{m^2}]$, is given by the product $w \cdot v \cdot t_r$.

A general chemical vapour deposition mechanism was introduced to illustrate the modelling procedure. Equation 4.46 was derived from mass balances of the given mechanism. Equation 4.47 is an original contribution of this work. It represents the final objective of the integrated model, which is to obtain the film thickness as a function of all the preceding and integrated steps of the AACVD process: the aerosol generation, transport, delivery and the chemical deposition. To apply the model for the production of a specific film, suffices to adapt Equation 4.46.

4.7 Summary

A procedure for a model-based scale-up for the AACVD process was introduced. With that in mind, models were presented to simulate every step needed for an industrial-scale AACVD. This includes models to predict the droplet median diameter generated by ultrasonic vibration; models to predict the amount and distribution of the droplet sizes for the aerosol that successfully crosses a piping transport

system; models to predict the increase in temperature when the carrier gas is heated and the time taken for the solvent to evaporate and release the precursors; and models to predict the growth rate and thickness of the deposited films. Next, simulation results for these models and their experimental validation will be presented.

5 Process Simulations and Experimental Validation

The models previously presented are now applied to exemplify how different parameters impact the aerosol droplet size and how they can be studied and understood. This includes the log-normal distribution of the aerosol droplet size generated by ultrasonic vibration, using a piezoelectric transducer. The loss of aerosol throughout a transport system and the final size distribution at the outlet of the piping system are also studied.

Potter et al. [31] used aerosol-assisted chemical vapour deposition (AACVD) to deposit thin transparent conducting oxide films on glass substrates. The generated aerosol retains the properties of the solvent used, assuming that the solute quantity is small enough. Carrier fluids are usually air or nitrogen; the latter if an inert atmosphere is necessary in the reactor. Therefore, to further evaluate the models proposed, simulations will be run using methanol as the solvent, which is atomised and transported using nitrogen as the carrier fluid at constant flow rate and room temperature.

5.1 Aerosol Generation

Based on Equation 4.2, the median droplet diameter is a function of some parameters that depend on the equipment and others that depend on the physico-chemical properties of the fluid to be atomised and its flow rate. The available commercial atomisers, such as the Sono-Tek Ultrasonic Nozzle, work with frequencies ranging from kilohertz to megahertz [160]. Figure 5.1 shows how the median droplet diameter changes with the frequency of the atomiser, according to the model presented in Section 4.3. The nominal values of the parameters used as the model input, based on the atomisation of methanol at 298.15 K, are listed in Table 5.1.

Using the same values displayed in Table 5.1, for a transducer frequency of 1.60 MHz, Figure 5.2 is obtained, presenting how the droplet median diameter is

Table 5.1: Input parameters for methanol atomisation.

Symbol	Parameter	Nominal Value	Units
ρ_d	Atomiser fluid density	786.6	$\mathrm{kg \cdot m^{-3}}$
σ_d	Atomiser fluid surface tension	$2.2 \cdot 10^{-2}$	$\mathrm{N \cdot m^{-1}}$
Symbol	Design Variable	Range	Units
f	Ultrasonic atomiser frequency	$[0.5, 20] \cdot 10^5$	Hz

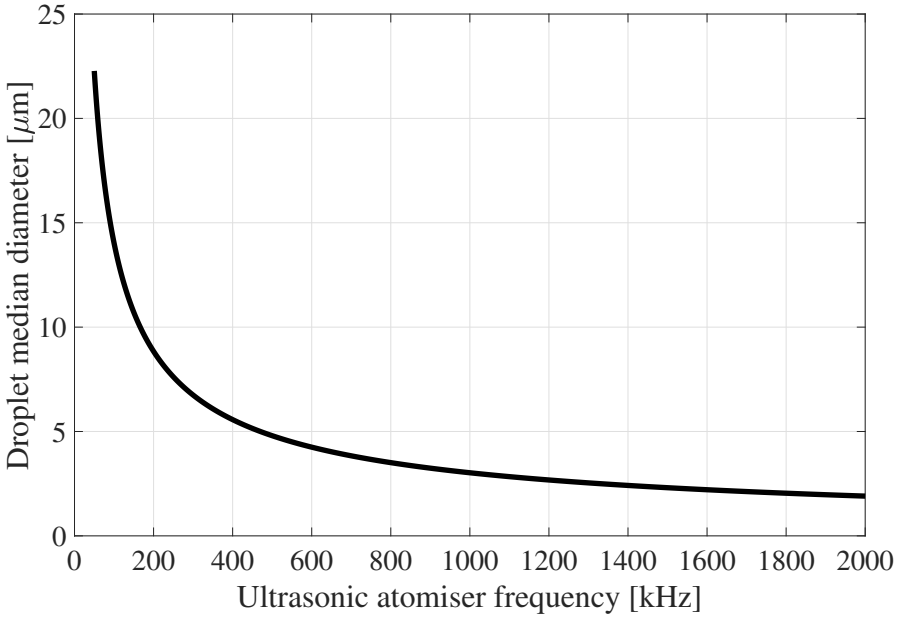

Figure 5.1: Median droplet diameter as a function of atomiser frequency. Other parameters as listed in Table 5.1.

sensitive to changes in different parameters. atomiser ultrasonic frequency of vibration is shown to have the greatest impact for the operating setting used. If it were to be increased by 5% (from 1.60 MHzto 1.68 MHz), the droplet median size would decrease by 3.2% (from 2.21 to 2.14 μm).

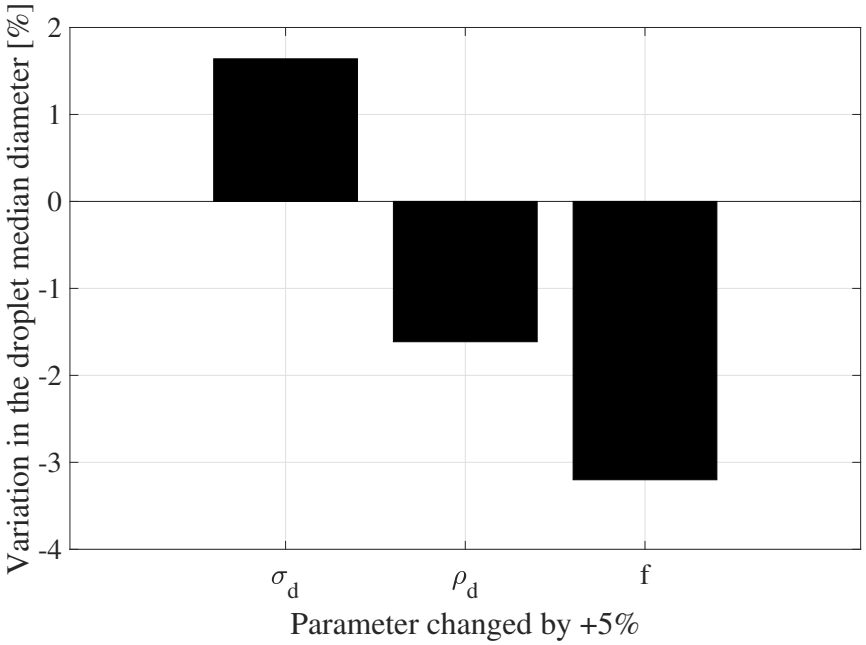

Figure 5.2: Local sensitivity analysis for the droplet median diameter. Each parameter is increased by 5%, keeping the other parameters constant. The percentage effect in the median diameter is shown in the y-axis. Other parameters as listed in Table 5.1.

Finally, Figure 5.3 shows the median droplet size as a function of the atomiser ultrasonic frequency and fluid density, the two parameters inversely proportional to the droplet diameter, for a constant fluid surface tension of $\sigma_d = 2.2 \cdot 10^{-2}\,\mathrm{N \cdot m^{-1}}$.

5.2 Aerosol Transport

Applying the equations described in Section 4.4, it is possible to study the aerosol penetration for different scenarios. First, straight pipes will be treated, followed by bends and coiled pipes. Finally, the droplet size distributions are shown for the inlet and outlet of different piping systems.

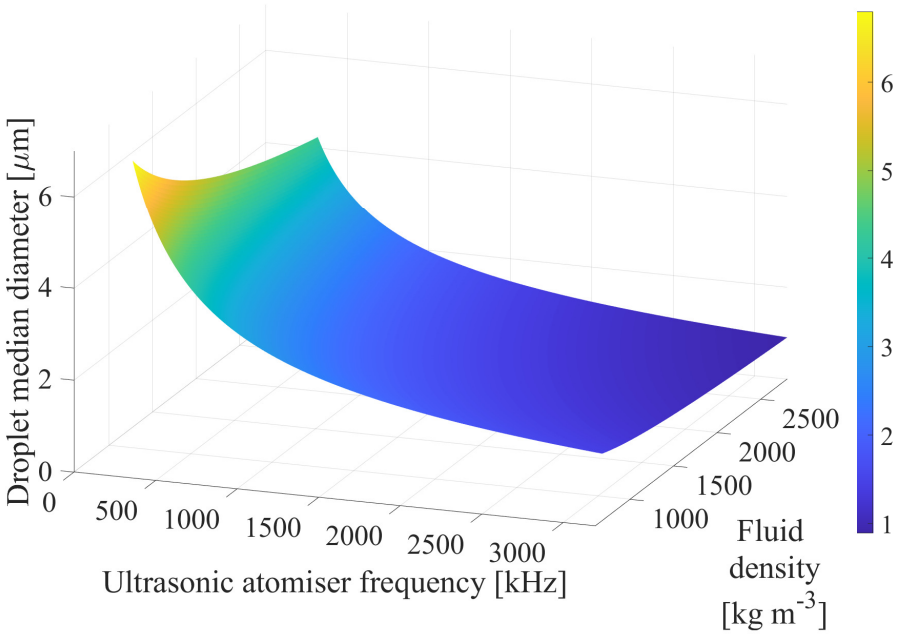

Figure 5.3: Median droplet diameter as a function of atomiser frequency and fluid density for fluid surface tension of $\sigma_d = 2.2 \cdot 10^{-2}\,\mathrm{N \cdot m^{-1}}$. The droplet diameter is shown in the z-axis and in the colour bar. Fixed model parameters are listed in

5.2.1 Straight Pipes

Different straight pipe settings are now simulated to understand the impacts of different deposition mechanisms. The nominal values of the model input parameters are presented in Table 5.2. Whenever a parameter is changed, it will be mentioned.

Table 5.2: Input parameters for the transport of methanol aerosol through straight pipes.

Symbol	Parameter	Nominal Value	Units
ρ	Carrier fluid density	1.17	$\mathrm{kg \cdot m^{-3}}$
Q	Carrier fluid flow rate	$3.333 \cdot 10^{-5}$	$\mathrm{m^3 \cdot s^{-1}}$
μ	Carrier fluid dynamic viscosity	$1.85 \cdot 10^{-5}$	$\mathrm{N \cdot s \cdot m^{-2}}$
ρ_d	Droplet density	786.6	$\mathrm{kg \cdot m^{-3}}$
d_d	Droplet diameter	$7 \cdot 10^{-6}$	m
d	Pipe inner diameter	0.01	m
ϕ	Pipe inclination angle (reference: horizontal axis)	30	degrees
L	Pipe length	2	m

5.2.1.1 Sensitivity Analysis

Figure 5.4 shows the sensitivity analysis for the initial input vector using all parameters as described in Table 5.2. The droplet diameter is shown to have the greatest impact for the input vector used: if it were to be increased by 5% (from 7.00 to 7.35 μm), the fraction of aerosol penetration would be reduced by 6% (from 0.54 to 0.51).

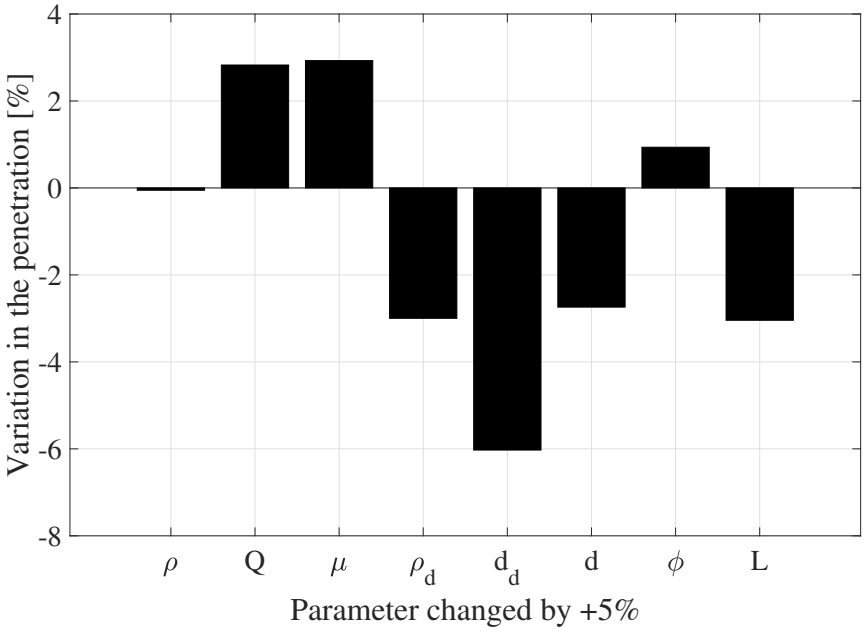

Figure 5.4: Sensitivity analysis for the aerosol penetration. Each parameter is increased by 5%, keeping the other parameters constant. The percentage effect in the aerosol penetration is shown in the y- axis. Other parameters as listed in Table 5.2.

5.2.1.2 The Contribution of Different Mechanisms

Figure 5.5 shows the dominance of each particular mechanism on the aerosol deposition depending on the droplet diameter for both horizontal and vertical pipes. For the horizontal pipe, a trade-off can be seen related to the size of transported particles: gravitational settling has little impact towards little droplets; however, they are more impacted by Brownian diffusion. The reverse can be seen for bigger droplets, which are strongly affected by gravitational settling. It can also be seen that the turbulent diffusion mechanism has little impact for horizontal pipe. This impact grows as the pipe inclination angle increases and is maximum when the pipe becomes vertical, when the gravitational settling becomes negligible.

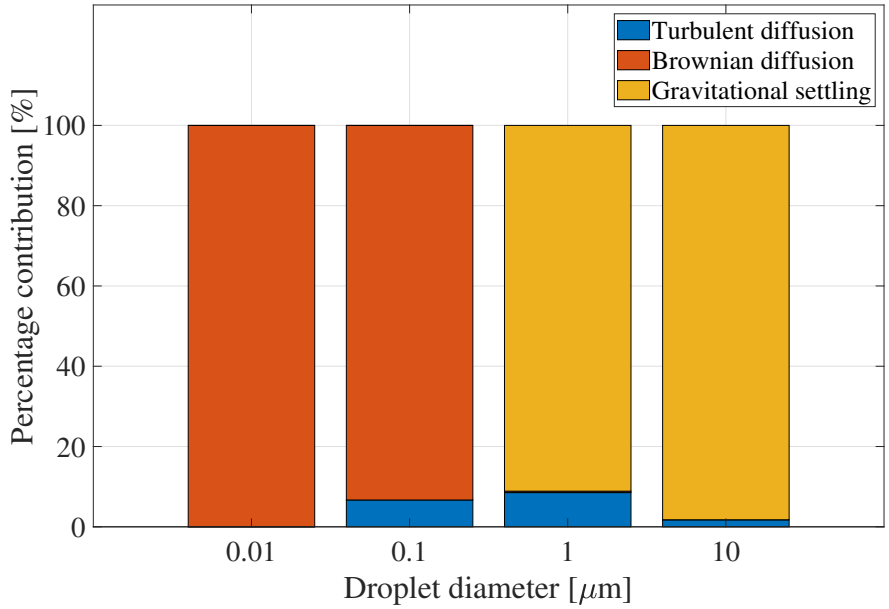

(a) Horizontal pipe.

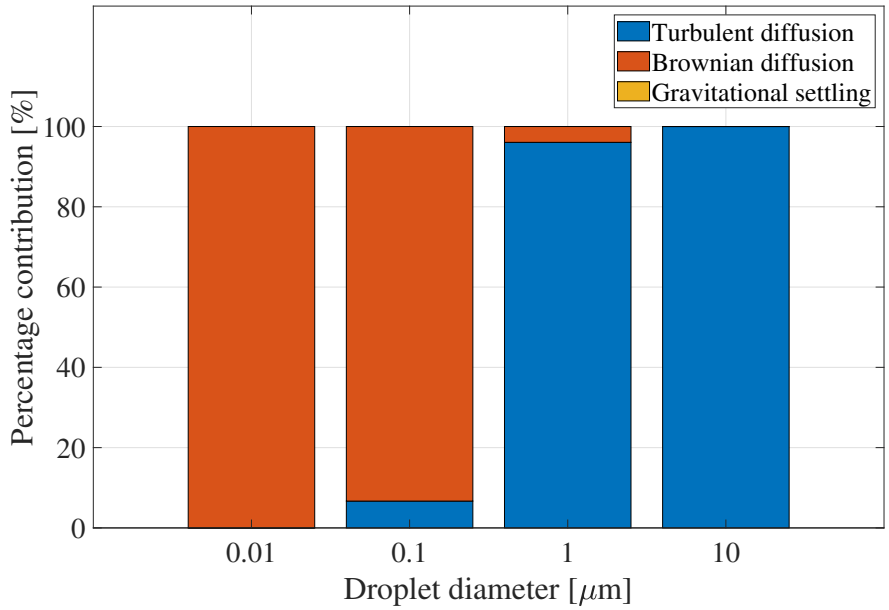

(b) Vertical pipe.

Figure 5.5: Percentage contribution of different mechanisms to the overall aerosol deposition, for different droplet sizes and horizontal or vertical pipe. Other parameters as listed in Table 5.2.

Figure 5.6 shows the dominance of each particular mechanism on the aerosol deposition depending on the pipe diameter. The figure only shows a horizontal pipe, since the only contribution for a vertical pipe would be turbulent diffusion, given that Brownian diffusion is negligible for the droplet diameter used, $d_d = 7\,\mu$m. It can be seen that small tube diameters have lower gravitational settling, but higher turbulent deposition. The reverse occurs for larger tube diameters.

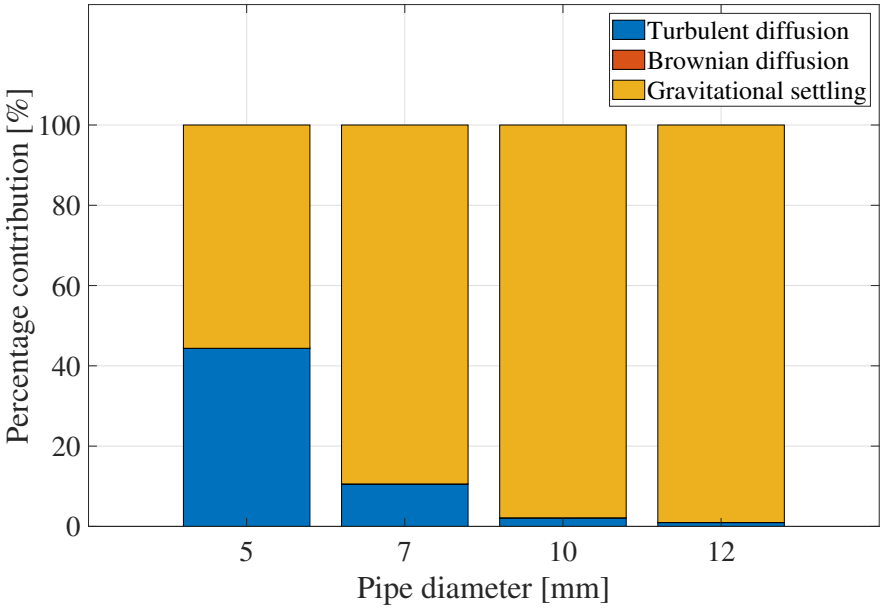

Figure 5.6: Percentage contribution of different mechanisms to the overall aerosol deposition, for different horizontal pipe diameters. Other parameters as listed in Table 5.2

5.2.1.3 The Impact of Droplet Size on Aerosol Penetration

Figure 5.7 shows the variation of the aerosol penetration as a function of the droplet size. The logarithmic scale was used so that a wide range of droplet diameters could be represented. It is interesting to note that substantial droplet losses occur in both extremes of the droplet sizes, too small and too big. The area with greater aerosol penetration coincides with the transition between the dominant Brownian diffusion mechanism for small droplets and the gravitational settling for bigger and heavier droplets.

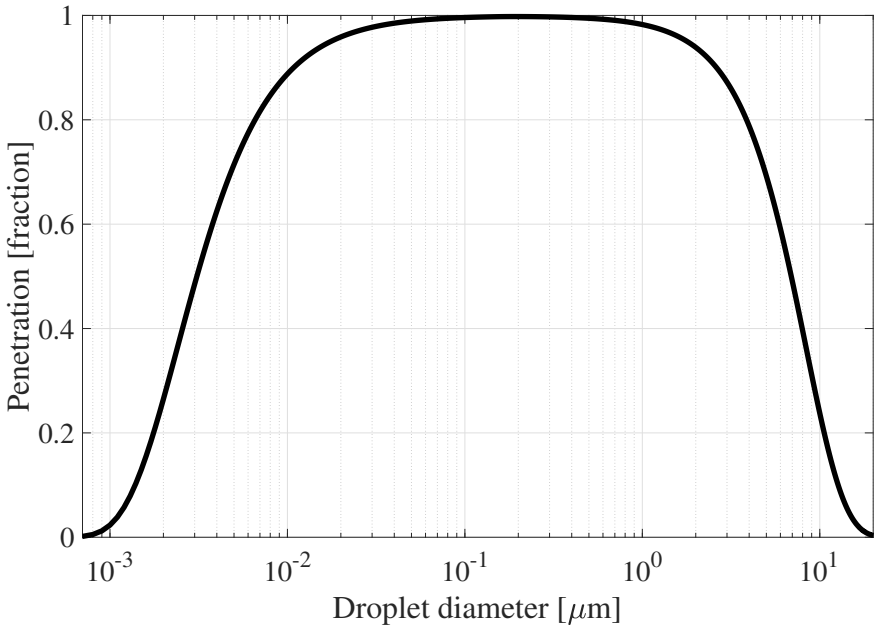

Figure 5.7: Penetration as a function of droplet diameter. Other parameters as listed in Table 5.2.

5.2.1.4 Aerosol Penetration as a Function of Pipe Length and Inclination Angle

Figure 5.8 shows the variation of the aerosol penetration with the pipe length, for different pipe inclinations. Notice how the penetration decreases at a growing rate as the vertical pipe is inclined until reaching the horizontal position. This is explained by the growing impact of the gravitational settling mechanism, which is maximum for the horizontal pipe and negligible for the vertical one. Figure 5.9 clearly exemplifies how the aerosol penetration decreases faster with the growth of pipe length for inclination angles approaching zero, which is the horizontal position.

5.2.2 Bends

Applying the model described in Section 4.4.2, it is possible to study the aerosol penetration for pipe bends. Figure 5.10 shows the sensitivity analysis for the nominal values of the parameters used as the model input described in Table 5.3. The tube inner diameter is shown to have the greatest impact for the input vector used: if it were to be increased by 5% (from 0.0100 to 0.0105 m), the fraction of aerosol penetration would be increased by 0.16% (from 0.989 to 0.991). On the other hand, the impact of temperature change is negligible. For a single bend, the aerosol loss

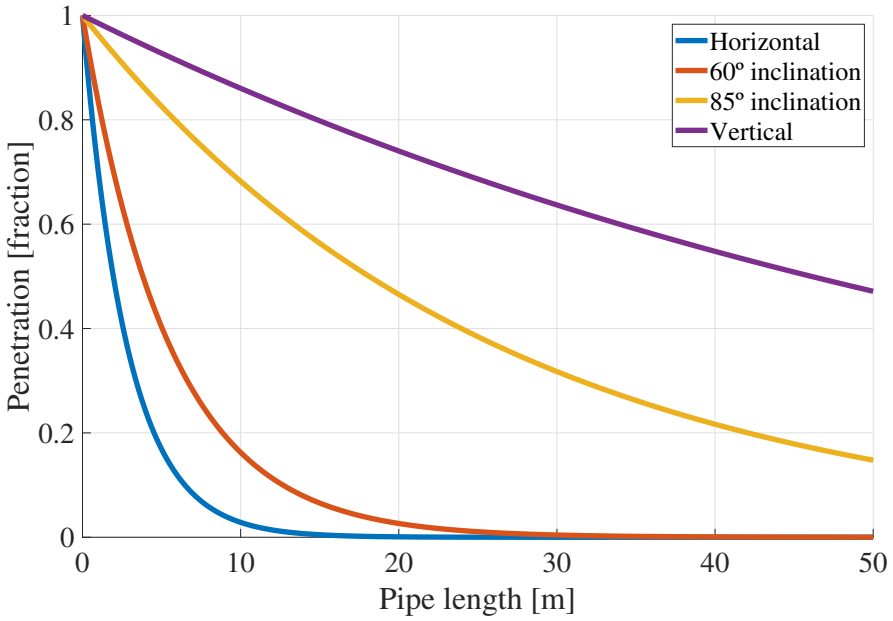

Figure 5.8: Penetration as a function of pipe length for different inclinations. Other parameters as listed in Table 5.2.

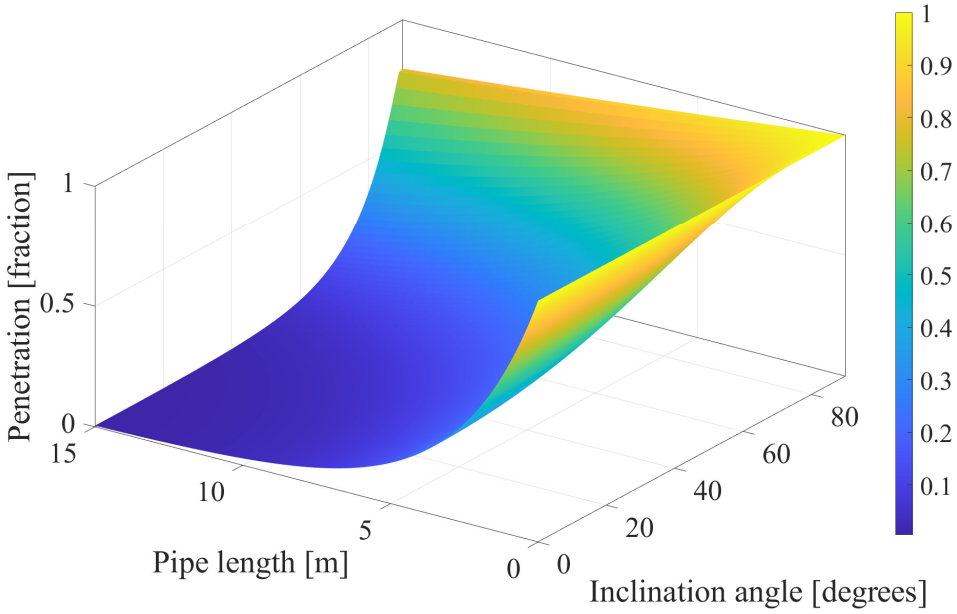

Figure 5.9: Aerosol penetration as a function of pipe length and inclination angle. The penetration fraction is shown in the z-axis and in the colour bar. Fixed model parameters are listed in Table 5.2.

is seen to be very small.

Table 5.3: Input parameters for the transport of methanol aerosol through pipe bends.

Symbol	Parameter	Nominal Value	Units
T	Temperature	298.15	K
Q	Carrier fluid flow rate	$3.333 \cdot 10^{-5}$	$m^3 \cdot s^{-1}$
μ	Carrier fluid dynamic viscosity	$1.85 \cdot 10^{-5}$	$N \cdot s \cdot m^{-2}$
ρ_d	Droplet density	786.6	$kg \cdot m^{-3}$
d_d	Droplet diameter	$7 \cdot 10^{-6}$	m
r_b	Bend radius	0.1	m
α	Bend angle	90	degrees
d	Tube inner diameter	0.01	m

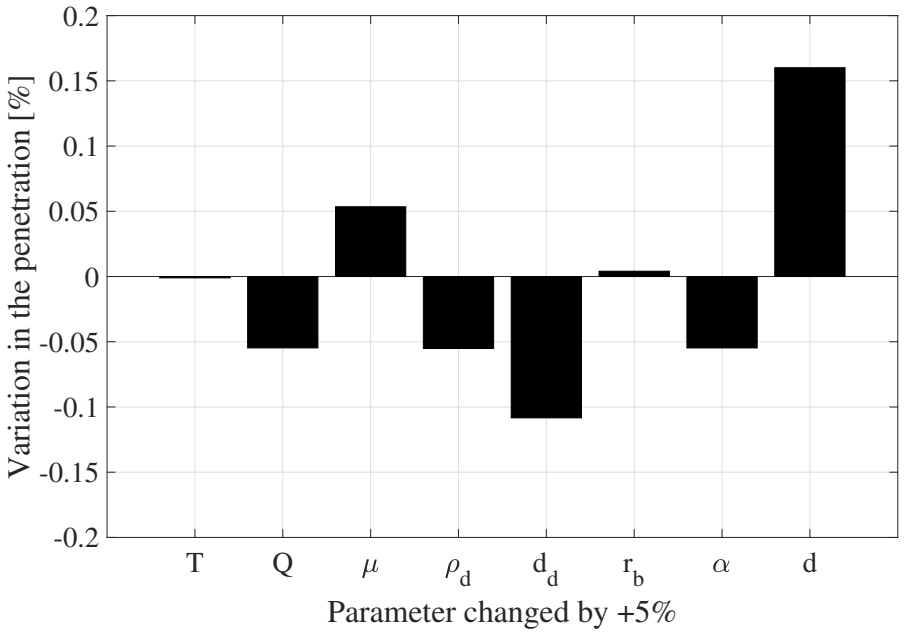

Figure 5.10: Sensitivity analysis for the aerosol penetration on a bend. Each parameter is increased by 5%, keeping the other parameters constant. The percentage effect in the penetration fraction is shown in the y-axis. Other parameters as listed in Table 5.3.

5.2.3 Droplet Diameter Distribution before and after a Transport System

The median droplet diameter obtained when generating aerosol by ultrasonic vibration is modelled using a log-normal distribution, where the variance of the distribution is a function of the atomiser properties. The loss of aerosol throughout the piping system changes dramatically depending on the size of the droplets, which makes it the variable of greatest interest. Therefore, the inlet droplet size distribution can be used to predict the outlet droplet distribution, as will be shown next.

Figure 5.11 shows the inlet droplet sizes following a log-normal distribution, represented by the blue curve. The red curve represents the outlet fraction of aerosol that is expected to successfully cross the transport system, in this case it is 0.63. The system is described by the parameters from Table 5.2, except the pipe length and position, which are respectively 1 m and horizontal. Additionally, Figure 5.12 shows the results when a 5 m horizontal pipe is used. The fraction of aerosol crossing the pipe is expected to be 0.26. The area under the curves represents the penetration fraction of aerosol.

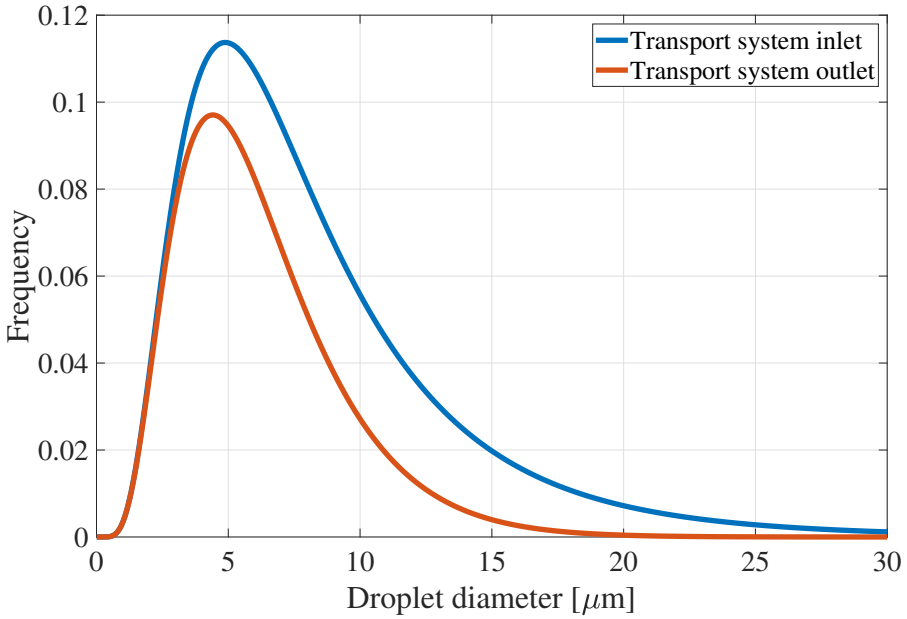

Figure 5.11: Droplet diameter distribution before and after transport in a horizontal pipe of 1 m length. Area under inlet curve is unitary and under the outlet curve is the fraction of aerosol expected in the outlet of the coiled pipe. Other parameters as listed in Table 5.2.

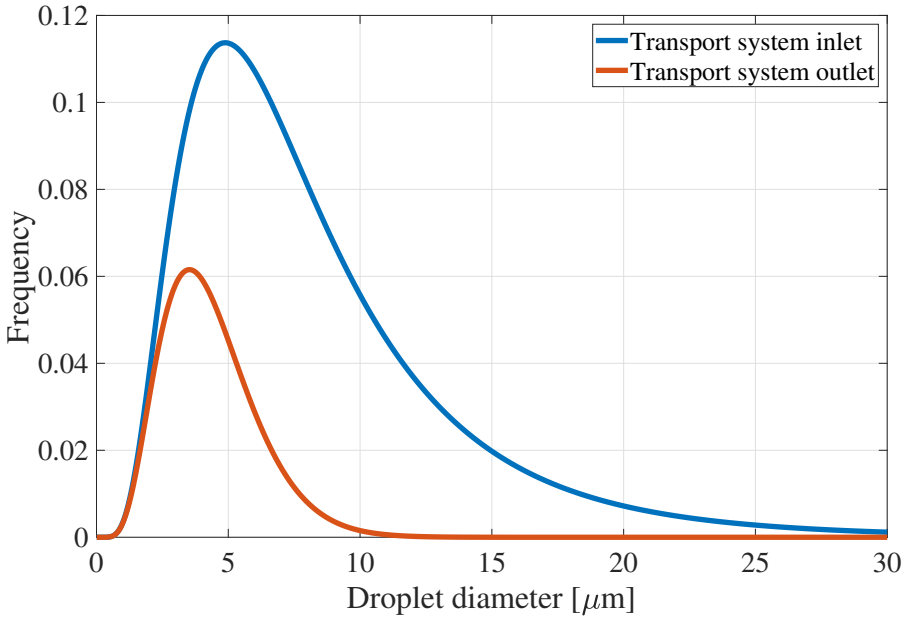

Figure 5.12: Droplet diameter distribution before and after transport in a horizontal pipe of 5 m length. Area under inlet curve is unitary and under the outlet curve is the fraction of aerosol expected in the outlet of the coiled pipe. Other parameters as listed in Table 5.2.

5.3 Experimental Validation

The aerosol generation and transport models presented in Sections 4.3 and 4.4 had already been validated using experimental data available in the literature. Further validation was possible through preliminary experiments performed at the Materials Chemistry Centre, part of University College London's Department of Chemistry. A laboratory-scale atomiser and transport system were used to emulate the generation and transport of aerosol. The following subsections present the methodology and the results.

5.3.1 Experimental Setting and Data Collected

An ultrasonic atomiser manufactured by Johnson Matthey Piezo Products was used to generate aerosol from liquid methanol. The aerosol was then transported through different pipe lengths using nitrogen as the carrier gas. Due to space restrictions in the laboratory and as a good approximation of a worst-case scenario, the transport tubing for these experiments was arranged in a coil format. The nitrogen carrier gas flow rate was $1\,\mathrm{L}\cdot\mathrm{min}^{-1}$, the temperature during the experiments was

approximately 25°C, and the atomiser should operate at a frequency of approximately 1.6 MHz, as provided by Johnson Matthey's technical data [161].

The measurement of the aerosol loss during transport was made using the experimental setting shown in Figure 5.13. The atomiser was fed 20 mL of liquid methanol to generate aerosol, which was carried by nitrogen gas from the atomiser through the coiled transport system to a cold-trap, which let the carrier gas pass while trapping the aerosol. The experiment ended when all the methanol had been atomised and transported. The mass difference between the cold-trap before and after the experiment is the amount of aerosol that successfully travelled through the coiled pipe. The amount of aerosol lost during transport is the mass difference between the initial liquid methanol and what was caught in the cold-trap. Each experiment was repeated three times to ensure the reproducibility of the results. The measurements were made for 2, 8 and 50 m of coiled pipe, with the results shown in Table 5.4.

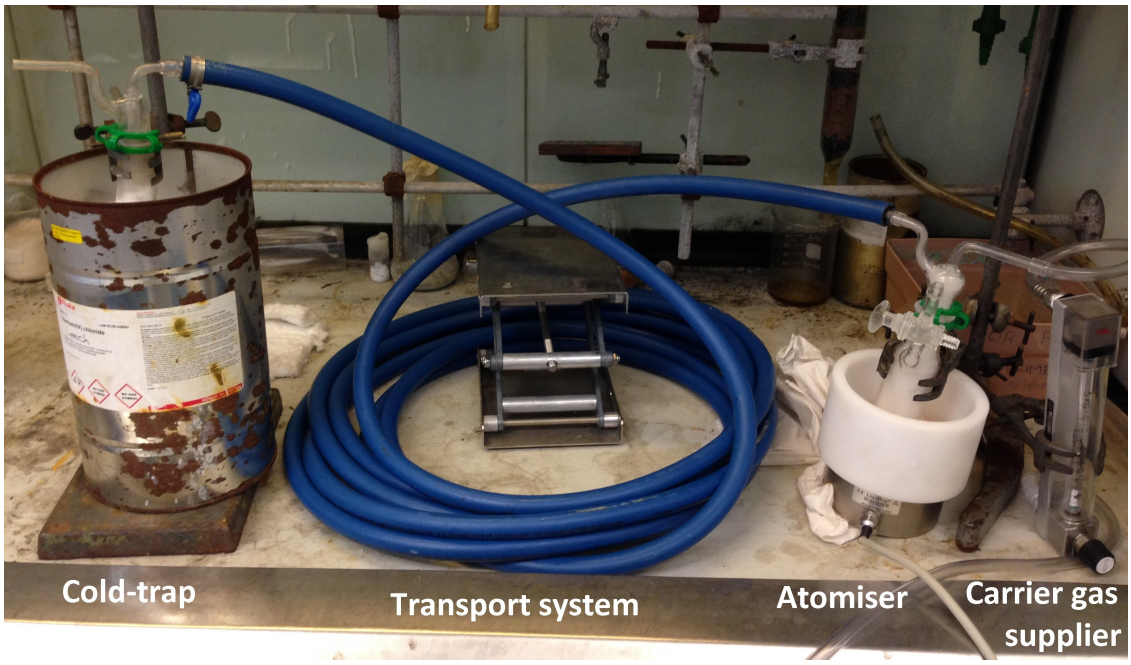

Figure 5.13: Experimental setting made of an atomiser in between a coiled tubing system and a supplier of carrier gas.

The measurement of the aerosol droplet size distributions was made using a similar experimental setting, but replacing the cold-trap with a Malvern Instruments' Spraytec laser diffraction device, responsible for sizing the aerosol. The measurements were made at four different points: the first one was where the aerosol leaves the atomiser; then after 2, 4 and 8 m of coiled pipe. The results are shown, respectively, in Figures 5.14, 5.15, 5.16 and 5.17. The measuring error was considerably lower for the outputs of the coiled pipes than for the output of the atomiser. This

was possibly caused by a less organised atomiser output, when compared to the coiled pipe output. The error bars shown in the preceding figures were generated for each run, which is independent from each other, they represent instrumental error and not the experimental spread of values.

Table 5.4: Fraction of aerosol particles that successfully crossed a given length of a coiled pipe transport system.

Transport system length $[m]$	Aerosol penetration
2	0.48 ± 0.03
8	0.18 ± 0.03
50	0.05 ± 0.03

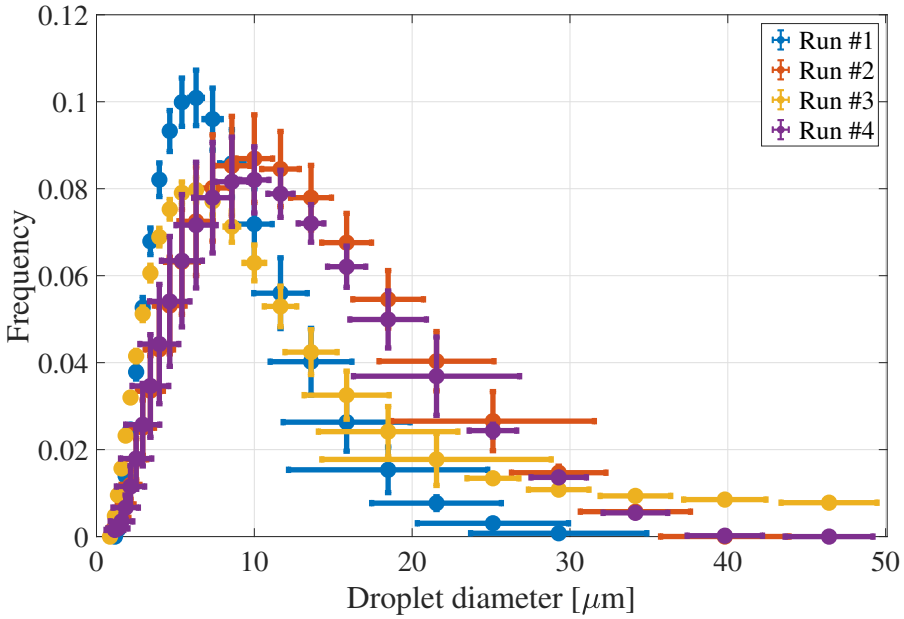

Figure 5.14: Experimental droplet size distribution after methanol atomisation.

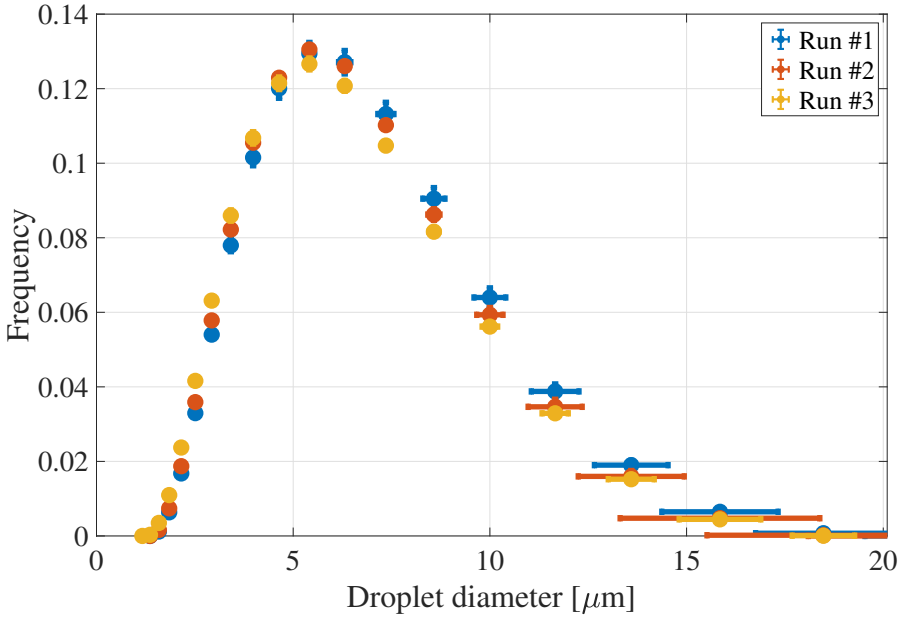

Figure 5.15: Experimental droplet size distribution after 2 m coiled pipe.

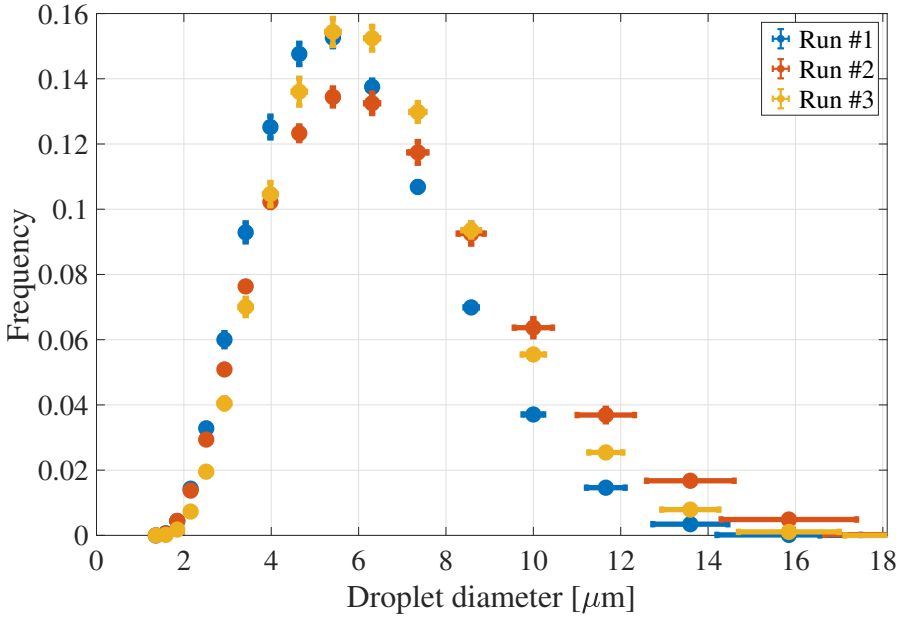

Figure 5.16: Experimental droplet size distribution after 4 m coiled pipe.

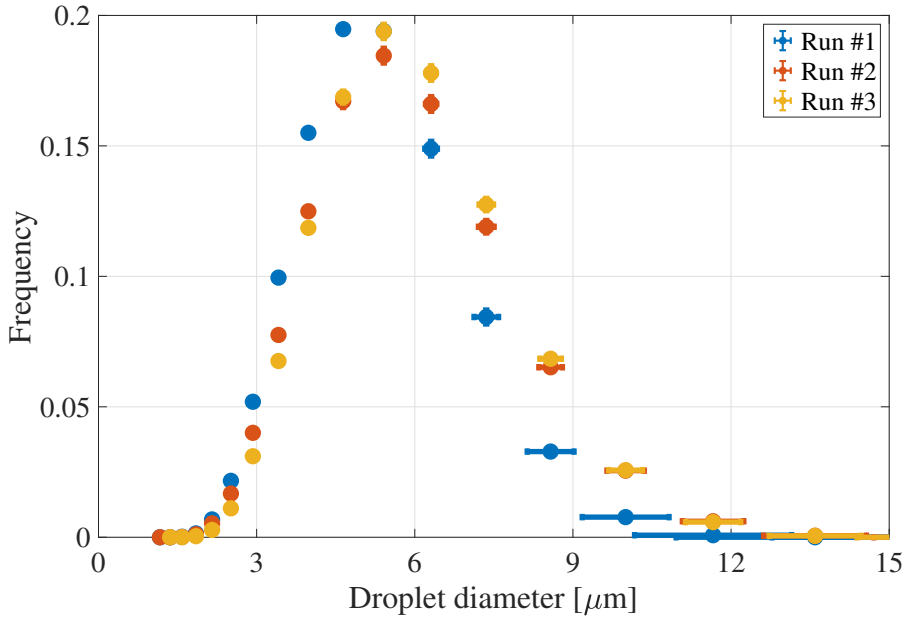

Figure 5.17: Experimental droplet size distribution after 8 m coiled pipe.

5.3.2 Comparison between Model and Experimental Results

The aerosol generation model presented in Section 4.3 can be directly applied using the experimental conditions to predict the size distribution of the aerosol produced. Liquid methanol was atomised at 25°C, therefore, the model input is: surface tension $\sigma_d = 0.022\,\mathrm{N \cdot m^{-1}}$, density $\rho_d = 786.6\,\mathrm{kg \cdot m^{-3}}$ and atomiser frequency $f = 1.6\,\mathrm{MHz}$. The result is shown in Figure 5.18(a), which presents a large discrepancy between the predicted distribution and the experimental distribution. This discrepancy motivated a further look into the atomiser's technical data provided by its manufacturer [161]. In fact, the technical data claims that the atomiser operates at a frequency of approximately 1.6 MHz and generates aerosol with median droplet size of approximately 3 μm. This is perfectly consistent with, and matches exactly, the output of the aerosol generation model for water (model input: $\rho_d = 997\,\mathrm{kg \cdot m^{-3}}$, $\sigma_d = 0.072\,\mathrm{N \cdot m^{-1}}$, $f = 1.6\,\mathrm{MHz}$), which validates the model. However, the expected median droplet size for methanol would be 2.2 μm (model input: $\sigma_d = 0.022\,\mathrm{N \cdot m^{-1}}$, $\rho_d = 786.6\,\mathrm{kg \cdot m^{-3}}$, $f = 1.6\,\mathrm{MHz}$), as shown in Figure 5.18(a), which differs from the measured droplet sizes obtained from the experiment. This suggests that the atomiser was malfunctioning and generating much larger droplets, as if the operating frequency were 100 kHz instead of 1.6 MHz. The model results for the lower frequency are shown in 5.18(b), the predicted median droplet size is 14 μm (model input: $\sigma_d = 0.022\,\mathrm{N \cdot m^{-1}}$, $\rho_d = 786.6\,\mathrm{kg \cdot m^{-3}}$, $f = 100\,\mathrm{kHz}$).

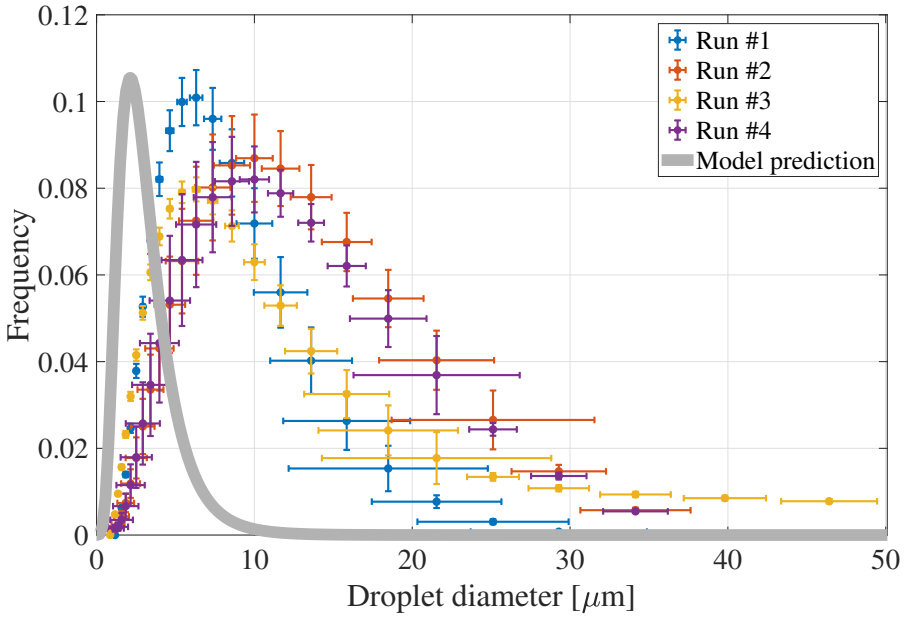

(a)

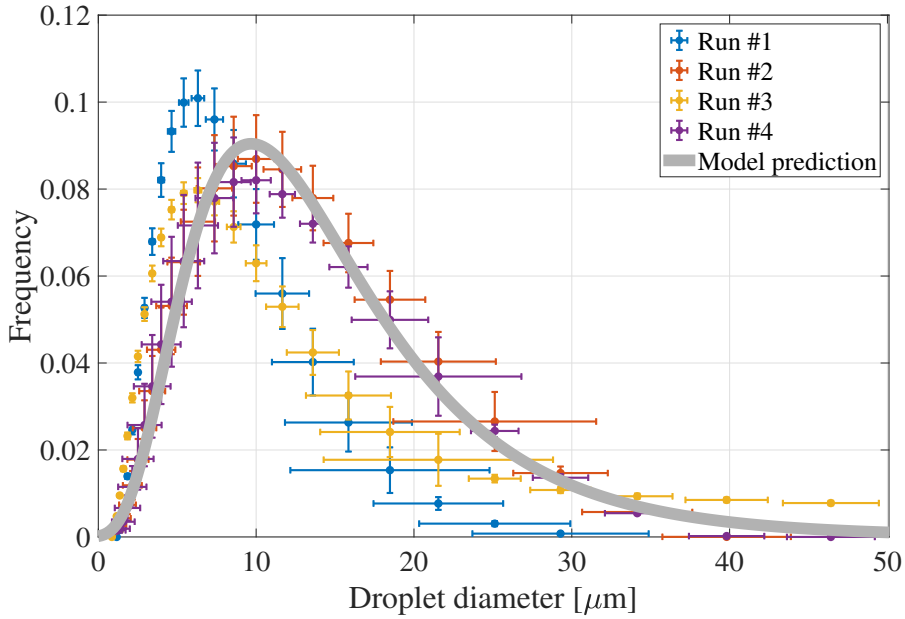

(b)

Figure 5.18: Comparison between the predicted and the experimentally obtained droplet size distributions for the droplets generated by the atomiser. The experimental data was used for the validation of the aerosol generation model. The model input for (a) and (b) used surface tension $\sigma_d = 0.022\,\mathrm{N \cdot m^{-1}}$ and density $\rho_d = 786.6\,\mathrm{kg \cdot m^{-3}}$. However, (a) used atomiser frequency $f = 1.6\,\mathrm{MHz}$, while (b) used atomiser frequency $f = 100\,\mathrm{kHz}$. The *log*-normal distribution for aerosol sizing is described in Section 4.3.

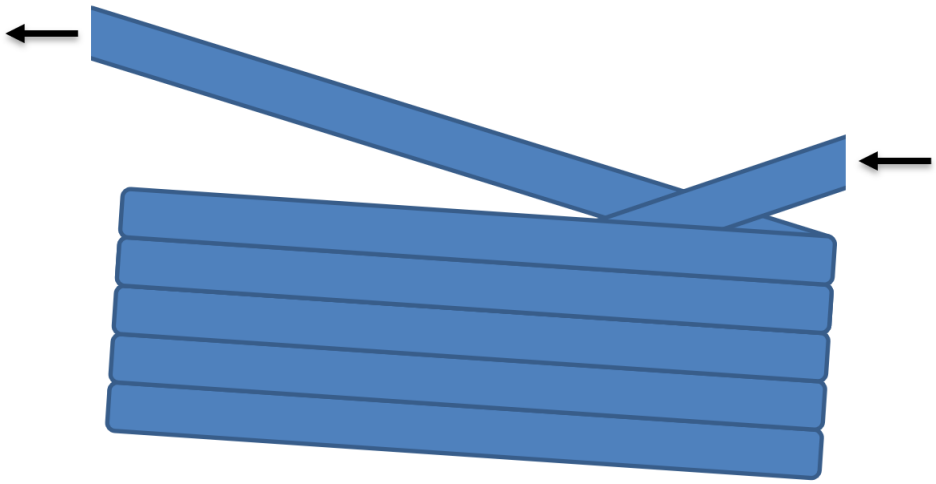

Figure 5.19: Schematics of a coiled pipe setting.

To validate the aerosol transport model presented in Section 4.4.3, the experimental conditions shown in Table 5.5 and the droplet distribution shown in grey in Figure 5.18(b) are used as the model input to run the simulations. The model predictions are then compared with the experimental results. Table 5.6 shows the comparison for the fraction of aerosol that successfully crosses the transport system. Figures 5.20, 5.21 and 5.22 show the comparisons of the size distributions for the 2, 4 and 8 m coiled pipe system, respectively.

The fact that the aerosol is transported at room temperature for the AACVD process allowed the assumption that aerosol evaporation during transport is negligible. However, it is likely that the evaporation of droplets should be considered in case of transport at higher temperatures or if very volatile solvents are used.

Table 5.5: Experimental conditions used as input parameters for the transport of methanol aerosol through the coiled pipe system.

Symbol	Parameter	Nominal Value	Units
ρ	Nitrogen gas density	1.17	$\mathrm{kg \cdot m^{-3}}$
Q	Nitrogen gas flow rate	1	$\mathrm{L \cdot min^{-1}}$
μ	Nitrogen gas dynamic viscosity	$1.85 \cdot 10^{-5}$	$\mathrm{N \cdot s \cdot m^{-2}}$
ρ_d	Droplet density	786.6	$\mathrm{kg \cdot m^{-3}}$
d	Coiled pipe inner diameter	1	cm
r_c	Coil radius	10	cm
l	Coiled pipe length	$2, 4, 8, 50$	m
T	Temperature	25	°C

Table 5.6: Comparison between experiment and model fraction of aerosol particles that successfully crossed a given length of a coiled pipe transport system.

Transport system length $[m]$	Experimental aerosol penetration	Model predicted aerosol penetration
2	0.48 ± 0.03	0.48
8	0.18 ± 0.03	0.17
50	0.05 ± 0.03	0.03

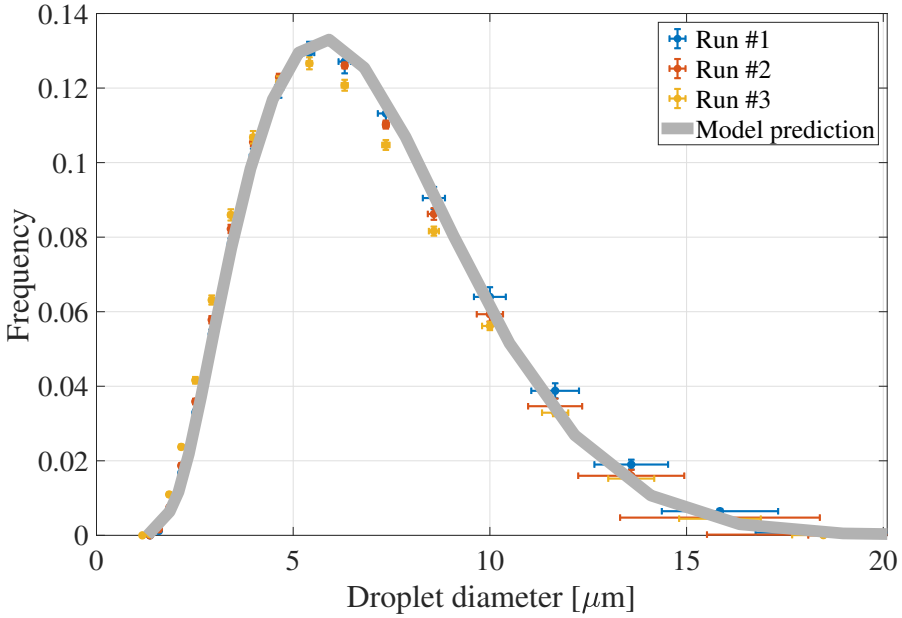

Figure 5.20: Comparison between the model prediction and the experimentally obtained droplet size distribution for a 2 m coiled transport system for the validation of the aerosol transport model. Model parameters as listed in Table 5.5.

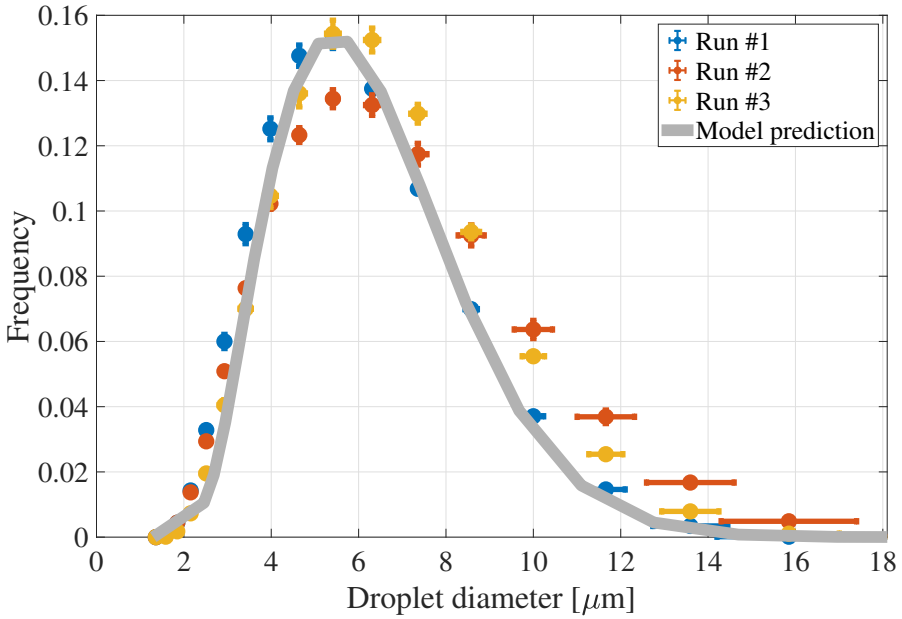

Figure 5.21: Comparison between the model prediction and the experimentally obtained droplet size distribution for a 4 m coiled transport system for the validation of the aerosol transport model. Model parameters as listed in Table 5.5.

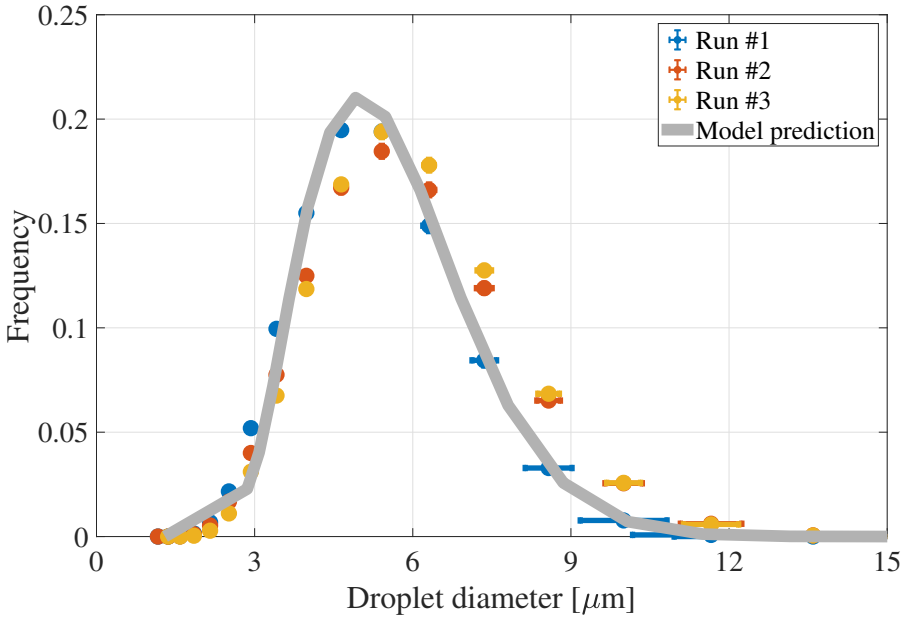

Figure 5.22: Comparison between the model prediction and the experimentally obtained droplet size distribution for a 8 m coiled transport system for the validation of the aerosol transport model. Model parameters as listed in Table 5.5.

5.4 Summary

The AACVD models presented in Chapter 4 were evaluated under different conditions to exemplify the use of the models and to show how the variation of parameter values affect the final results. Although the examples given used a specific set of parameter values, the same methodology could be applied for any design choices and the whole AACVD model or for specific parts, for example, the aerosol transport model alone. Experimental results were presented for the validation of the aerosol generation and transport models. The next chapter will present the procedure and its application for the the model-based AACVD process scale-up.

6 Process Design for Scale-up under Uncertainty

There are several possible options to be considered for a large-scale AACVD. Some options may scale-up better than others, based on the design criteria and the constraints related to the aerosol generation, transport, delivery and the chemical deposition itself. As a design methodology, the expected process output will be defined as a target and the results will be shown for the aerosol generation and transport, then for the aerosol delivery and the film formation. The objective is to understand the whole process from the perspective of the industry, which is interested in large production rates of a specific film thickness.

The set of parameters and their values used in the models can be found in Table 6.1. For the deposition of different films, there will be a different set of model parameters, since they are a function of the precursors, solvents, carrier gas and reaction mechanisms. However, to illustrate the use of the models for the industrial setting, the carrier gas will be nitrogen and the precursor solvent methanol, as seen in Chapter 5. For the aerosol generation and transport models, some of the parameters were fixed according to what could be expected for an industrial-scale process, such as transport system length and number of pipe bends. Other parameters were allowed to be changed, called design variables, such as the pipe inner diameter and the atomiser frequency. For the aerosol delivery and chemical deposition, the heat transfer coefficients are calculated using the correlations presented in Section 4.5. Specific heats are obtained from Perry et al. [117]. Finally, the mass transfer coefficients and the kinetic coefficients are obtained by fitting parameters from experimental results. Since the reaction mechanism presented here is general, the fitting process only used average values found in the literature for the thickness of AACVD films experimentally deposited [30, 32, 35, 162, 163]. However, for a specific film, the experimental results for such a film must be used.

Table 6.1: Values used for the model parameters in the industrial-scale range with the objective of continuously coating glass with 425 nm film thickness.

Symbol	Parameter	Nominal Value	Units
A	Glass surface area in contact with the gas	$4.5 \cdot 10^{-3}$	m^2
$c_{p,d}$	Droplet average specific heat	$2.6 \cdot 10^{3}$	$J \cdot kg^{-1} \cdot K^{-1}$
c_p	Carrier gas average specific heat	$1.1 \cdot 10^{3}$	$J \cdot kg^{-1} \cdot K^{-1}$
h_1	Heat transfer coefficient wall to carrier gas	6	$W \cdot m^{-2} \cdot K^{-1}$
h_2	Heat transfer coefficient carrier gas to droplet	$2.5 \cdot 10^{3}$	$W \cdot m^{-2} \cdot K^{-1}$
$h_{m,A}$	Mass transfer coefficient of component A	$7.4 \cdot 10^{-4}$	$m \cdot s^{-1}$
$h_{m,B}$	Mass transfer coefficient of component B	$1.2 \cdot 10^{-2}$	$m \cdot s^{-1}$
$h_{m,C}$	Mass transfer coefficient of component C	$1.4 \cdot 10^{-3}$	$m \cdot s^{-1}$
$h_{m,D}$	Mass transfer coefficient of component D	$1 \cdot 10^{-9}$	$m \cdot s^{-1}$
$h_{m,s}$	Mass transfer of the precursor solvent	1.5	$m \cdot s^{-1}$
$h_{vap,d}$	Droplet specific heat of evaporation	$1.2 \cdot 10^{6}$	$J \cdot kg^{-1}$
k_1	Kinetic constant of reaction 1	1.62	s^{-1}
k_2	Kinetic constant of reaction 2	$8.96 \cdot 10^{-4}$	$m \cdot s^{-1}$
k_3	Kinetic constant of reaction 3	$5.6 \cdot 10^{-4}$	$m \cdot s^{-1}$
L	Transport system length	$5.0 \cdot 10^{1}$	m
N	Number of 90° pipe bends	5	–
P	Contact surface perimeter for heat transfer in the distributor beam	6.4	m
s	*S*tandard deviation for the droplet *log*-normal distribution	0.6	–
T_w	Wall temperature	$7.8 \cdot 10^{2}$	K
v_g	Carrier gas velocity inside the deposition beam	0.3	$m \cdot s^{-1}$
V	Reactor volume	$1.4 \cdot 10^{-4}$	m^3
V_{int}	Solid-gas interface volume	$1 \cdot 10^{-5}$	m^3
μ	Carrier gas dynamic viscosity	$1.9 \cdot 10^{-5}$	$N \cdot s \cdot m^{-2}$
μ_d	Droplet dynamic viscosity	$5.5 \cdot 10^{-4}$	$N \cdot s \cdot m^{-2}$
ρ	Carrier gas density	1.2	$kg \cdot m^{-3}$
$\bar{\rho}$	Film average molar density	$7 \cdot 10^{4}$	$mol \cdot m^{-3}$
ρ_d	Droplet density	$7.9 \cdot 10^{2}$	$kg \cdot m^{-3}$
σ_d	Surface tension of the precursor solution	$2.2 \cdot 10^{-2}$	$N \cdot m^{-1}$
Φ	Volume fraction of aerosol in the carrier gas	0.02	–
Symbol	Design Variable	Range	Units
C_A^{prec}	Concentration of precursor A in the solution to generate aerosol	$[0.01, 1.0] \cdot 10^{3}$	$mol \cdot m^{-3}$
d	Pipe inner diameter	$[0.5, 9] \cdot 10^{-2}$	m
f	Ultrasonic atomiser frequency	$[0.1, 54] \cdot 10^{5}$	Hz
$\dot{F}_{in}$	Carrier gas volumetric flow rate	$[1, 7] \cdot 10^{-2}$	$m^3 \cdot s^{-1}$
N_P	Number of parallel pipes	$[1, 10]$	–

6.1 Aerosol Generation and Transport

Given the amount of reactants necessary for the production of a film with a specific thickness, the aerosol generation and transport system can be designed. For the aerosol generation, the models show that the most impactful variable on the aerosol sizing is the atomiser ultrasonic frequency. This is important, since the sizing has the greatest impact on the aerosol loss for a given transport geometry, followed by the carrier gas flow rate. Note that the relative range of the uncertain droplet sizes is much greater than all the other variables in the transport model.

To illustrate the outputs of the transport model, the droplet distributions before and after a 50 m transport system are shown in Figure 6.1 for two different distributions of droplet sizes in the aerosol. Results show that 86 % of the aerosol is expected to successfully reach the distributor beam for the aerosol with 2 μm median droplet diameter and 26 % for the 10 μm median droplet diameter. Note that more of the larger droplets are lost, indicating the importance of modelling the full range of possible droplet sizes, explained by the different extent of aerosol loss depending on the size of the particles. The optimum sizing range for transport can be found for each particular transport system. Additionally, the maintenance schedule is a function of the aerosol loss and can be determined by the presented models, varying according to the generated droplet sizes and the properties of the flow and the transport system.

6.2 Aerosol Delivery and Chemical Deposition

TCO functional films reported in the literature [30, 32, 35, 162, 163], which satisfy industry standards for the functional properties, have their thicknesses varying from one-tenth to eight micrometres, depending on how long the deposition process is allowed to take place. Most papers published showing experimental work only report values of the final film thickness for a given reaction residence time. These values allow, as first approximation, the quantification of the uncertain coefficients in systems of ODEs analogous to the one represented in Equation 4.46. The conversion fraction of precursors can also be estimated, based on the final film thickness and the initial quantity of precursors used. The objective is simulating the continuous industrial-scale AACVD process; therefore, laboratory-scale batch experiments are used to study the reaction kinetics and transfer coefficients, which will then inform the models for the large-scale simulations. Equation 4.46 will have its

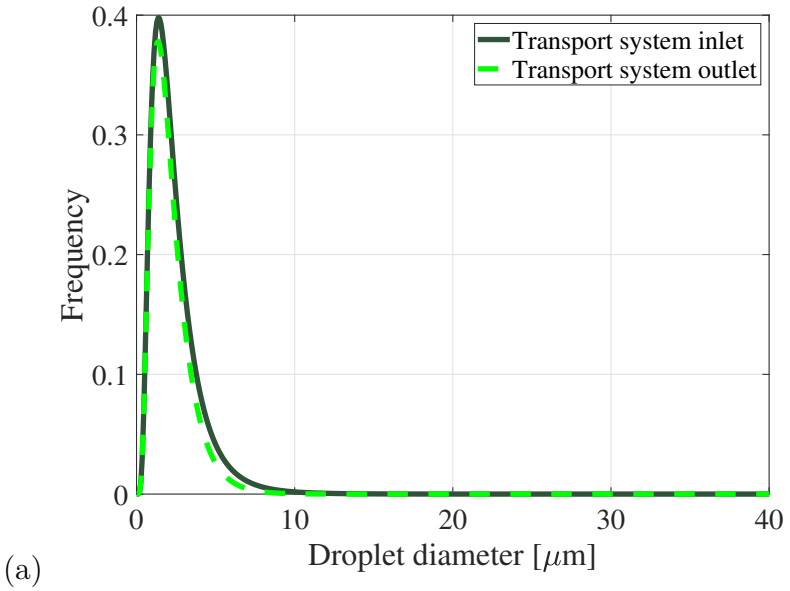

(a)

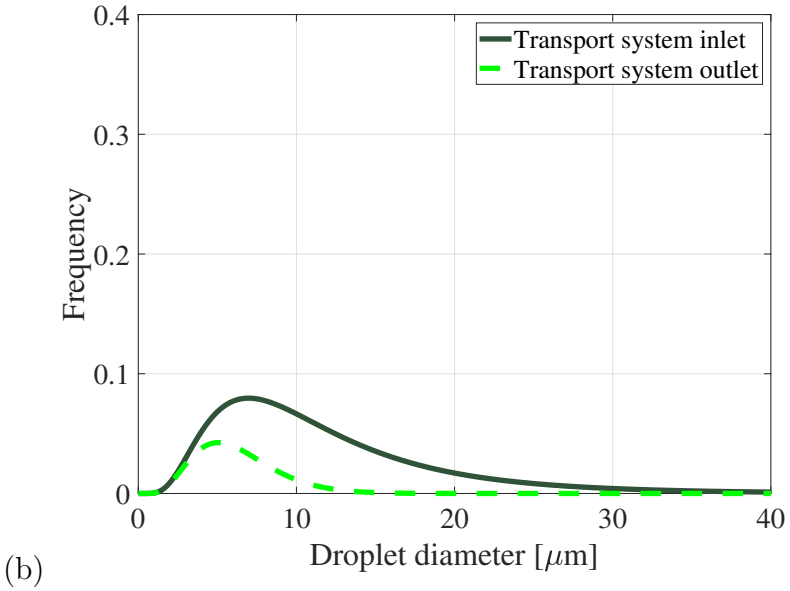

(b)

Figure 6.1: Droplet diameter distribution before and after a 50 m transport system. The diameter of the piping system was 6.2 cm for (a) and (b), while the inlet median droplet diameter was 2 μm for (a) and 10 μm for (b). Other parameters as described in Table 6.1. The area under the inlet curve is unitary, while the area under the outlet curve is the fraction of aerosol expected in the outlet of the transport system, 0.86 for (a) and 0.26 for (b).

scale-dependent parameters adjusted according to the scale, having different contact surface area, flow rates and concentrations. On the other hand, the mass transfer coefficients and kinetic constants are scale-independent and are estimated using the experiments.

The parameter estimation procedure from experimental data emphasises the need to handle uncertainties that arise from the scale-up. For example, using the final film thickness and deposition time from a laboratory-scale batch experiment for a particular deposition, the scale-independent parameters can be fitted. The time behaviour can then be obtained by the models, as exemplified by Figure 6.2(a). The time starts being counted when the reactant starts being delivered to the deposition site. The film starts growing at an approximately constant rate after one minute and analogous experiments usually last for about 15 minutes. Note that Figure 6.2(a) shows the most likely results. However, due to the uncertainties in the model parameters, there is actually a distribution of possible results for each time interval. As an example, Figure 6.2(b) shows the likelihood plot of the amounts of reactant A and main product D specifically for time $t = 2\,\text{min}$. This plot was obtained by using normal distributions for the three kinetic constants instead of using their deterministic nominal values shown in Table 6.1. To make the models more robust, it would be necessary to collect data on the evolution of the film thickness with time. Going further, it would also be useful to measure the concentrations of reactants, intermediates, products and by-products.

6.3 Distributor Beam and Industrial Continuous Process

The industrial deposition site is found at the final stage of the glass production. Current plants using the conventional CVD process use a distributor beam to deliver gaseous chemical precursors to the glass surface. Ideally, the same setting could be kept after switching to the AACVD process. In the latter case, an inert gas will carry aerosol containing precursors to the deposition site, which is shown in the bottom right-hand side of Figure 2.1. The schematic diagram is similar to the distributor beam made public by the International Patent 96/11802 [164]. The diagram shows a cross-section of the device, where the aerosol arrives from the top middle part and reaches the surface of a moving glass in the x-axis direction on the bottom part. The formation of a thin film with specific optoelectronic properties on the glass is

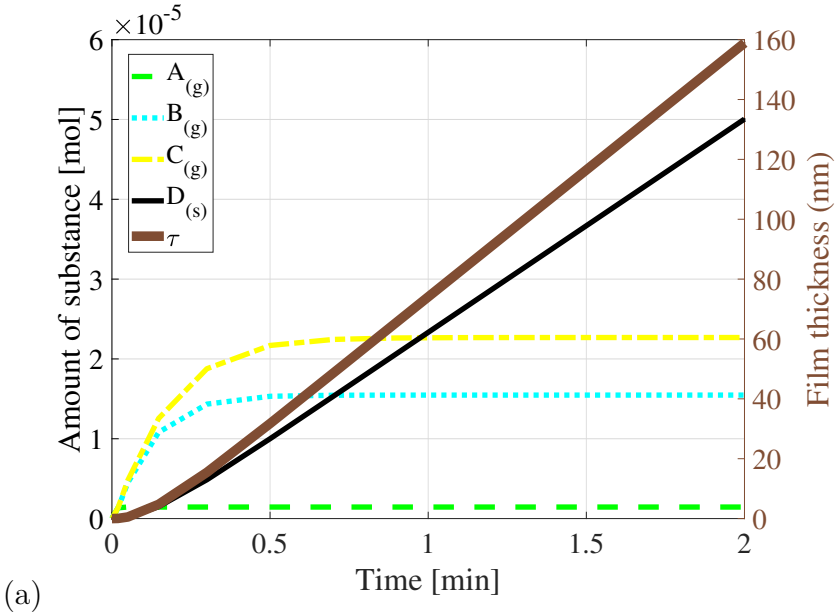

(a)

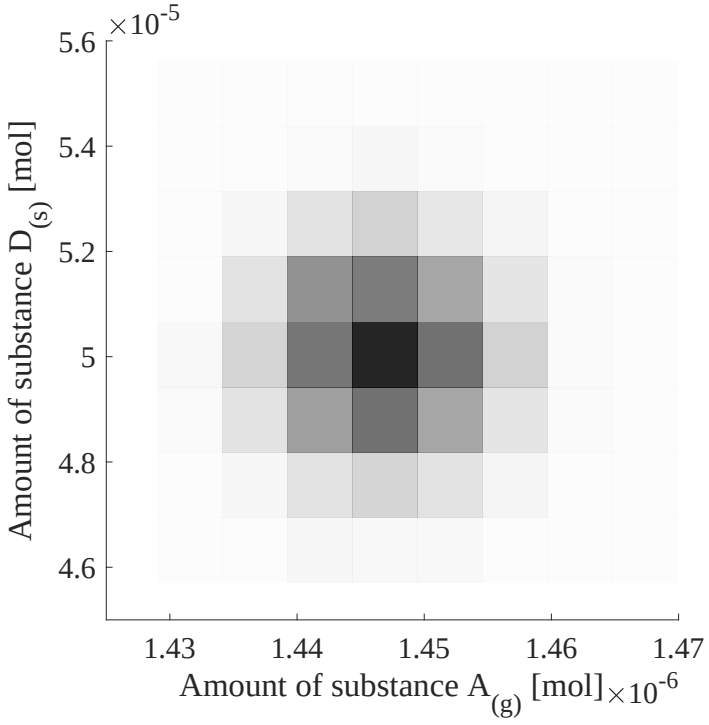

(b)

Figure 6.2: (a) Simulation of the laboratory-scale batch chemical deposition. The reactant A is fed at constant flow rate; component B is an intermediate; C is a by-product; D forms the thin film with thickness τ [nm] growing as shown in the right-hand side axis. (b) Plot showing the likelihood regions for the components A and D at time $t = 2\,\text{min}$, given the uncertainties in the model parameters. The darker the region, the more likely it is to represent reality. Model parameters as described in Table 6.1.

the final objective. The filled rectangles in the diagram are heat exchangers, which allow the temperature of the deposition site walls to be controlled.

The industrial process operates at constant temperature and atmospheric pressure. The glass width is in the direction perpendicular to the xy-plane, while the vertical direction represents the distributor's height, which is adjustable and can be taken as a design variable. The carrier gas arrives at the distributor beam at room temperature and its temperature increases while travelling between the walls of the distributor beam, as modelled by Equation 4.33. Discretising the x-axis, it is possible to solve the system of ODEs represented in Equation 4.46 for different positions, which allows the prediction of the chemical species concentration for different values of distance from the centre of the distributor beam. It is then possible to study different variations of the patented device, as shown in Figure 6.3.

As the results suggest, the film growth rate is not uniform throughout the reaction space. Whether the highest growth rate happens when the film has just started forming (parallel flow setting) or when the film already has some thickness (counter flow setting) will impact the properties of the film, given that its morphology can potentially differ. The best design will depend on the chemistry for the chosen precursors to produce a specific film. Note that the results shown in Figure 6.3(e) are not symmetric, since that would only happen if the flow were evenly distributed to both directions. The use of amount of substance instead of concentration is convenient, since it allows the representation of solid and vapour substances in the same plot. However, the concentrations of the substances in the vapour state are easily obtained and are directly proportional to their amounts, for example, Figure 6.4 shows the equivalent results of Figure 6.3(b).

6.4 Integrated Industrial-Scale Process

The simulations are carried out for the different parts of the process: aerosol generation, transport and delivery, and the chemical deposition. Since the final objective of the integrated process is to meet a specific deposition rate, all variables will be dependent on the chemical deposition results. Therefore, the design of each subprocess is done based on defined targets leading to a goal seeking iterative method. For example, aiming at a final film thickness, simulations are done to evaluate each subprocess. The models presented can also be used to predict the properties of the complete industrial-scale AACVD, given the final objective of continuously coating glass flowing at a specific speed. Simulating the process before

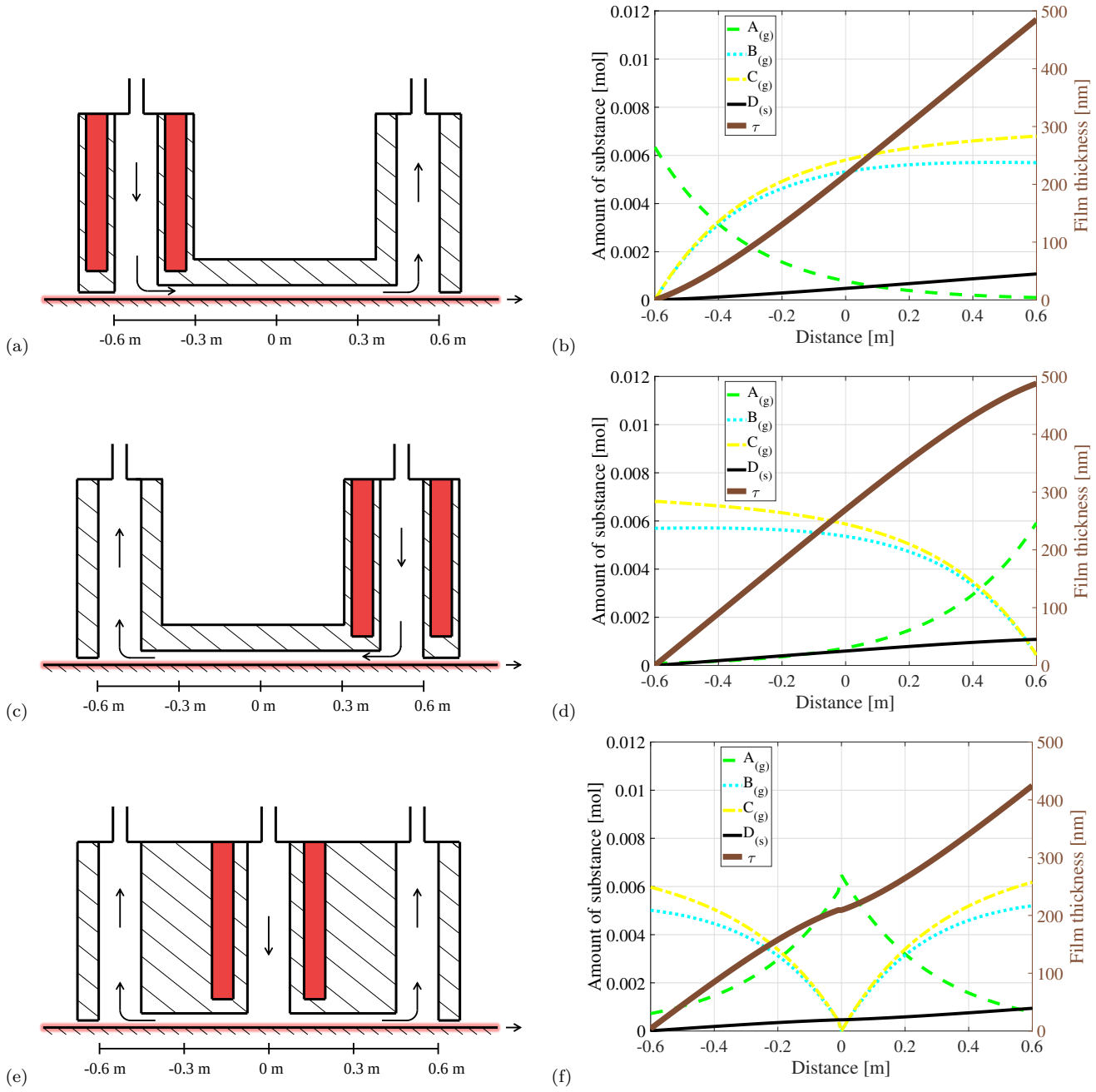

Figure 6.3: In the first column, schematic diagrams represent the cross-section of the deposition site in the direction of the glass flowing from left to right. Each schematic has its respective chemical deposition simulation results, shown in the second column. The parallel flow setting is shown in (a) and (b); the counter flow setting in (c) and (d); and the mixed flow setting in (e) and (f). The reactant A is consumed, while intermediate B and by-product C are produced and the film is formed by component D. The film thickness, τ [nm], is shown in the secondary axis. Model parameters as described in Table 6.1.

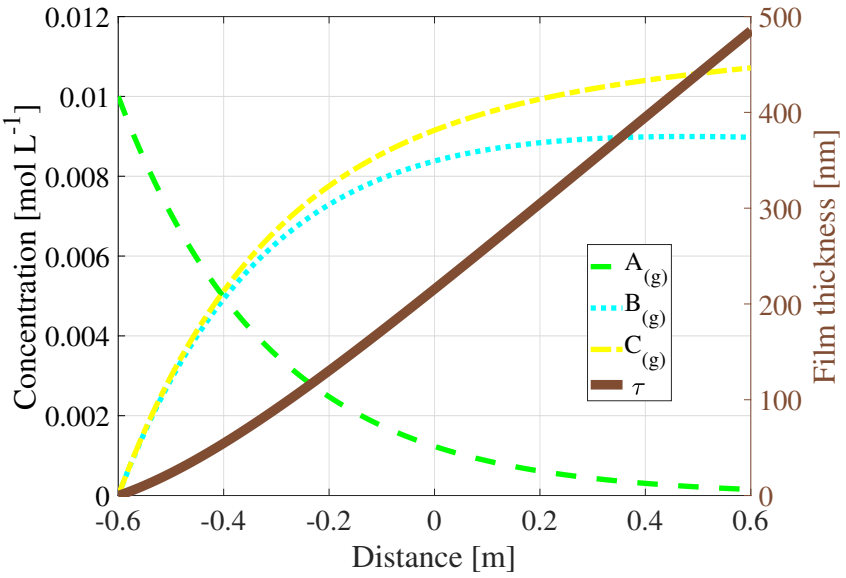

Figure 6.4: Concentration of the gaseous species in different regions of the deposition site. The reactant A is consumed, while intermediate B and by-product C are produced and the film is grown. The film thickness, τ [nm], is shown in the secondary axis. These results are for the parallel flow setting and are equivalent to Figure 6.3(b). Model parameters as described in Table 6.1.

scaling-up is also important to identify possible bottlenecks in the process and to determine where to dedicate more effort and resources. It also aids the evaluation of different process options and to determine process constraints, limiting factors and feasible conditions.

The use of the models is illustrated to suggest a possible configuration for the design of an industrial-scale AACVD process, including the maintenance schedule for the aerosol transport system. The final objective is producing films with a thickness of at least 425 nm in a continuous industrial-scale process. Laboratory-scale experimental results with settings analogous to the ones shown in Section 6.2, replacing the cold-trap by a CVD reactor, can be used to fit the mass transfer coefficients and kinetic constants from Equation 4.46 for the deposition site, which are scale-independent when using the same components and reactions. The necessary flow rate of precursors arriving at the reaction site is then estimated. Results show that a film of 425 nm thickness is obtained when using a total flow rate of $0.03\,\mathrm{m}^3 \cdot \mathrm{s}^{-1}$, with reactant concentration of $10\,\mathrm{mol} \cdot \mathrm{m}^{-3}$, and divided into five parallel pipes of 6.2 cm inner diameter. A high conversion of reactants of 88 % is obtained, however, only 7 % of what reacted is converted into the main product (D), the remainder becoming unreacted intermediate (B) and by-product (C). These results are shown in

Figure 6.3(f), for the industrial deposition site shown in Figure 6.3(e). The aerosol transport and delivery models show that for the $10\,\mathrm{mol}\cdot\mathrm{m}^{-3}$ reactant concentration in the reactor, the concentration in the beginning of the transport system must be $11.6\,\mathrm{mol}\cdot\mathrm{m}^{-3}$ since about 14 % of the aerosol will be lost during a 50 m transport distance, for 2 μm median droplet diameter (atomiser frequency 1.8 MHz), as shown in Figure 6.1(a). For this droplet distribution, the solvent will fully evaporate before the reactants reach the glass. If the aerosol volume fraction in the carrier gas is 2 %, the precursor solution used for the aerosol generation must therefore have a concentration of $580\,\mathrm{mol}\cdot\mathrm{m}^{-3}$.

Given that 14 % of aerosol is lost during transport and assuming that the transport system must always have 99 % of the piping system unclogged, for uniform loss throughout the piping system and average lost material density of $5\cdot10^{4}\,\mathrm{mol}\cdot\mathrm{m}^{-3}$, it would be necessary to run a solvent through the pipe system to clean it every 227 h of plant operation. To highlight the impact of the range of droplet sizes, if an aerosol with a 10 μm median droplet diameter (atomiser frequency 170 kHz) were used instead of 2 μm, the aerosol loss would jump from 14 % to 74 %, as shown in Figure 6.1(b). Keeping the same flow rate and precursor concentration, the film produced would have its thickness dropping from 425 nm to 110 nm and the transport system would have to be cleaned every 12 h of plant operation. Increasing the precursor solution concentration and/or increasing the flow rate would increase the film thickness. This is an iterative process, since the changes in concentration and/or flow rate will change the properties of the system, leading to a different aerosol loss during transport. However, the best solution would be to operate at a much lower fraction of aerosol loss, as what was obtained for the aerosol with 2 μm median droplet diameter.

The possible configuration and results obtained and described above are based on values that can be used in the industrial-scale process, as shown in Table 6.1. Note that all values shown in the table were fixed, which means they only apply to the particular precursor solution, transport system, distributor beam dimensions and temperature and set of reactions used. The design variables are the number of parallel pipes and their inner diameter, the ultrasonic frequency for the aerosol sizing, the flow rate, and the precursor concentration. However, the models presented can also simulate the process for different precursor solutions, different transport systems and different chemical reactions, with the aim of serving as a guide to the AACVD scale-up.

6.5 Summary

There are several possible design options to be considered for a large-scale AACVD. How to evaluate these options and how to apply a model-based scale-up procedure were presented. The objective was to understand the whole process from the perspective of the industry, which is interested in the large-scale production of functional films. One design was obtained for the AACVD process, which included the integrated use of the aerosol generation, transport, delivery and the chemical deposition models. Model uncertainty was taken into account, where parameters, measurements and process uncertainties were the sources of the uncertainties.

The chemical deposition mechanism presented was general and the methodology can be applied for the modelling of any deposition. Once a specific film has to be produced, the mechanism presented in Equation 4.44 can be adapted accordingly and the procedure executed in this chapter will provide results for that specific film.

7 Concluding Remarks and Future Work

This thesis ends with a summary of the work accomplished and the contributions provided, followed by the main limitations of the work and an indication of possible venues for future research.

7.1 Conclusions

The manufacture of coatings and thin films such as the TCOs is often limited by high costs, environmental impacts, and a scarcity of specific precursors. Therefore, it is essential to look for less expensive and more sustainable processes, which becomes an easier task as AACVD enables the consideration of a wider range of precursors. This thesis introduced the first integrated model for the AACVD process, which includes the aerosol generation, transport, delivery, and for the chemical deposition. The preliminary simulation results presented worked as a proof-of-concept for the use of simulations for gaining insights into the feasibility of an industrial-scale AACVD process and the possibility of keeping the current CVD equipment used in the industry to operate the AACVD technique instead.

Given an initial aerosol, with a log-normal distribution of droplet diameter, the prediction is a skewed outlet distribution. An extreme case of a coiled pipe was used to test the model fully. This latter case was validated experimentally, including droplet sizing by laser diffraction. The model proposed has been shown to predict aerosol distributions at the deposition site that take into account the different types of losses, suitable for transport distances on the scale of industrial processes. Based on probability distribution functions, the model incorporated the stochastic nature of both aerosol production and the factors that influence losses during transport, as well as the uncertainties impacting the chemical deposition. The modelling of the film formation brought insights about chemical mechanisms and the competition between mass transfer and reaction kinetics which affect the final product.

The models presented are also suitable to test different ranges of the AACVD process variables and parameters, in addition to other applications that rely on the atomisation and transport of particles, for example, spray drying or cooling, inkjet printing, agricultural sprays, and fuel combustion. Furthermore, the lessons learned in modelling uncertainties and their impact on process scale-up motivated research into formulation, modelling, and solution methods for such applications. The aim was to ease the procedure of design under uncertainty for a process scale-up and facilitate the interactions between different professionals, such as chemists and engineers. The experimental validation for the AACVD models indicated their effectiveness at predicting transport losses and also highlighted the impacts of uncertainties in some of the key parameters. These uncertainties formed the basis for further research into the treatment of uncertainty in general, through a novel domain-specific modelling language.

Consequently, the Uncertainty.jl framework was introduced as a user-friendly environment for the modelling of uncertainty. Examples were presented to show the ease with which models can be developed, while the obtained solutions demonstrated the viability of this prototype language, whose merits are particularly promising, when considering the relative ease through which models can be written. In fact, the framework has already been used in a number of peer-reviewed publications, as shown next in the "Publications" section.

The Uncertainty.jl framework and the AACVD models developed and presented in this thesis are freely available on GitHub [1]. Readers of this thesis are more than welcome to contact the author for collaborations, as well as to run the codes for any purpose, including to study, change, and distribute them and any adapted versions.

7.2 Recommendations for Future Work

The aerosol generation model does not provide the standard deviation for the *log*-normal distribution of aerosol sizing, which has to be determined using experimental results. It would be useful to extend the model to also provide the standard deviation. The aerosol transport model did not account for aerosol evaporation/condensation and coalescence/fracture. The model was applied to a transport system at room temperature and with low aerosol concentration, which is reasonable in the AACVD context. However, the model could be extended to allow applications that use the transport system at higher temperatures or with higher aerosol concentration or transporting a very volatile aerosol.

The AACVD models themselves can be further validated. Most experimental results found in the literature show the final film thickness, but not the evolution in time. The latter would greatly help to build a mechanism for the production of a specific film. Additionally, it would be very interesting to apply the models and methodology presented in this thesis to model the AACVD large-scale production of a specific film. Depending on the results, the industry could, perhaps, try and adopt the AACVD process.

The models presented could be integrated within an optimisation-based design framework. This could enable the identification of the best settings for the design variables for specific film growth rates and optoelectronic film properties. The lumped nature of the models presented in this thesis could also be considered to be used within a real-time optimisation system, possibly enabling a more robust or flexible process operation.

On that note, adding optimisation capabilities to the Uncertainty.jl framework would be a useful by-product. The framework could also facilitate and encourage the use of Machine Learning in the context of process modelling. This could be achieved by allowing users access to supervised learning algorithms, as well as inference algorithms and probabilistic programming tools. Uncertainty.jl could have a parser for the communication with the most established modelling platforms, such as GAMS, AMPL and gPROMS. Finally, more work is also required in terms of further incorporating state-of-the-art methods for handling uncertainties.

Publications

Some of the work that led to this thesis has appeared previously in the following peer-reviewed publications:

1. P. I. O. Filho, D. B. Potter, M. J. Powell, C. J. Carmalt, P. Angeli, and E. S. Fraga, "Probability Density Functions for Droplet Sizing in Aerosol Transport Modelling," *Computer Aided Chemical Engineering*, vol. 40, no. 1, 2017.

2. P. I. O. Filho, P. Angeli, and E. S. Fraga, "Modelling under Uncertainty for Process Design and Scale-up of an Industrial AACVD," *Computer Aided Chemical Engineering*, vol. 44, no. 1, 2018.

3. P. I. O. Filho and E. S. Fraga, "On the Design and Implementation of a Process Modelling Language for Uncertainty," *Computer Aided Chemical Engineering*, vol. 46, no. 1, 2019.

4. P. I. O. Filho, C. J. Carmalt, P. Angeli, and E. S. Fraga, "Mathematical Modeling for the Design and Scale-Up of a Large Industrial Aerosol-Assisted Chemical Vapor Deposition Process under Uncertainty," *Industrial & Engineering Chemistry Research*, vol. 59, no. 3, 2020.

5. M. Pineda, D. Tsaoulidis, P. I. O. Filho, T. Tsukahara, P. Angeli, and E. S. Fraga, "Design Optimization of Microfluidic-Based Solvent Extraction Systems for Radionuclides Detection," *Nuclear Engineering and Design*, vol. 383, 2021.

References

[1] P. I. O. Filho and E. S. Fraga, "Uncertainty.jl Framework and the AACVD models," 2021. GitHub repository: https://github.com/ivopedro3/AACVD-models-and-Uncertainty.jl.

[2] J. A. Cano-Ruiz and G. J. McRae, "Environmentally conscious chemical process design," *Annual Review of Energy and the Environment*, vol. 23, pp. 499–536, 1998. WOS:000077473600014.

[3] G. J. Harmsen, "Reactive distillation: The front-runner of industrial process intensification - A full review of commercial applications, research, scale-up, design and operation," *Chem. Eng. Process.*, vol. 46, pp. 774–780, Sept. 2007. WOS:000249632000002.

[4] M. Braungart and W. McDonough, *Cradle to Cradle*. Random House, Jan. 2009. Google-Books-ID: 13hfHzBstcEC.

[5] S. Chu and A. Majumdar, "Opportunities and challenges for a sustainable energy future," *Nature*, vol. 488, pp. 294–303, Aug. 2012.

[6] M. K. H. Rabaia, M. A. Abdelkareem, E. T. Sayed, K. Elsaid, K.-J. Chae, T. Wilberforce, and A. G. Olabi, "Environmental impacts of solar energy systems: A review," *Science of the Total Environment*, vol. 754, p. 141989, Feb. 2021. Place: Amsterdam Publisher: Elsevier WOS:000593904200011.

[7] D. Gielen, F. Boshell, D. Saygin, M. D. Bazilian, N. Wagner, and R. Gorini, "The role of renewable energy in the global energy transformation," *Energy Strategy Reviews*, vol. 24, pp. 38–50, Apr. 2019. Place: Amsterdam Publisher: Elsevier WOS:000466911300004.

[8] P. Marchand, I. A. Hassan, I. P. Parkin, and C. J. Carmalt, "Aerosol-assisted delivery of precursors for chemical vapour deposition : expanding the scope of CVD for materials fabrication," *Dalton Transactions*, vol. 42, no. 26, pp. 9406–9422, 2013.

[9] X. Hou and K.-L. Choy, "Processing and applications of aerosol-assisted chemical vapor deposition," *Chem. Vapor Depos.*, vol. 12, pp. 583–596, Oct. 2006. WOS:000241774400002.

[10] K. L. Choy, "Chemical vapour deposition of coatings," *Progress in Materials Science*, vol. 48, no. 2, pp. 57–170, 2003. WOS:000180690200001.

[11] Y. Zhang, L. Zhang, and C. Zhou, "Review of Chemical Vapor Deposition of Graphene and Related Applications," *Accounts of Chemical Research*, vol. 46, pp. 2329–2339, Oct. 2013. WOS:000326123300015.

[12] A. Reina, X. Jia, J. Ho, D. Nezich, H. Son, V. Bulovic, M. S. Dresselhaus, and J. Kong, "Large Area, Few-Layer Graphene Films on Arbitrary Substrates by Chemical Vapor Deposition," *Nano Letters*, vol. 9, pp. 30–35, Jan. 2009. WOS:000262519100006.

[13] A. L. M. Reddy, A. Srivastava, S. R. Gowda, H. Gullapalli, M. Dubey, and P. M. Ajayan, "Synthesis Of Nitrogen-Doped Graphene Films For Lithium Battery Application," *Acs Nano*, vol. 4, pp. 6337–6342, Nov. 2010. WOS:000284438000007.

[14] S. Park, M. Vosguerichian, and Z. Bao, "A review of fabrication and applications of carbon nanotube film-based flexible electronics," *Nanoscale*, vol. 5, no. 5, pp. 1727–1752, 2013. WOS:000314931900002.

[15] Y. Wu, Y.-m. Lin, A. A. Bol, K. A. Jenkins, F. Xia, D. B. Farmer, Y. Zhu, and P. Avouris, "High-frequency, scaled graphene transistors on diamond-like carbon," *Nature*, vol. 472, pp. 74–78, Apr. 2011. WOS:000289199400039.

[16] C. Chung, Y.-K. Kim, D. Shin, S.-R. Ryoo, B. H. Hong, and D.-H. Min, "Biomedical Applications of Graphene and Graphene Oxide," *Accounts of Chemical Research*, vol. 46, pp. 2211–2224, Oct. 2013. WOS:000326123300004.

[17] N. Sinha, J. Z. Ma, and J. T. W. Yeow, "Carbon nanotube-based sensors," *Journal of Nanoscience and Nanotechnology*, vol. 6, pp. 573–590, Mar. 2006. WOS:000235941500001.

[18] X.-M. Li, D. Reinhoudt, and M. Crego-Calama, "What do we need for a superhydrophobic surface? A review on the recent progress in the preparation of superhydrophobic surfaces," *Chemical Society Reviews*, vol. 36, no. 8, pp. 1350–1368, 2007. WOS:000247933900011.

[19] C. R. Crick and I. P. Parkin, "Preparation and Characterisation of Super-Hydrophobic Surfaces," *Chemistry-a European Journal*, vol. 16, no. 12, pp. 3568–3588, 2010. WOS:000276327300001.

[20] N. P. Mellott, C. Durucan, C. G. Pantano, and M. Guglielmi, "Commercial and laboratory prepared titanium dioxide thin films for self-cleaning glasses: Photocatalytic performance and chemical durability," *Thin Solid Films*, vol. 502, pp. 112–120, Apr. 2006. WOS:000236309200023.

[21] L. Zhang, C.-H. Xue, M. Cao, M.-M. Zhang, M. Li, and J.-Z. Ma, "Highly transparent fluorine-free superhydrophobic silica nanotube coating," *Chemical Engineering Journal*, vol. 320, pp. 244–252, July 2017. WOS:000401202200027.

[22] K. L. Chopra, P. D. Paulson, and V. Dutta, "Thin-film solar cells: An overview," *Progress in Photovoltaics*, vol. 12, pp. 69–92, May 2004. WOS:000220731200002.

[23] C. P. Sajan, S. Wageh, A. A. Al-Ghamdi, J. Yu, and S. Cao, "TiO2 nanosheets with exposed {001} facets for photocatalytic applications," *Nano Research*, vol. 9, pp. 3–27, Jan. 2016. WOS:000371797800002.

[24] E. Franklin, K. Fong, K. McIntosh, A. Fell, A. Blakers, T. Kho, D. Walter, D. Wang, N. Zin, M. Stocks, E.-C. Wang, N. Grant, Y. Wan, Y. Yang, X. Zhang, Z. Feng, and P. J. Verlinden, "Design, fabrication and characterisation of a 24.4% efficient interdigitated back contact solar cell," *Progress in Photovoltaics*, vol. 24, pp. 411–427, Apr. 2016. WOS:000371890900001.

[25] Y. Jiang, M. R. Leyden, L. Qiu, S. Wang, L. K. Ono, Z. Wu, E. J. Juarez-Perez, and Y. Qi, "Combination of Hybrid CVD and Cation Exchange for Upscaling Cs-Substituted Mixed Cation Perovskite Solar Cells with High Efficiency and Stability," *Advanced Functional Materials*, vol. 28, pp. 1–13, Jan. 2018. WOS:000419025200006.

[26] D. B. Potter, I. P. Parkin, and C. J. Carmalt, "The effect of solvent on Al-doped ZnO thin films deposited via aerosol assisted CVD," *RSC Advances*, vol. 8, no. 58, pp. 33164–33173, 2018.

[27] J. Zhang, L. Wang, X. Liu, X. Li, and W. Huang, "High-performance CdS–ZnS core–shell nanorod array photoelectrode for photoelectrochemical hydrogen generation," *Journal of Materials Chemistry A*, vol. 3, pp. 535–541, Dec. 2014.

[28] S. Sathasivam, D. S. Bhachu, Y. Lu, N. Chadwick, S. A. Althabaiti, A. O. Alyoubi, S. N. Basahel, C. J. Carmalt, and I. P. Parkin, "Tungsten Doped TiO_2 with Enhanced Photocatalytic and Optoelectrical Properties via Aerosol Assisted Chemical Vapor Deposition," *Scientific Reports*, vol. 5, pp. 1–10, June 2015.

[29] D. S. Bhachu, D. O. Scanlon, E. J. Saban, H. Bronstein, I. P. Parkin, C. J. Carmalt, and R. G. Palgrave, "Scalable route to CH3NH3PbI3 perovskite thin films by aerosol assisted chemical vapour deposition," *Journal of Materials Chemistry A*, vol. 3, no. 17, pp. 9071–9073, 2015.

[30] C. E. Knapp, G. Hyett, I. P. Parkin, and C. J. Carmalt, "Aerosol-Assisted Chemical Vapor Deposition of Transparent Conductive Gallium-Indium-Oxide Films," *Chemistry of Materials*, vol. 23, pp. 1719–1726, Apr. 2011.

[31] D. B. Potter, D. S. Bhachu, M. J. Powell, J. A. Darr, I. P. Parkin, and C. J. Carmalt, "Al-, Ga-, and In-doped ZnO thin films via aerosol assisted CVD for use as transparent conducting oxides," *Physica Status Solidi a-Applications and Materials Science*, vol. 213, pp. 1346–1352, May 2016. WOS:000378398400039.

[32] A. Tombesi, S. Li, S. Sathasivam, K. Page, F. L. Heale, C. Pettinari, C. J. Carmalt, and I. P. Parkin, "Aerosol-assisted chemical vapour deposition of transparent superhydrophobic film by using mixed functional alkoxysilanes," *Scientific Reports*, vol. 9, pp. 1–12, May 2019.

[33] D. B. Potter, M. J. Powell, J. A. Darr, I. P. Parkin, and C. J. Carmalt, "Transparent conducting oxide thin films of Si-doped ZnO prepared by aerosol assisted CVD," *RSC Advances*, vol. 7, no. 18, pp. 10806–10814, 2017.

[34] A. Zhuang, R. Liao, S. C. Dixon, Y. Lu, S. Sathasivam, I. P. Parkin, and C. J. Carmalt, "Transparent superhydrophobic PTFE films via one-step aerosol assisted chemical vapor deposition," *RSC Advances*, vol. 7, no. 47, pp. 29275–29283, 2017.

[35] M. J. Powell, D. B. Potter, R. L. Wilson, J. A. Darr, I. P. Parkin, and C. J. Carmalt, "Scaling aerosol assisted chemical vapour deposition: Exploring the relationship between growth rate and film properties," *Materials & Design*, vol. 129, pp. 116–124, Sept. 2017.

[36] D. B. Potter, M. J. Powell, I. P. Parkin, and C. J. Carmalt, "Aluminium/gallium, indium/gallium, and aluminium/indium co-doped ZnO thin

films deposited via aerosol assisted CVD," *Journal of Materials Chemistry C*, vol. 6, no. 3, pp. 588–597, 2018.

[37] B. Blackburn, I. Hassan, C. Zhang, C. Blackman, K. Holt, and C. J. Carmalt, "Aerosol Assisted Chemical Vapour Deposition Synthesis of Copper(I) Oxide Thin Films for CO2 Reduction Photocatalysis," *Journal of Nanoscience and Nanotechnology*, vol. 16, pp. 10112–10116, Sept. 2016.

[38] M. J. Powell, B. A. D. Williamson, S.-Y. Baek, J. Manzi, D. B. Potter, D. O. Scanlon, and C. J. Carmalt, "Phosphorus doped SnO 2 thin films for transparent conducting oxide applications: synthesis, optoelectronic properties and computational models," *Chemical Science*, vol. 9, no. 41, pp. 7968–7980, 2018.

[39] M. Ling, C. S. Blackman, R. G. Palgrave, C. Sotelo-Vazquez, A. Kafizas, and I. P. Parkin, "Correlation of Optical Properties, Electronic Structure, and Photocatalytic Activity in Nanostructured Tungsten Oxide," *Advanced Materials Interfaces*, vol. 4, pp. 1–7, Sept. 2017.

[40] K. A. Ramisetty, A. B. Pandit, and P. R. Gogate, "Investigations into ultrasound induced atomization," *Ultrason. Sonochem.*, vol. 20, pp. 254–264, Jan. 2013. WOS:000311130000036.

[41] A. Qi, L. Y. Yeo, and J. R. Friend, "Interfacial destabilization and atomization driven by surface acoustic waves," *Phys. Fluids*, vol. 20, p. 074103, July 2008. WOS:000258175600022.

[42] M. Frenklach and H. Wang, "Detailed surface and gas-phase chemical kinetics of diamond deposition," *Physical Review B*, vol. 43, pp. 1520–1545, Jan. 1991. Publisher: American Physical Society.

[43] D. R. Lamborn, D. W. Snyder, X. X. Xi, and J. M. Redwing, "Modeling studies of the chemical vapor deposition of boron films from B2H6," *Journal of Crystal Growth*, vol. 299, pp. 358–364, Feb. 2007.

[44] J.-H. Park, "Mathematical modeling for chemical vapor deposition in a single-wafer reactor: Application to low-pressure deposition of Tungsten," *Korean Journal of Chemical Engineering*, vol. 19, pp. 391–399, May 2002.

[45] F. de Jong and M. Meyyappan, "Numerical simulation of silicon carbide chemical vapor deposition," *Diamond and Related Materials*, vol. 5, pp. 141–150, Mar. 1996.

[46] K. Raji, S. Thomas, and C. B. Sobhan, "A chemical kinetic model for chemical vapor deposition of carbon nanotubes," *Applied Surface Science*, vol. 257, pp. 10562–10570, Oct. 2011.

[47] Y. Huang, "Modeling and analysis of SiO2 deposition during high-purity fused silica glass synthesis by SiCl4 chemical vapor deposition," *Ceramics International*, vol. 45, pp. 10740–10745, June 2019.

[48] Y. Huang, Z. Lu, and L. Zheng, "Study of SiCl4/H2/O2 chemical kinetics and its application to fused silica glass synthesis," *Combustion Science and Technology*, vol. 190, pp. 1861–1885, Oct. 2018. Publisher: Taylor & Francis _eprint: https://doi.org/10.1080/00102202.2018.1476349.

[49] S. Bhaviripudi, X. Jia, M. S. Dresselhaus, and J. Kong, "Role of Kinetic Factors in Chemical Vapor Deposition Synthesis of Uniform Large Area Graphene Using Copper Catalyst," *Nano Letters*, vol. 10, pp. 4128–4133, Oct. 2010. Publisher: American Chemical Society.

[50] P. T. Lin, Y. Jaluria, and H. C. Gea, "Parametric Modeling and Optimization of Chemical Vapor Deposition Process," *Journal of Manufacturing Science and Engineering*, vol. 131, Jan. 2009.

[51] A. Li, K. Norinaga, W. Zhang, and O. Deutschmann, "Modeling and simulation of materials synthesis: Chemical vapor deposition and infiltration of pyrolytic carbon," *Composites Science and Technology*, vol. 68, pp. 1097–1104, Apr. 2008.

[52] U. K. Singh, B. J. Reizman, S. M. Changi, J. L. Burt, and C. Orella, "Reaction Kinetics and Characterization," in *Chemical Engineering in the Pharmaceutical Industry*, pp. 151–190, John Wiley & Sons, Ltd, 2019.

[53] M. Zlokarnik, "Scale-Up of Chemical and Biotechnological Processes," *Encyclopedia of Industrial Biotechnology*, pp. 1–24, Apr. 2010.

[54] J. Hannon, "Characterization and First Principles Prediction of Api Unit Operations," in *Chemical Engineering in the Pharmaceutical Industry*, pp. 203–226, John Wiley & Sons, Ltd, 2019.

[55] S. Moran and M. Zlokarnik, "Scale-Up in Chemical Engineering," in *Ullmann's Encyclopedia of Industrial Chemistry*, pp. 1–33, American Cancer Society, 2017.

[56] H. Yang and D. G. Allen, "Model-based scale-up strategy for mycelial fermentation processes," *The Canadian Journal of Chemical Engineering*, vol. 77, no. 5, pp. 844–854, 1999.

[57] G. Francois and D. Bonvin, "Measurement-Based Real-Time Optimization of Chemical Processes," in *Control and Optimisation of Process Systems*, Academic Press, Apr. 2013.

[58] G. Malhotra, "Scale-up to Commercialization," in *Chemical Process Simplification*, pp. 171–188, John Wiley & Sons, Ltd, 2011.

[59] I. E. Grossmann, R. M. Apap, B. A. Calfa, P. García-Herreros, and Q. Zhang, "Recent advances in mathematical programming techniques for the optimization of process systems under uncertainty," *Computers & Chemical Engineering*, vol. 91, pp. 3–14, Aug. 2016.

[60] B. Iooss and A. Saltelli, "Introduction to Sensitivity Analysis," in *Handbook of Uncertainty Quantification* (R. Ghanem, D. Higdon, and H. Owhadi, eds.), pp. 1103–1122, Cham: Springer International Publishing, 2017.

[61] B. d. Finetti, *Theory of Probability: A critical introductory treatment*. Wiley, Mar. 2017. Google-Books-ID: PzmKjwEACAAJ.

[62] J. Zhang, "Modern Monte Carlo methods for efficient uncertainty quantification and propagation: A survey," *Wiley Interdisciplinary Reviews-Computational Statistics*, vol. 13, p. e1539, Sept. 2021. Place: Hoboken Publisher: Wiley WOS:000594981700001.

[63] N. V. Sahinidis, "Optimization under uncertainty: state-of-the-art and opportunities," *Comput. Chem. Eng.*, vol. 28, pp. 971–983, June 2004. WOS:000221418000010.

[64] I. N. Durbach and T. J. Stewart, "Modeling uncertainty in multi-criteria decision analysis," *European Journal of Operational Research*, vol. 223, pp. 1–14, Nov. 2012. WOS:000307796100001.

[65] H.-G. Beyer and B. Sendhoff, "Robust optimization - A comprehensive survey," *Computer Methods in Applied Mechanics and Engineering*, vol. 196, no. 33-34, pp. 3190–3218, 2007. WOS:000248605400009.

[66] J. C. Helton, J. D. Johnson, C. J. Sallaberry, and C. B. Storlie, "Survey of sampling-based methods for uncertainty and sensitivity analysis," *Reliab. Eng. Syst. Saf.*, vol. 91, pp. 1175–1209, Nov. 2006. WOS:000241350400009.

[67] Y. Li, J. Chen, and L. Feng, "Dealing with Uncertainty: A Survey of Theories and Practices," *Ieee Transactions on Knowledge and Data Engineering*, vol. 25, pp. 2463–2482, Nov. 2013. WOS:000324934400004.

[68] F. Borello, E. Cestino, and G. Frulla, "Structural Uncertainty Effect on Classical Wing Flutter Characteristics," *Journal of Aerospace Engineering*, vol. 23, pp. 327–338, Oct. 2010. WOS:000281824000012.

[69] T. Parker, E. Jepsen, and H. McCann, "Measurements and error analysis of droplet size in optically thick diesel sprays," in *Twenty-Seventh Symposium (international) on Combustion, Vols 1 and 2* (A. R. Burgess and F. L. Dryer, eds.), (Pittsburgh), pp. 1881–1888, Combustion Institute, 1998. WOS:000083308600217.

[70] M. O. Wittner, H. P. Karbstein, and V. Gaukel, "Pneumatic Atomization: Beam-Steering Correction in Laser Diffraction Measurements of Spray Droplet Size Distributions," *Applied Sciences-Basel*, vol. 8, p. 1738, Oct. 2018. Place: Basel Publisher: Mdpi WOS:000448653700033.

[71] G. Charalampous and Y. Hardalupas, "Method to reduce errors of droplet sizing based on the ratio of fluorescent and scattered light intensities (laser-induced fluorescence/Mie technique)," *Applied Optics*, vol. 50, pp. 3622–3637, July 2011. Place: Washington Publisher: Optical Soc Amer WOS:000293069000032.

[72] A. L. Hojberg and J. C. Refsgaard, "Model uncertainty - parameter uncertainty versus conceptual models," *Water Science and Technology*, vol. 52, no. 6, pp. 177–186, 2005. Place: London Publisher: I W a Publishing WOS:000233557300024.

[73] W. L. Oberkampf, S. M. DeLand, B. M. Rutherford, K. V. Diegert, and K. F. Alvin, "Error and uncertainty in modeling and simulation," *Reliability Engineering & System Safety*, vol. 75, pp. 333–357, Mar. 2002. Place: Oxford Publisher: Elsevier Sci Ltd WOS:000174658700007.

[74] R. J. Moffat, "Describing the uncertainties in experimental results," *Experimental Thermal and Fluid Science*, vol. 1, pp. 3–17, Jan. 1988.

[75] I. N. Durbach and T. J. Stewart, "An experimental study of the effect of uncertainty representation on decision making," *European Journal of Operational Research*, vol. 214, pp. 380–392, Oct. 2011. WOS:000293313400019.

[76] R. T. Rockafellar, *Optimization Under Uncertainty - Lecture Notes*. University of Washington, Seattle: Digital Version, 2001.

[77] J. Ghahremani-Nahr, R. Kian, and E. Sabet, "A robust fuzzy mathematical programming model for the closed-loop supply chain network design and a whale optimization solution algorithm," *Expert Systems with Applications*, vol. 116, pp. 454–471, Feb. 2019.

[78] B. D. Liu and K. Iwamura, "Chance constrained programming with fuzzy parameters," *Fuzzy Sets and Systems*, vol. 94, pp. 227–237, Mar. 1998. WOS:000072032200007.

[79] M. Inuiguchi and J. Ramı?k, "Possibilistic linear programming: a brief review of fuzzy mathematical programming and a comparison with stochastic programming in portfolio selection problem," *Fuzzy Sets and Systems*, vol. 111, pp. 3–28, Apr. 2000.

[80] P. Li, H. Arellano-Garcia, and G. Wozny, "Chance constrained programming approach to process optimization under uncertainty," *Computers & Chemical Engineering*, vol. 32, pp. 25–45, Feb. 2008. WOS:000251636100004.

[81] A. Nemirovski and A. Shapiro, "Convex approximations of chance constrained programs," *Siam Journal on Optimization*, vol. 17, no. 4, pp. 969–996, 2006. WOS:000244631800002.

[82] M. Wendt, P. Li, and G. Wozny, "Nonlinear chance-constrained process optimization under uncertainty," *Industrial & Engineering Chemistry Research*, vol. 41, pp. 3621–3629, July 2002. WOS:000176965700014.

[83] A. Neumaier, "Clouds, Fuzzy Sets, and Probability Intervals," *Reliable Computing*, vol. 10, pp. 249–272, Aug. 2004.

[84] K. Natarajan, D. Pachamanova, and M. Sim, "Constructing Risk Measures from Uncertainty Sets," *Operations Research*, vol. 57, pp. 1129–1141, Oct. 2009. WOS:000270866000008.

[85] R. L. Harrison, "Introduction to Monte Carlo Simulation," in *Nuclear Physics Methods and Accelerators in Biology and Medicine* (A. Dubnickova, S. Dubnicka, C. Granja, C. Leroy, and I. Stekl, eds.), vol. 1204, (Melville), pp. 17–21, Amer Inst Physics, 2009. ISSN: 0094-243X WOS:000281184400003.

[86] A. Jasra, K. Law, and C. Suciu, "Advanced Multilevel Monte Carlo Methods," *International Statistical Review*, vol. 88, pp. 548–579, Dec. 2020. Place: Hoboken Publisher: Wiley WOS:000517673000001.

[87] M. Betancourt, "The Convergence of Markov Chain Monte Carlo Methods: From the Metropolis Method to Hamiltonian Monte Carlo," *Annalen Der Physik*, vol. 531, p. 1700214, Mar. 2019. Place: Weinheim Publisher: Wiley-V C H Verlag Gmbh WOS:000460956500008.

[88] J. C. Helton and F. J. Davis, "Latin hypercube sampling and the propagation of uncertainty in analyses of complex systems," *Reliability Engineering & System Safety*, vol. 81, pp. 23–69, July 2003. WOS:000183391300003.

[89] Y. Wang and S. Boyd, "Fast Model Predictive Control Using Online Optimization," *Ieee Transactions on Control Systems Technology*, vol. 18, pp. 267–278, Mar. 2010. WOS:000274996100003.

[90] A. I. J. Forrester and A. J. Keane, "Recent advances in surrogate-based optimization," *Progress in Aerospace Sciences*, vol. 45, pp. 50–79, Apr. 2009. WOS:000263652500003.

[91] N. V. Queipo, R. T. Haftka, W. Shyy, T. Goel, R. Vaidyanathan, and P. K. Tucker, "Surrogate-based analysis and optimization," *Progress in Aerospace Sciences*, vol. 41, pp. 1–28, Jan. 2005. WOS:000229133400001.

[92] F. A. C. Viana, T. W. Simpson, V. Balabanov, and V. Toropov, "Metamodeling in Multidisciplinary Design Optimization: How Far Have We Really Come?," *Aiaa Journal*, vol. 52, pp. 670–690, Apr. 2014. WOS:000332960100002.

[93] M. Mernik, J. Heering, and A. M. Sloane, "When and how to develop domain-specific languages," *ACM Comput. Surv.*, vol. 37, pp. 316–344, Dec. 2005. WOS:000236006500002.

[94] A. van Deursen, P. Klint, and J. Visser, "Domain-specific languages: An annotated bibliography," *Acm Sigplan Notices*, vol. 35, pp. 26–36, June 2000. WOS:000088371500003.

[95] G. Karsai, J. Sztipanovits, A. Ledeczi, and T. Bapty, "Model-integrated development of embedded software," *Proceedings of the Ieee*, vol. 91, pp. 145–164, Jan. 2003. WOS:000180715800010.

[96] A. Fall and J. Fall, "A domain-specific language for models of landscape dynamics," *Ecological Modelling*, vol. 141, pp. 1–18, July 2001. WOS:000170638600001.

[97] N. Nystrom, M. R. Clarkson, and A. C. Myers, "Polyglot: An extensible compiler framework for Java," in *Compiler Construction, Proceedings* (G. Hedin, ed.), vol. 2622, pp. 138–152, Berlin: Springer-Verlag Berlin, 2003. WOS:000183068200011.

[98] A. R. da Silva, "Model-driven engineering: A survey supported by the unified conceptual model," *Computer Languages Systems & Structures*, vol. 43, pp. 139–155, Oct. 2015. WOS:000360513500006.

[99] J. Bezanson, S. Karpinski, V. B. Shah, and A. Edelman, "Julia: A Fast Dynamic Language for Technical Computing," *arXiv:1209.5145 [cs]*, Sept. 2012. arXiv: 1209.5145.

[100] B. Carpenter, A. Gelman, M. D. Hoffman, D. Lee, B. Goodrich, M. Betancourt, M. A. Brubaker, J. Guo, P. Li, and A. Riddell, "Stan: A Probabilistic Programming Language," *Journal of Statistical Software*, vol. 76, pp. 1–29, Jan. 2017. Place: Los Angeles Publisher: Journal Statistical Software WOS:000392705600001.

[101] J. Salvatier, T. Wiecki, and C. Fonnesbeck, "Probabilistic programming in Python using PyMC3," *Peerj Computer Science*, p. e55, Apr. 2016. Place: London Publisher: Peerj Inc WOS:000437456500001.

[102] P.-C. Buerkner, "brms: An R Package for Bayesian Multilevel Models Using Stan," *Journal of Statistical Software*, vol. 80, pp. 1–28, Aug. 2017. Place: Los Angeles Publisher: Journal Statistical Software WOS:000408409900001.

[103] Z. Ghahramani, "Probabilistic machine learning and artificial intelligence," *Nature*, vol. 521, pp. 452–459, May 2015. Place: London Publisher: Nature Publishing Group WOS:000355286600032.

[104] Y. Gal and Z. Ghahramani, "Dropout as a Bayesian Approximation: Representing Model Uncertainty in Deep Learning," in *International Conference on Machine Learning, Vol 48* (M. F. Balcan and K. Q. Weinberger, eds.), vol. 48, (San Diego), Jmlr-Journal Machine Learning Research, 2016. ISSN: 2640-3498 WOS:000684193701014.

[105] B. Echard, N. Gayton, and M. Lemaire, "AK-MCS: An active learning reliability method combining Kriging and Monte Carlo Simulation," *Structural Safety*, vol. 33, no. 2, pp. 145–154, 2011. Place: Amsterdam Publisher: Elsevier Science Bv WOS:000290355800003.

[106] J. Bezanson, A. Edelman, S. Karpinski, and V. B. Shah, "Julia: A Fresh Approach to Numerical Computing," *SIAM Review*, vol. 59, pp. 65–98, Jan. 2017. Publisher: Society for Industrial and Applied Mathematics.

[107] Q. Chen and I. Grossmann, "Recent Developments and Challenges in Optimization-Based Process Synthesis," *Annual Review of Chemical and Biomolecular Engineering*, vol. 8, no. 1, pp. 249–283, 2017. _eprint: https://doi.org/10.1146/annurev-chembioeng-080615-033546.

[108] F. Zappa Nardelli, J. Belyakova, A. Pelenitsyn, B. Chung, J. Bezanson, and J. Vitek, "Julia subtyping: a rational reconstruction," *Proceedings of the ACM on Programming Languages*, vol. 2, pp. 113:1–113:27, Oct. 2018.

[109] C. Rackauckas and Q. Nie, "DifferentialEquations.jl – A Performant and Feature-Rich Ecosystem for Solving Differential Equations in Julia," *Journal of Open Research Software*, vol. 5, p. 15, May 2017. Number: 1 Publisher: Ubiquity Press.

[110] Y. Ma, V. Dixit, M. J. Innes, X. Guo, and C. Rackauckas, "A Comparison of Automatic Differentiation and Continuous Sensitivity Analysis for Derivatives of Differential Equation Solutions," in *2021 IEEE High Performance Extreme Computing Conference (HPEC)*, pp. 1–9, Sept. 2021. ISSN: 2643-1971.

[111] F. Schäfer, M. Tarek, L. White, and C. Rackauckas, "AbstractDifferentiation.jl: Backend-Agnostic Differentiable Programming in Julia," *arXiv:2109.12449 [cs]*, Sept. 2021. arXiv: 2109.12449.

[112] W.-Y. Loh, "Fifty Years of Classification and Regression Trees," *International Statistical Review*, vol. 82, pp. 329–348, Dec. 2014.

[113] D. E. Dobry, D. M. Settell, and J. M. Baumann, "Spray Drying and Scale-Up," in *Pharmaceutical Sciences Encyclopedia*, pp. 1–26, American Cancer Society, 2015.

[114] M. Mezhericher, A. Levy, and I. Borde, "Modelling of particle breakage during drying," *Chemical Engineering and Processing: Process Intensification*, vol. 47, pp. 1404–1411, Aug. 2008.

[115] T. L. Bergman, A. S. Lavine, F. P. Incropera, and D. P. DeWitt, *Fundamentals of Heat and Mass Transfer*. John Wiley & Sons, Apr. 2011. Google-Books-ID: vvyIoXEywMoC.

[116] C. Christodoulou, E. Sorensen, S. García-Muñoz, and L. Mazzei, "Mathematical modelling of water absorption and evaporation in a pharmaceutical tablet during film coating," *Chemical Engineering Science*, vol. 175, pp. 40–55, Jan. 2018.

[117] D. Green, M. Z. Southard, and R. H. Perry, *Perry's Chemical Engineers' Handbook, 9th Edition*. New York, NY: McGraw-Hill Education, 9 edition ed., Sept. 2018.

[118] R. Rajan and A. B. Pandit, "Correlations to predict droplet size in ultrasonic atomisation," *Ultrasonics*, vol. 39, pp. 235–255, June 2001. WOS:000169103200001.

[119] G. Ramachandran and D. W. Cooper, "Size Distribution Data Analysis and Presentation," in *Aerosol Measurement* (P. Kulkarni, P. A. Baron, and K. Willeke, eds.), pp. 479–506, John Wiley & Sons, Inc., 2011.

[120] K. Yasuda, Y. Bando, S. Yamaguchi, M. Nakamura, A. Oda, and Y. Kawase, "Analysis of concentration characteristics in ultrasonic atomization by droplet diameter distribution," *Ultrason. Sonochem.*, vol. 12, pp. 37–41, Jan. 2005. WOS:000224680600007.

[121] R. Lang, "Ultrasonic Atomization of Liquids," *J. Acoust. Soc. Am.*, vol. 34, no. 1, pp. 6–8, 1962. WOS:A19622942B00018.

[122] J. H. Bang and K. S. Suslick, "Applications of Ultrasound to the Synthesis of Nanostructured Materials," *Advanced Materials*, vol. 22, no. 10, pp. 1039–1059, 2010.

[123] N. R. Sikwal, S. H. Sonawane, B. A. Bhanvase, K. Ramisetty, D. V. Pinjari, P. R. Gogate, and R. S. Babu, "Ultrasound-assisted preparation of ZnO nanostructures: understanding the effect of operating parameters," *Green Process. Synth.*, vol. 5, pp. 163–172, Apr. 2016. WOS:000374997600008.

[124] N. Anand, A. Mcfarland, K. Kihm, and F. Wong, "Optimization of Aerosol Penetration Through Transport Lines," *Aerosol Sci. Technol.*, vol. 16, pp. 105–112, Feb. 1992. WOS:A1992HG50800003.

[125] D.-L. Liu, "Particle Deposition onto Enclosure Surfaces," in *Developments in Surface Contamination and Cleaning* (R. Kohli and K. L. Mittal, eds.), pp. 1–56, Oxford: William Andrew Publishing, Jan. 2010.

[126] J. E. Brockmann, "Aerosol Transport in Sampling Lines and Inlets," in *Aerosol Measurement* (P. Kulkarni, P. A. Baron, and K. Willeke, eds.), pp. 68–105, John Wiley & Sons, Inc., 2011.

[127] A. Mcfarland, F. Wong, N. Anand, and C. Ortiz, "Aerosol Penetration Through a Model Transport-System - Comparison of Theory and Experiment," *Environ. Sci. Technol.*, vol. 25, pp. 1573–1577, Sept. 1991. WOS:A1991GD06000011.

[128] F. Lucci, N. D. Castro, A. A. Rostami, M. J. Oldham, J. Hoeng, Y. B. Pithawalla, and A. K. Kuczaj, "Characterization and modeling of aerosol deposition in Vitrocell® exposure systems - exposure well chamber deposition efficiency," *Journal of Aerosol Science*, vol. 123, pp. 141–160, Sept. 2018.

[129] E. M. A. Frederix, M. Stanic, A. K. Kuczaj, M. Nordlund, and B. J. Geurts, "Extension of the compressible PISO algorithm to single-species aerosol formation and transport," *International Journal of Multiphase Flow*, vol. 74, pp. 184–194, Sept. 2015.

[130] J. Brockmann, P. Mcmurry, and B. Liu, "Experimental-Study of Simultaneous Coagulation and Diffusional Loss of Free-Molecule Aerosols in Turbulent Pipe-Flow," *J. Colloid Interface Sci.*, vol. 88, no. 2, pp. 522–529, 1982. WOS:A1982PA56600021.

[131] K. Lee and J. Gieseke, "Deposition of Particles in Turbulent Pipe Flows," *J. Aerosol. Sci.*, vol. 25, pp. 699–709, June 1994. WOS:A1994NW86500011.

[132] P. I. O. Filho, D. B. Potter, M. J. Powell, C. J. Carmalt, P. Angeli, and E. S. Fraga, "Probability Density Functions for Droplet Sizing in Aerosol Transport Modelling," *Computer Aided Chemical Engineering*, vol. 40, no. 1, pp. 2245–2250, 2017.

[133] Y. Cheng and C. Wang, "Motion of Particles in Bends of Circular Pipes," *Atmos. Environ.*, vol. 15, no. 3, pp. 301–306, 1981. WOS:A1981LF21400012.

[134] M. Pilou, S. Tsangaris, P. Neofytou, C. Housiadas, and Y. Drossinos, "Inertial Particle Deposition in a 90 degrees Laminar Flow Bend: An Eulerian Fluid

Particle Approach," *Aerosol Science and Technology*, vol. 45, no. 11, pp. 1376–1387, 2011. WOS:000294604200009.

[135] S. R. Wilson, Y. Liu, E. A. Matida, and M. R. Johnson, "Aerosol Deposition Measurements as a Function of Reynolds Number for Turbulent Flow in a Ninety-Degree Pipe Bend," *Aerosol Science and Technology*, vol. 45, no. 3, pp. 364–375, 2011. WOS:000286655700007.

[136] Z.-J. Wang, F. Ding, G. Eres, M. Antonietti, R. Schloegl, and M. G. Willinger, "Formation Mechanism, Growth Kinetics, and Stability Limits of Graphene Adlayers in Metal-Catalyzed CVD Growth," *Advanced Materials Interfaces*, vol. 5, no. 14, pp. 1–15, 2018.

[137] T. Wu, X. Zhang, Q. Yuan, J. Xue, G. Lu, Z. Liu, H. Wang, H. Wang, F. Ding, Q. Yu, X. Xie, and M. Jiang, "Fast growth of inch-sized single-crystalline graphene from a controlled single nucleus on Cu–Ni alloys," *Nature Materials*, vol. 15, pp. 43–47, Jan. 2016.

[138] Z. Cai, B. Liu, X. Zou, and H.-M. Cheng, "Chemical Vapor Deposition Growth and Applications of Two-Dimensional Materials and Their Heterostructures," *Chemical Reviews*, vol. 118, pp. 6091–6133, July 2018.

[139] X. Li, L. Colombo, and R. S. Ruoff, "Synthesis of Graphene Films on Copper Foils by Chemical Vapor Deposition," *Advanced Materials*, vol. 28, no. 29, pp. 6247–6252, 2016.

[140] B. Liu, M. Fathi, L. Chen, A. Abbas, Y. Ma, and C. Zhou, "Chemical Vapor Deposition Growth of Monolayer WSe2 with Tunable Device Characteristics and Growth Mechanism Study," *ACS Nano*, vol. 9, pp. 6119–6127, June 2015.

[141] M. Hafeez, L. Gan, H. Li, Y. Ma, and T. Zhai, "Large-Area Bilayer ReS2 Film/Multilayer ReS2 Flakes Synthesized by Chemical Vapor Deposition for High Performance Photodetectors," *Advanced Functional Materials*, vol. 26, pp. 4551–4560, July 2016.

[142] X. He, F. Liu, P. Hu, W. Fu, X. Wang, Q. Zeng, W. Zhao, and Z. Liu, "Chemical Vapor Deposition of High-Quality and Atomically Layered ReS2," *Small*, vol. 11, no. 40, pp. 5423–5429, 2015.

[143] Z.-J. Wang, G. Weinberg, Q. Zhang, T. Lunkenbein, A. Klein-Hoffmann, M. Kurnatowska, M. Plodinec, Q. Li, L. Chi, R. Schloegl, and M.-G. Willinger, "Direct Observation of Graphene Growth and Associated Copper Sub-

strate Dynamics by in Situ Scanning Electron Microscopy," *ACS Nano*, vol. 9, pp. 1506–1519, Feb. 2015.

[144] G. Lu, T. Wu, Q. Yuan, H. Wang, H. Wang, F. Ding, X. Xie, and M. Jiang, "Synthesis of large single-crystal hexagonal boron nitride grains on Cu–Ni alloy," *Nature Communications*, vol. 6, pp. 1–7, Jan. 2015.

[145] A. Yan, J. Velasco, S. Kahn, K. Watanabe, T. Taniguchi, F. Wang, M. F. Crommie, and A. Zettl, "Direct Growth of Single- and Few-Layer MoS2 on h-BN with Preferred Relative Rotation Angles," *Nano Letters*, vol. 15, pp. 6324–6331, Oct. 2015.

[146] H. Li, Y. Li, A. Aljarb, Y. Shi, and L.-J. Li, "Epitaxial Growth of Two-Dimensional Layered Transition-Metal Dichalcogenides: Growth Mechanism, Controllability, and Scalability," *Chemical Reviews*, vol. 118, pp. 6134–6150, July 2018.

[147] B. Zheng, Y. Chen, Z. Wang, F. Qi, Z. Huang, X. Hao, P. Li, W. Zhang, and Y. Li, "Vertically oriented few-layered HfS2nanosheets: growth mechanism and optical properties," *2D Materials*, vol. 3, pp. 1–9, Sept. 2016.

[148] S. Wang, M. Liu, L. Kong, Y. Long, X. Jiang, and A. Yu, "Recent progress in VO2 smart coatings: Strategies to improve the thermochromic properties," *Progress in Materials Science*, vol. 81, pp. 1–54, Aug. 2016.

[149] M. Rahman, K. Davey, and S.-Z. Qiao, "Advent of 2D Rhenium Disulfide (ReS2): Fundamentals to Applications," *Advanced Functional Materials*, vol. 27, pp. 1–21, Mar. 2017.

[150] X.-G. Li and W.-D. Xiao, "Silane Pyrolysis to Silicon Rod in a Bell-Jar Reactor at High Temperature and Pressure: Modeling and Simulation," *Industrial & Engineering Chemistry Research*, vol. 55, pp. 4887–4896, May 2016.

[151] C. Cavallotti, F. Rossi, S. Ravasio, and M. Masi, "A Kinetic Analysis of the Growth and Doping Kinetics of the SiC Chemical Vapor Deposition Process," *Industrial & Engineering Chemistry Research*, vol. 53, pp. 9076–9087, June 2014.

[152] A. G. Salinger, R. P. Pawlowski, J. N. Shadid, and B. G. van Bloemen Waanders, "Computational Analysis and Optimization of a Chemical Vapor Deposition Reactor with Large-Scale Computing," *Industrial & Engineering Chemistry Research*, vol. 43, pp. 4612–4623, Aug. 2004.

[153] H. Wang, H. A. G. Stern, D. Chakraborty, H. Bai, V. DiFilippo, J. S. Goela, M. A. Pickering, and J. D. Gale, "Computational Study of Surface Deposition and Gas Phase Powder Formation during Spinel Chemical Vapor Deposition Processes," *Industrial & Engineering Chemistry Research*, vol. 52, pp. 15270–15280, Nov. 2013.

[154] L. Samandari-Masouleh, N. Mostoufi, A. Khodadadi, Y. Mortazavi, and M. Maghrebi, "Modeling the Growth of Carbon Nanotubes in a Floating Catalyst Reactor," *Industrial & Engineering Chemistry Research*, vol. 51, pp. 1143–1149, Jan. 2012.

[155] M. Vallerio, D. Telen, L. Cabianca, F. Manenti, J. Van Impe, and F. Logist, "Robust multi-objective dynamic optimization of chemical processes using the Sigma Point method," *Chem. Eng. Science*, vol. 140, pp. 201–216, 2016.

[156] L. E. K. Achenie, Y. Sharifi, and D. G. Lee, "Development of a Multiscale Strategy and Application to Chemical Vapor Deposition," in *Tools For Chemical Product Design: From Consumer Products to Biomedicine*, pp. 95–124, Elsevier, Sept. 2016. Google-Books-ID: Q5B4CgAAQBAJ.

[157] J. J. Thiart, V. Hlavacek, and H. J. Viljoen, "Chemical vapor deposition and morphology problems," *Thin Solid Films*, vol. 365, pp. 275–293, Apr. 2000.

[158] H. S. Fogler, *Elements of Chemical Reaction Engineering*. Upper Saddle River, NJ: Pearson, 6th edition ed., Jan. 2021.

[159] C.-H. Huang, K.-P. Chang, H.-D. Ou, Y.-C. Chiang, and C.-F. Wang, "Adsorption of cationic dyes onto mesoporous silica," *Microporous and Mesoporous Materials*, vol. 141, pp. 102–109, May 2011.

[160] R. Engle, *Advantages of Ultrasonic Spray Coatings of Biomaterials onto Devices and Implantables*. 2010.

[161] "LIQUIFOG® Ultrasonic Liquid Atomizer - Technical Data," *Johnson Matthey Piezo Products GmbH*, Feb. 2018.

[162] M. J. Powell and C. J. Carmalt, "Aerosols: A Sustainable Route to Functional Materials," *Chemistry – A European Journal*, vol. 23, no. 62, pp. 15543–15552, 2017.

[163] C. E. Knapp, C. Dyer, N. P. Chadwick, R. Hazael, and C. J. Carmalt, "Metal β-diketoiminate precursor use in aerosol assisted chemical vapour deposition

of gallium- and aluminium-doped zinc oxide," *Polyhedron*, vol. 140, pp. 35–41, Feb. 2018.

[164] M. J. Soubeyrand, "Glass coating method and glass coated thereby," *World Intellectual Property Organization*, p. WO1996011802A1, Apr. 1996. Patent Number: WO1996011802A1. Assignee: Libbey-Owens-Ford Co.